

UNIVERSITY OF OKLAHOMA
GRADUATE COLLEGE

ULTRA-MINIATURIZED AND HIGH-Q EMBEDDED LOADED
COAXIAL CAVITY RESONATORS AND FILTERS

A DISSERTATION
SUBMITTED TO THE GRADUATE FACULTY
in partial fulfillment of the requirements for the
Degree of
DOCTOR OF PHILOSOPHY

By

NAWAF ALMUQATI
Norman, Oklahoma
2023

ULTRA-MINIATURIZED AND HIGH-Q EMBEDDED LOADED
COAXIAL CAVITY RESONATORS AND FILTERS

A DISSERTATION APPROVED FOR THE
SCHOOL OF ELECTRICAL AND COMPUTER ENGINEERING

BY THE COMMITTEE CONSISTING OF

Dr. Hjalti Sigmarsson, Chair

Dr. Yingtao Liu

Dr. Jorge Salazar-Cerreno

Dr. Tian-You Yu

Dr. Yan Zhang

© Copyright Nawaf Almuqati 2023

All Rights Reserved.

*To my dear wife,
for her unconditional love, support, and encouragement throughout my
academic journey.*

Acknowledgments

I would like to express my deepest gratitude to my Ph.D. advisor Professor Hjalti Sigmarsson for his exceptional support, guidance, and encouragement throughout my Ph.D. journey. His expertise, vision, and mentorship have been invaluable in shaping my research and personal skills. I am grateful for his tireless efforts and insightful feedback on my work, which has helped me to grow as a researcher. I am proud to have had the opportunity to work with such an amazing mentor. I would also like to thank my advisor for his understanding and flexibility, especially during challenging times. His support has been crucial in helping me overcome obstacles and keeping me focused on my research.

I would like to extend my sincere gratitude to the members of my Ph.D. committee, Professor Yingtao Liu, Professor Jorge Salazar-Cerreno, Professor Yan Zhang, and Professor Tian-You Yu, for their support, guidance, and invaluable insights throughout my Ph.D. I am grateful for the time, effort, and thoughtfulness that each committee member has put into reviewing my research and providing constructive feedback. Their feedback has been critical in shaping my work and guiding me toward the successful completion of my Ph.D.

Also, I would like to express my gratitude to my colleagues at the Advance Radar Research Center (ARRC) for their support, collaboration, and friendship during my time here. I am grateful for the opportunities to work with and learn from each one of them and for the joyful spirit that has been an inspiration of our time here. I would also like to acknowledge the supportive and inclusive

environment that the ARRC has provided, which has allowed me to thrive and feel valued as a member of the ARRC.

Finally, I would like to thank my family and my wife for their unconditional love and support. Their love and support have been my source of strength and inspiration, and I could not have done this without them. My words are not enough to express my gratitude to them. Thank You.

Abstract

The rapid development in modern wireless communication systems and remote sensing and their applications towards portable and compact systems are inevitable. Microwave filters are critical components in the RF front-ends for band selection and unwanted signal rejection. These filters generally occupy a large area in the RF front-ends. In addition, RF filters' in-band losses significantly impact the overall system performance, such as noise figure and dynamic range. Thus, compact and high-quality factor RF filters are greatly desirable. Embedded coaxial substrate integrated waveguide filters have shown great potential compared to competing technologies in terms of high-Q, compact size, planar form, and wide spurious free region. This dissertation develops the theory and design of ultra-miniaturized high-Q embedded loaded coaxial substrate integrated waveguide filters with potential application in modern communication systems.

In this research, high-Q and compact embedded loaded coaxial substrate integrated waveguide (ELCSIW) resonators are designed and investigated. Integrating air-filled parallel plate capacitive loading into an embedded coaxial cavity enables the achievement of a highly miniaturized resonator with a 99 % miniaturization factor compared to the conventional substrate integrated waveguide resonator. In-depth analysis of the resonant frequency, miniaturization factor, and unloaded quality factor is presented. A second-order ELCSIW filter with

a resonant frequency of 1.1 GHz is developed and implemented. The filter obtains a simulated insertion loss of 0.26 dB and a wide spurious free stopband up to seven times its resonant frequency. The overall ELCSIW filter size is $0.07\lambda_g \times 0.26\lambda_g$. The proposed ELCSIW filter demonstrates superiority in compactness, quality factor, and stopband rejection compared to other miniaturized counterparts. Moreover, the proposed ELCSIW filter showed a high power handling capability of 113 Watts through theoretical investigation. A mixed (electric and magnetic) inter-resonator coupling mechanism is developed and integrated into the ELCSIW filter to generate a transmission zero to improve the stopband rejection. The arbitrary location of the transmission zero is determined by the intensity of each coupling mechanism. Moreover, a novel post-fabrication frequency tuning mechanism for the embedded loaded coaxial substrate integrated waveguide filter is developed. The tuning mechanism is constructed of additional embedded capacitive loading strip lines that can be altered to compensate for fabrication tolerances. The circuit model and the working mechanism of the tuning circuit are explained and illustrated. The novel tuning method shows a capability of a post-fabrication tuning range of 10 % for the proposed ELCSIW filter.

This research illustrates the feasibility of designing and integrating low-loss, compact, low-cost, and lightweight filters for future communications and radar systems.

Contents

Acknowledgments	v
Abstract	vii
Table of Contents	ix
List of Tables	xii
List of Figures	xiv
1 Introduction	1
1.1 Motivation	1
1.2 Overview of Substrate Integrated Waveguide Technology	5
1.3 Overview of Miniaturization Techniques in Substrate Integrated Waveguide Technology	11
1.4 Dissertation Outline	18
2 Ultra-Miniaturized Substrate Integrated Resonators and Fil- ters	20
2.1 Embedded Loaded Coaxial Substrate Integrated Waveguide Res- onator Modeling	21
2.2 Embedded Loaded Coaxial Substrate-Integrated Waveguide Res- onator	36
2.2.1 Material Selection	36

2.2.2	Effective Dielectric Constant and Loss Tangent	41
2.2.3	Resonator Design	44
2.3	Second-Order Embedded Loaded Coaxial Substrate-Integrated Waveguide Filter	46
2.3.1	Input/Output Feed Lines Design	50
2.3.2	External Coupling Mechanism	54
2.3.3	Inter-Resonator Coupling Mechanism	55
2.3.4	Simulation Results	57
2.3.5	Fabrication Procedure	61
2.3.6	Measurements and Discussion	63
2.4	Second-order Embedded Loaded Coaxial SIW Filter with Mixed Electric and Magnetic Coupling	71
2.5	Power-Handling Capabilities	77
3	Post-Fabrication Frequency Tuning of Embedded Loaded Coaxial Substrate Integrated Waveguide Filters	84
3.1	Post-Fabrication Tuning Circuit Model	88
3.2	Post-Fabrication Tuning Mechanism	93
3.3	Post-Fabrication Frequency Tuning Filter	104
4	Ka-band Ultra-Miniaturized Substrate Integrated Waveguide Filters	115
4.1	Ka-band ELCSIW Bandpass Filter Design	115
4.1.1	Input/Output Feed Lines Design	118
4.1.2	Simulation Results	122
4.2	Ka-band Mixed-Coupling ELCSIW Bandpass Filter Design	124
5	Summary and Future Work	129
5.1	Summary of Work	129

5.2 Contributions	131
5.3 Future Work	132
Bibliography	137
Appendices	149
Appendix A	150
A.1 Fourth-order ELCSIW Filter	150
A.2 ELCSIW Resonator and Filter Fabrication Process	153

List of Tables

2.1	Comparison of selected available PCB lamination materials. . . .	40
2.2	Comparison of selected available prepreg materials.	41
2.3	Resonator design parameters. All dimensions are in mm.	45
2.4	The filter's Chebyshev polynomial coefficients, inter-resonator coupling coefficient, and the external quality factor of of the second-order Chebyshev ELCSIW filter.	49
2.5	Calculated capacitance and inductance of the vertical via transition lumped circuit model elements.	53
2.6	Second-order ELCSIW filter design parameters. All dimensions are in mm.	58
2.7	Comparison between the related works in the literature and the proposed ELCSIW filter.	70
2.8	Mixed-coupling second-order filters design parameters. All dimensions are in mm.	77
3.1	The post-fabrication tunable ELCSIW resonator design parameters. All dimensions are in mm.	92
3.2	Switch states of the tunable ELCSIW filter. ON: switch is connected, OFF: switch is disconnected.	96
3.3	Second-order post-fabrication tunable ELCSIW filter design parameters (filter A). All dimensions are in mm.	107

3.4	Switch states of the tunable ELCSIW filter (filter A). ON: switch is connected, OFF: switch is disconnected.	109
3.5	Second-order post-fabrication tunable ELCSIW filter design parameters (filter B). All dimensions are in mm.	112
3.6	Switch states of the tunable ELCSIW filter (filter B). ON: switch is connected, OFF: switch is disconnected.	112
4.1	Grounded coplanar waveguide design parameters. All dimensions are in mm.	119
4.2	Calculated capacitance and inductance of the Ka-band vertical via transition lumped circuit model elements.	121
4.3	Ka-band second-order Chebyshev ELCSIW bandpass filter design parameters. All dimensions are in mm.	123
A.1	The Chebyshev polynomial coefficients, inter-resonator coupling coefficient, and external quality factor for the fourth-order Chebyshev ELCSIW filter.	150
A.2	Fourth-order ELCSIW filter design parameters. All dimensions are in mm.	152
A.3	The periodic pulse revers program and waveform parameters. . . .	155

List of Figures

1.1	Illustration of the fundamental concept of the human respiration detection system using multiple UAV radar units.	2
1.2	A simplified example of super-heterodyne transceiver	3
1.3	The relative size, insertion loss, and cost of various RF resonators.	5
1.4	The SIW-related publications trend in the IEEE community.	7
1.5	The geometry of the SIW structure.	8
1.6	The SIW region of interest with respect to its cut-off frequency, vias diameter, and vias spacing.	11
1.7	Cross section of folded SIW (a) C-type and (b) T-type. (c) A 3-d view of double folded SIW resonator cavity (d) Top view of quadri-folded SIW resonator cavity.	12
1.8	The slow-wave structure (a) 3-D View, and (b) side view.	13
1.9	Field distribution of the circular SIW cavity resonator (a) full-mode, (b) half-mode, (c) quarter-mode, (d) eighth-mode, (e) sixteenth-mode, and (f) thirty-second-mode.	15
1.10	A 3-D and cross-sectional views of (a) RHMSIW, (b) transition between RHMSIW and FRHMSIW, and (c) FRHMSIW along with their respective fundamental mode field patterns.	15
1.11	(a) Unit-cell of CLRH-based SIW cavity resonator, and (b) CLRH structure based on folded-SIW.	16

1.12	(a) Coaxial SIW cavity resonator , and (b) embedded coaxial SIW cavity resonator.	18
2.1	Proposed ELCSIW resonator (a) top view, and (b) cross-section view. The image is not drawn to scale and dimensions are in mm. ($W = 10$, $W_r = 7.5$, $D = 0.5$ mm, $s_1 = 0.2$, $H_1 = 3.37$, $H_2 = 0.069$, $t = 0.017$, $d = 0.5$, $p = 1$).	22
2.2	(a) Top view of the magnetic field distribution, (b) cross-section view of the electric field distribution, and (c) cross-section view of the electric field intensity inside the ELCSIW cavity. The magnetic field distribution in the lower side of the cavity resembles that of a coaxial line. The electric field is primarily concentrated between the patch and the cavity top.	23
2.3	Quasi-static model of ELCSIW cavity resonator, (a) capacitive and inductive regions in ELCSIW resonator, and (b) equivalent circuit model.	23
2.4	Lumped element model of an ELCSIW cavity resonator.	26
2.5	A comparison of the resonant frequency versus air gap thickness for the ELCSIW resonator shown in Figure 2.1. Simulation: eigenmode ANSYS solver solution, Model 1: Loaded coaxial line model from (2.3), Model 2: Lumped element model from (2.10).	26
2.6	A comparison of the resonant frequency versus patch width for the ELCSIW resonator shown in Figure 2.1. Simulation: eignemode ANSYS solver solution, Model 1: Loaded coaxial line model from (2.3), Model 2: Lumped element model from (2.10).	27
2.7	Variation in frequency as a function of the prepreg thickness at three different post sizes, demonstrating the frequency sensitivity.	28

2.8	Miniaturization factor and quality factor of the ELCSIW resonator versus dielectric substrate thickness (H_1).	30
2.9	Miniaturization factor and quality factor of the ELCSIW resonator versus patch width (W_r).	31
2.10	Miniaturization factor and quality factor of the ELCSIW resonator versus air gap (H_2).	32
2.11	Miniaturization factor and quality factor of the ELCSIW resonator versus post diameter (D).	32
2.12	The miniaturization factor as function of H_2 for multiple post diameters values.	33
2.13	The unloaded quality factor as function of H_2 for multiple post diameters values.	34
2.14	The unloaded quality factor as a function of copper surface roughness at 5.8×10^7 S/m copper conductivity for the ELCSIW resonator in Figure 2.1.	35
2.15	Design illustration of the ELCSIW cavity resonator, (a) the top view, (b) a 3D structure view, and (c) side view.	37
2.16	The effect of the lamination process on the air gap thickness.	39
2.17	(a) Side view of the stack-up layers of the ELCSIW cavity resonator, (b) side view of the single homogeneous substrate with an effective dielectric constant (ϵ_{eff}) and loss tangent ($\tan\delta_{eff}$). Note that some wall vias of the cavity are not shown for clarity. All dimensions are in mm, and the image is not drawn to scale. ($h_1 = 1.27$, $h_2 = 0.1016$, $h_3 = 0.635$, $h_4 = 0.1016$, $h_5 = 1.27$, $H_1 = 3.3782$).	43
2.18	Effective dielectric constant of Sub1 versus the normalized frequency with respect to the design resonant frequency of 1 GHz.	43

2.19	3D view of the stack-up layers of the ELCSIW cavity resonator. Note that the vias of the ELCSIW cavity are not shown for clarity.	44
2.20	The transmission coefficient (S_{21}) of a weakly coupled ELCSIW cavity resonator.	46
2.21	Design illustration of the second-order ELCSIW filter, (a) a 3D structure view, (b) top view, and (c) side view. The image is not drawn to scale.	47
2.22	A 3-D view of the stack-up layers of the second-order ELCSIW filter. Note that the plated vias that form the walls of the ELCSIW filter are not shown for clarity.	50
2.23	A 3D view of the input/output feed line and vertical transition.	52
2.24	Vertical via transition equivalent lumped element circuit model.	52
2.25	S-parameters of the vertical transition via lumped element circuit model.	54
2.26	External quality factor of an ELCSIW resonator as a function of the external tap width at different tap heights.	55
2.27	Inter-resonator coupling coefficient of two coupled ELCSIW resonators as a function of the internal tap width at different tap heights.	57
2.28	Simulated S-parameters of the second-order ELCSIW filter.	59
2.29	A 3D view of the back-to-back input/output feed lines for the second-order ELCSIW filter.	59
2.30	Simulated S-parameters of the back-to-back input/output feed lines for the second-order ELCSIW filter.	60
2.31	Simulated S-parameters of the second-order ELCSIW filter showing the achieved wide spurious free stopband.	60
2.32	Photograph of the fabricated ELCSIW resonator.	64

2.33	Comparison between the simulated and measured S_{21} of the proposed ELCSIW resonator.	64
2.34	Photograph of the fabricated second-order ELCSIW filter.	65
2.35	Comparison between the simulated and measured wideband response of the second-order ELCSIW filter.	66
2.36	Comparison between the simulated and measured results of the second-order ELCSIW filter with a wide frequency sweep.	66
2.37	Post-fabrication tuning setup for the second-order ELCSIW filter.	67
2.38	Comparison between the simulated and measured results of the designed second-order ELCSIW filter after the post-tuning.	68
2.39	Design illustration of the second-order ELCSIW filter with mixed magnetic and electric coupling mechanisms.	72
2.40	Equivalent lumped element circuit model of the mixed-coupling second-order ELCSIW filter.	72
2.41	Inter-resonator coupling coefficient (k_{21}) as a function of the electric coupling strip length at different heights of the inter-resonator tap.	74
2.42	Second-order embedded loaded mixed-coupling coaxial SIW filter with dominant magnetic coupling.	75
2.43	Second-order embedded loaded mixed-coupling coaxial SIW filter with dominant electric coupling.	75
2.44	Simulated second-order mixed-coupling filter B showing the transmission zero locations as a function of the strip length (L_s).	76
2.45	Simulated stored energy of the resonators of the second-order ELCSIW filter.	81
2.46	Frequency locations of the extracted stored energy of the second-order ELCSIW filter.	81

2.47	Electric-field distribution inside the second-order ELCSIW filter cavity with the posts modeled as through-plated vias. The inset figure shows a closer view of the electric-field at the edge of the post.	82
2.48	Electric-field distribution inside the second-order ELCSIW filter cavity with the posts modeled as copper-filled vias. The inset figure shows a closer view of the electric-field at the edge of the patch	82
3.1	The measured S_{21} of the nine fabricated filters showing frequency variations due to the materials and fabrication tolerances.	85
3.2	The shift in the resonant frequency of the proposed ELCSIW resonator versus the dielectric constant tolerance of the substrate of thickness $H_1 = 3.378$ mm).	86
3.3	The shift in the resonant frequency of the proposed ELCSIW resonator versus the variation in the dielectric substrate of the thickness (H_1).	87
3.4	The shift in the resonant frequency of the proposed ELCSIW resonator versus the variation in the prepreg substrate thickness (H_2).	88
3.5	The structure of the proposed post-fabrication tunable ELCSIW resonator, (a) a 3D view, (b) top view, and (c) side view. The design parameters are presented in Table 3.1.	91
3.6	Circuit model of the proposed post-fabrication tunable ELCSIW resonator.	93
3.7	The effect of the H_2 tolerance on the resonant frequency of the sample resonator in Figure 3.5.	95
3.8	The impact of all switch states on the resonant frequency of the sample resonator in Figure 3.5.	95

3.9	The impact on the resonant frequency tuning of the sample resonator when all switches are connected (State 0) and when all switches are disconnected (State 8). This impact shows that maximum tunability can be obtained for the sample resonator with $\epsilon_t = 3.45$, $L_t = 2.7$ mm, and $W_t = 1.2$ mm.	97
3.10	The maximum tuning range as a function of the tuning substrate thickness for the sample resonator with $\epsilon_t = 3.45$, $L_t = 2.7$ mm, and $W_t = 1.2$ mm.	98
3.11	The maximum tuning range as a function of the tuning substrate dielectric constant at different tuning substrate thicknesses for the sample resonator with $L_t = 2.7$ mm and $W_t = 1.2$ mm.	99
3.12	The maximum tuning range as a function of the tuning stripline length at different tuning substrate thicknesses for the sample resonator with $\epsilon_t = 3.45$ mm and $W_t = 1.2$ mm.	99
3.13	The maximum tuning range and quality factor of the sample tunable ELCSIW resonator as a function of the tuning substrate thickness with $\epsilon_t = 3.45$ mm, $\tan\delta_t = 0.002$, $L_t = 2.7$ mm, and $W_t = 1.2$ mm.	101
3.14	The maximum tuning range and quality factor of the sample tunable ELCSIW resonator as a function of the tuning substrate dielectric constant with $\tan\delta_t = 0.002$, $H_t = 0.2032$, $L_t = 2.7$ mm, and $W_t = 1.2$ mm.	101
3.15	The unloaded quality factor of the sample tunable ELCSIW resonator as a function of the tuning substrate loss tangent at various tuning substrate thicknesses.	102
3.16	The transmission coefficient of a weakly coupled tunable ELCSIW cavity resonator.	103

3.17	The structure of the proposed post-fabrication tunable ELCSIW filter, (a) a 3D view, (b) top view, (c) side view.	106
3.18	The impact of Isola prepreg thickness variations on the tunable ELCSIW filter center frequency. Showing only S_{11} for clarity.	108
3.19	S-parameters of the tunable ELCSIW filter (filter A) at $H_2 = 68.58 \mu\text{m}$ and $H_2 = 58 \mu\text{m}$	109
3.20	The impact of disconnecting tuning switches of the tunable ELCSIW filter (filter A) on the center frequency. Initial: initial design of the ELCSIW filter with $H_2 = 68.58 \mu\text{m}$. Showing only S_{11} for clarity.	110
3.21	S-parameters of the designed tunable ELCSIW filter (filter A) with $H_2 = 68.58 \mu\text{m}$ and the re-tuned ELCSIW filter (filter A) with $H_2 = 58 \mu\text{m}$	110
3.22	S-parameters of the tunable ELCSIW filter (filter B) at $H_2 = 68.58 \mu\text{m}$ and $H_2 = 50 \mu\text{m}$	111
3.23	The impact of disconnecting tuning switches of the tunable ELCSIW filter (filter B) on the return loss. Initial: initial design of the ELCSIW filter with $H_2 = 68.58 \mu\text{m}$	113
3.24	S-parameters of the designed tunable ELCSIW filter (filter B) with $H_2 = 68.58 \mu\text{m}$ and the re-tuned ELCSIW filter (filter B) with $H_2 = 50 \mu\text{m}$	113
4.1	The structure of the Ka-band second-order ELCSIW bandpass filter, (a) 3D view, (b) top view, and (c) side view.	116
4.2	The substrate material stack-up for the Ka-band ELCSIW BPF.	117
4.3	Top-view of the grounded coplanar waveguide trace with design parameters illustrations.	118

4.4	The simulated S-parameters of the designed grounded coplanar waveguide.	119
4.5	Overview of the Ka-band vertical via transition to illustrate the lumped elements affecting the signal path.	120
4.6	Ka-band vertical via transition equivalent lumped element circuit model.	121
4.7	The simulated S-parameters of the Ka-band vertical transition via lumped element circuit model.	122
4.8	The simulated S-parameters of the Ka-band second-order ELCSIW bandpass filter.	123
4.9	Design illustration of the second-order ELCSIW filter (case A) with mixed magnetic and electric coupling mechanisms. ($L_s = 0.08$ mm, $W_s = 0.03$ mm, $G_s = 0.03$ mm, $D = 0.107$ mm, $W_{12} = 0.13$ mm, $W_{ex} = 0.09$ mm).	125
4.10	The simulated S-parameters of the Ka-band second-order ELCSIW filter (case A).	125
4.11	Design illustration of the Ka-band second-order ELCSIW filter (case B) with mixed magnetic and electric coupling mechanisms. ($L_s = 0.12$ mm, $W_s = 0.03$ mm, $G_s = 0.03$ mm, $D = 0.215$ mm, $W_{12} = 0.05$ mm, $W_{ex} = 0.087$ mm, $H_{in} = 0.1016$ mm).	126
4.12	The simulated S-parameters of the Ka-band second-order ELCSIW filter (case B).	127
5.1	The typical lamination setup for two substrates and a prepreg illustration the prepreg thickness reduction after pressing.	133
5.2	The proposed lamination setup for two substrates and a prepreg showing the benefit of the metal stopper in controlling the prepreg final thickness.	133

5.3	The proposed overview of the tunable ELCSIW filter using switch technology.	134
5.4	(a) Design layout of the proposed quad-mode ELCSIW cavity resonator, and (b) coupling scheme of the proposed quad-mode ELCSIW filter.	135
5.5	Vector plot of the simulated electric field distribution of the proposed quad-mode ELCSIW cavity resonator, (a) fundamental mode, (b) differential mode, (c) and (d) pair of orthogonal degenerate modes.	136
A.1	Design illustration of the fourth-order ELCSIW filter. (a) A 3D structure view, (b) top view, and (c) side view.	151
A.2	Simulated S-parameters of the fourth-order ELCSIW filter.	153
A.3	Schematic diagram illustrating the parameters to describe the forward and reverse pulse plating waveform.	155
A.4	Cross-section view of plated via using (a) forward pulse, and (b) periodic pulse reverse plating methods.	155

Chapter 1

Introduction

1.1 Motivation

Over the last decades, the rapid development in wireless communications technologies driven by low-cost integrated circuit fabrication has opened doors for new systems such as automotive radars, UAV communication systems, and cube-Sat atmospheric remote sensing systems. Low-altitude UAVs are widely employed in various industries for a variety of applications due to their mobility and versatility. UAVs have been considered the key factor in the development of many applications, including surveillance and monitoring, military, telecommunications, delivery of medical supplies, and rescue operations [1]. Thus, UAV research and development is the fastest-growing market globally. The worldwide market share for unmanned aerial vehicles is projected to grow from an estimated \$ 27.4 billion in 2021 to \$ 58.4 billion by 2026 [2]. This indicates the rapid growth and demand for lightweight, compact airborne communication systems in the next few years. This expansion in the use of UAV systems led to additional stringent demands on the specifications of their RF front-ends, requiring more compactness, cost-effectiveness, and lower loss.

Consider the example in Figure 1.1 where frequency-modulated continuous wave radar is deployed on UVA for detecting buried people for rescue missions [3]. In disaster events such as earthquakes and collapsed buildings, searching quickly

for buried people is vital for their survival. These scenarios are dangerous for rescue teams to approach quickly due to the instability of collapsed structures. Thus, technological solutions using UAVs and radar systems can be safer and more time-efficient for detection and rescue missions. The fundamental operation of the rescue system in Figure 1.1 is to detect buried people and measure their movement, particularly respiratory activity, using low-frequency signals. The movement can be identified by extracting the phase change on the low-frequency generated signal. The operation frequency is from 1.16 to 1.36 GHz with a pulse duration of $900 \mu\text{s}$ transmitted every 25 ms allowing for a 75 cm range resolution. Despite the system operating in a low-frequency band, it is critical to have a compact, lightweight RF front-end module for UAV deployment.

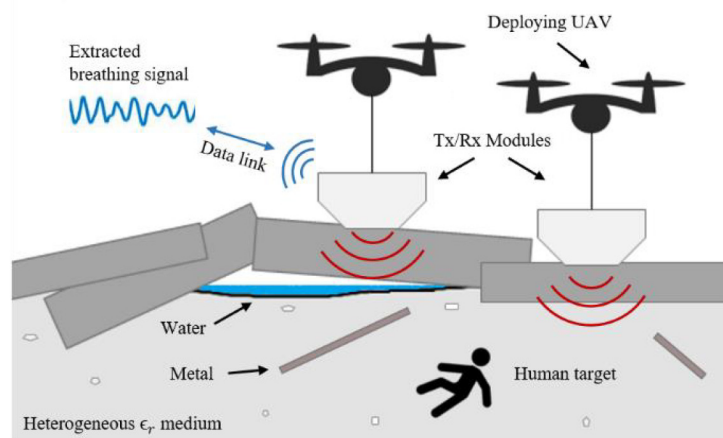


Figure 1.1: Illustration of the fundamental concept of the human respiration detection system using multiple UAV radar units (from [3]).

Filters have been extensively used in RF front-ends to suppress interference signals and spurious generated signals. These filters, in particular electromagnetic filters, occupy a large area in the RF front-end. Therefore, much research and developments have been directed toward miniaturizing RF filters to meet the requirement of the next generation of compact systems.

Figure 1.2 illustrates a front-end module of a simplified super-heterodyne

transceiver. The RF front end consists of two parallel branches for signal reception and transmission. In the receiver path, the antenna receives the signal and passes through an RF bandpass preselect filter. Preselect filters are commonly implemented in the receiver path right after the antenna to capture the desired signal and prevent possible image interfering and jamming signals. The receiver noise figure, which determines the system’s sensitivity, is significantly affected by the insertion loss of the preselect filter. In other words, any increase in the insertion loss of the preselect filter increases the noise figure, which limits the ability of the receiver to detect the signal from the noise floor [4]. Therefore, it is crucial for the preselect filters to have a compact size and a low insertion loss to reduce the impact on the system performance. Then, the signal is amplified using a low noise amplifier (LNA) and converted down to the intermediate frequency (IF) and baseband digital signal processing stages. In the transmitter path, the generated signal is filtered at the IF stage and up-converted to the RF band. Then, the RF signal is amplified with a high power amplifier (PA) and passes through a bandpass filter to suppress the transmission band noise and spurious emissions.

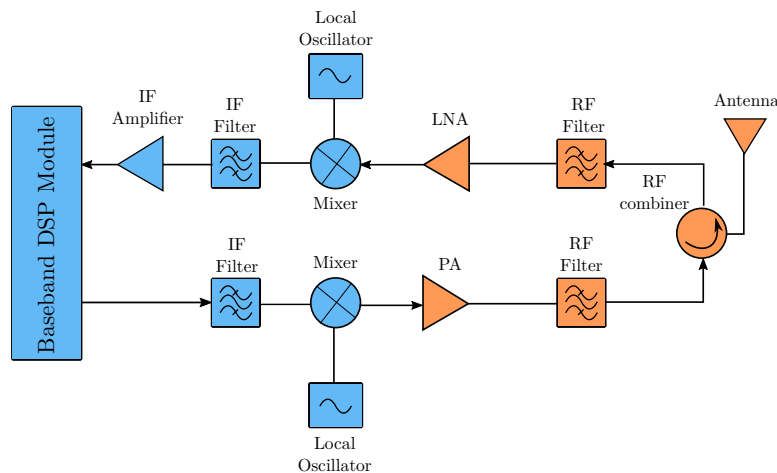


Figure 1.2: A simplified example of a super-heterodyne transceiver (from [5]).

A wide range of technologies can be utilized to implement filters based on

the application's requirements. Planar transmission lines, such as microstrip lines and coplanar waveguides, have been preferred in manufacturing a variety of filters and microwave components in the low-frequency range. They exhibit a low profile, lightweight and inexpensive manufacturing process. However, planar transmission lines have higher losses and exhibit signal interference between adjacent elements due to their structure's inherent radiation [6]. Conventional metallic waveguides are considered the best performance transmission line regarding quality factors and electromagnetic shielding. However, they are too large to embed in circuit boards and raise difficulties in manufacturing using standard fabrication techniques. Dielectric resonators offer a low-loss solution in a compact form factor, with the degree of miniaturization being inversely proportional to the square root of the dielectric constant of the low-loss material used. As a result of their high dielectric constant, dielectric resonator filters have limited spurious-free characteristics and require additional fabrication complexity [7]. The development of substrate integrated waveguide (SIW) reduced the gap between the lossy planar technology and bulky metallic waveguides, and achieved a remarkable trade-off. SIW technology combines the advantages of planar technology, namely low weight, and planar structure, and the metallic waveguide technology, which has a high-quality factor, electromagnetic shielding, and high power capability [8]. Another advantage that SIW technology provides is the possibility of integrating a complete system in one substrate, including antennas, passive elements, and active elements. Nevertheless, the size of the SIW is too large for compact airborne systems. Thus, numerous techniques have been proposed to miniaturize the SIW filters. The next two sections present overviews of the substrate integrated waveguide technology and the miniaturization techniques and structures for SIW. Figure 1.3 depicts a relative comparison between the aforementioned filter technologies in terms of size, insertion loss, and cost.

Among the miniaturized SIW filters, the loaded embedded coaxial substrate integrated waveguide filters demonstrate high miniaturization and high-quality factors. The feasibility of a loaded embedded coaxial substrate integrated waveguide filter to meet the stringent requirements of modern wireless systems in terms of size, weight, power, and cost (SWaP-C) is investigated. The proposed filters have shown ultra-miniaturized size and high-Q. In addition, the presented work has low weight and can handle 113 watts.

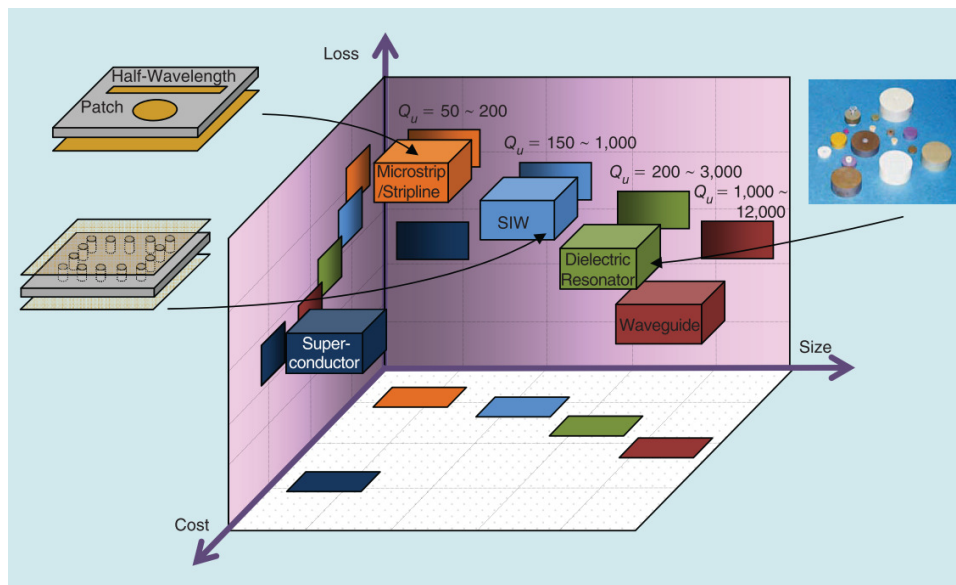


Figure 1.3: The relative size, insertion loss, and cost of various RF resonators (from [9]).

1.2 Overview of Substrate Integrated Waveguide Technology

Increasingly crucial to the development of future communication systems is the integration of passive and active components in a substrate. In communication systems, low cost, high performance, and a low profile are desirable characteristics. The integration of planar and non-planar system components presents obstacles. Interconnections between technologies, such as metallic waveguides and planar transmission lines, become the cause of performance deterioration and loss. In addition, incorporating non-planar components in a system limits

its miniaturization [10]. Planar transmission lines, such as microstrip lines and coplanar waveguides, have been preferred in manufacturing a variety of passive elements, interconnects, and antennas in the low-frequency range. They exhibit a low profile, are lightweight, and can be created using inexpensive manufacturing processes. However, they produce higher losses and exhibit signal interference between adjacent elements [11]. When compared to other types of transmission lines, waveguides outperform due to the absence of electromagnetic radiation and dielectric loss and hence superior transmission characteristics. However, they are impractical to embed in circuit boards and have difficulties manufacturing using standard fabrication techniques. These limitations inspired researchers to investigate and explore new technologies that surpass existing constraints. In 1998, researchers in Japan developed a technology called a laminated waveguide. The developed laminated waveguide is constructed of two sidewalls of vias and metalized planes that can be manufactured by standard printed circuit board (PCB) processing [12]. The primary motivation behind this invention is to meet the requirements of emerging compact systems. This was the first attempt to develop substrate integrated waveguide. Later in 2001, Ke Wu proposed the first integration between the microstrip line and substrate-integrated waveguide [13]. The development of SIW reduces the gap between the lossy planar technology and the bulky metallic waveguide. SIW technology combines the advantages of planar technology, namely low weight, and compactness, and the metallic waveguide technology, which has a high-quality factor, electromagnetic shielding, and high power capability [8]. These advantages attracted researchers' interest in the SIW techniques, which have been widely studied and developed at a fast pace compared to other substrate-integrated structures [14]. Figure 1.4 shows the popularity of SIW products in academia and the industry based on the number of IEEE technical papers published since the invention of the SIW. The figure

suggests a linear increase in the published paper in the field of SIW over the next few years.

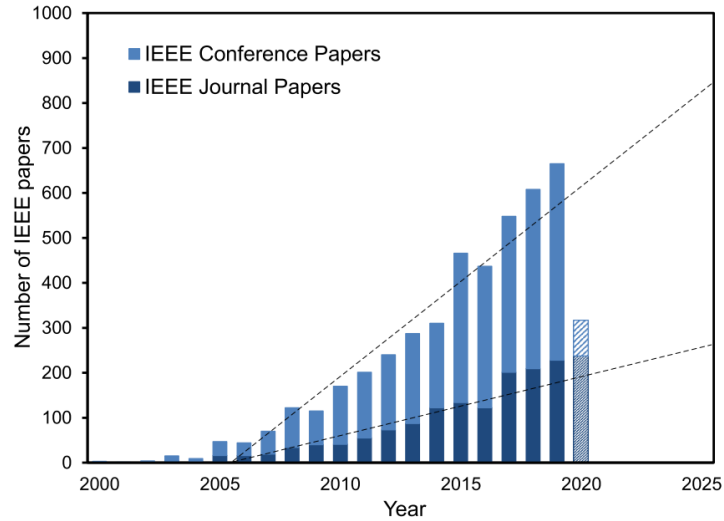


Figure 1.4: The SIW-related publications trend in the IEEE community (from [14]).

Substrate integrated waveguides are periodic structures consisting of two parallel rows of metallic vias electrically connected to a ground plane and filled with dielectric materials, as shown in Figure 1.5. They have low loss, planar structure, and low fabrication cost. They exhibit an equivalent behavior as conventional waveguides and demonstrate high power capability [15]. The distinctive feature of SIW is that an entire system can be integrated into a single layer, hence avoiding the need for transitions between technologies. A variety of microwave active and passive components are integrated into SIW, such as amplifiers [16], [17], filters [18], [19] and oscillators [20], [21].

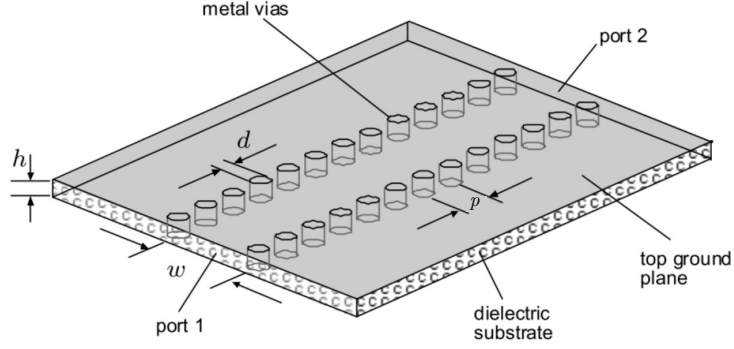


Figure 1.5: The geometry of the SIW structure (from [22]).

The wave propagation of SIW is similar to conventional waveguides. It supports the TE modes in which the surface current of the sidewalls can travel vertically along the metallic vias. Due to gap discontinuity along the longitudinal direction on the sidewall, SIW does not support TM modes. This characteristic classifies the SIW to be an H-plane waveguide [23]. Both SIW and conventional waveguides exhibit the same modes of dispersion characteristics. Therefore, SIW is equivalent to a conventional waveguide with equivalent width. The effective width of the SIW (w_{eff}) is characterized by the diameter of the via (d) and the spacing between vias (p), and its expressed by [24]:

$$w_{eff} = w - \frac{d^2}{0.95p}, \quad (1.1)$$

where w is the width of the SIW as shown in Figure 1.5. The cut-off frequency of the SIW can be determined by [24]:

$$f_c = \frac{c}{2\sqrt{\epsilon_r}} \left(w - \frac{d^2}{0.95p} \right)^{-1}, \quad (1.2)$$

where ϵ_r is the substrate relative dielectric permittivity and c is the speed of light.

The main components of loss in the substrate integrated waveguide structure

are dielectric loss (α_d), conductor loss (α_c), and radiation leakage (α_r). The total loss mechanism can be expressed mathematically as [25]

$$\alpha_{total} = \alpha_d + \alpha_c + \alpha_r. \quad (1.3)$$

Although radiation leakage exists in SIW, it's considered negligible if the design rules for d and p are correctly followed. The finite conductivity of the metal planes and vias is the primary cause of the conductor loss. The SIW's field distribution is equivalent to that of the rectangular waveguide. Hence the waveguide's analytical formula for calculating the conductor loss in [26] can be used for the SIW. Replacing the rectangular waveguide width with the effective width of the SIW, the conductor loss of the SIW can be determined by [25]

$$\alpha_c(f) = \frac{\sqrt{\pi f \epsilon_0 \epsilon_r} (1 + 2(f_0/f)^2 (h/w_{eff}))}{h \sqrt{\sigma_c} \sqrt{1 - (f_0/f)^2}}, \quad (1.4)$$

where h is the substrate thickness, ϵ_0 is the free space dielectric permittivity, and σ is the metal conductivity. Similarly, the analytical formula of dielectric loss derived for the rectangular waveguide can be adopted for the calculation of the attenuation constant of the SIW. The dielectric loss is proportional to loss tangent ($\tan\delta$) and be expressed as [25]

$$\alpha_d = \frac{\pi f \sqrt{\epsilon_r}}{c \sqrt{1 - (f_0/f)^2}} \tan\delta. \quad (1.5)$$

The SIW operates as equivalent to conventional waveguides with negligible leakage and free of bandgap in operation bandwidth if it follows the design rules of

d and p , which are [24]:

$$p > d \quad (1.6a)$$

$$\frac{p}{\lambda_c} < 0.25 \quad (1.6b)$$

$$\frac{\alpha_r}{k_o} < 1 \times 10^{-4} \quad (1.6c)$$

$$\frac{p}{\lambda_c} > 0.05, \quad (1.6d)$$

where $k_0 = 2\pi f \sqrt{\epsilon_r \epsilon_0 \mu_0}$ and μ_0 is the free space permeability. λ_c denotes the cutoff wavelength of the fundamental mode of the SIW. The condition (1.6a) states that the via spacing must be larger than the via diameter so it can be physically realizable. The condition (1.6a) is vital to avoid any bandgap in the operating bandwidth. To avoid leakage in the SIW structure, condition (1.6c) must be satisfied. For manufacturing process cost and mechanical rigidity of the SIW, the drilled vias should be minimized. Thus, condition (1.6d) suggests that the number of drilled vias should not be more than 20 per wavelength. The region of operation of SIW based on d and p is visualized in Figure 1.6.

This section summarizes the fundamental operation and characteristics of the SIW structures to highlight the advantages of this technology. The losses in the SIW are reviewed, and an analytical estimation of each loss mechanism is provided. Also, design rules for developing SIW structure are presented and discussed. These fundamental concepts and design rules are implemented in designing the ELCSIW cavity resonators and filters.

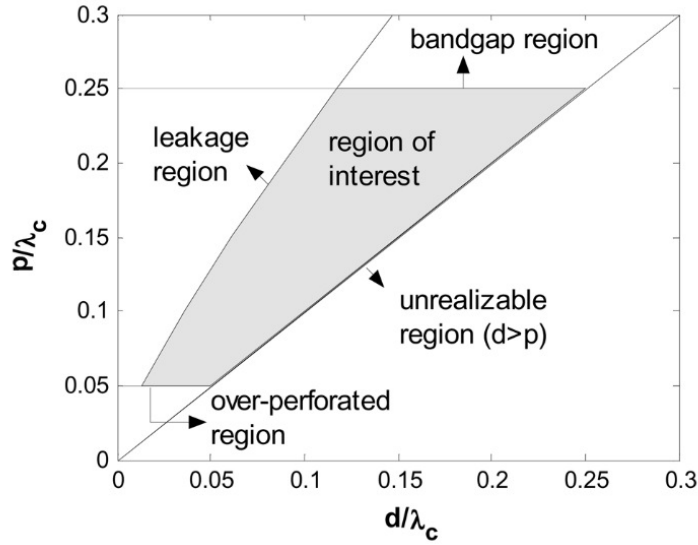


Figure 1.6: The SIW region of interest with respect to its cut-off frequency, vias diameter, and vias spacing (from [24]).

1.3 Overview of Miniaturization Techniques in Substrate Integrated Waveguide Technology

The SIW demonstrates the advantages of compact size and planar integration over the non-planar bulky waveguide. This allows integration with other planar technology and reduces the need for non-planar transitions. SIW is still considered a large structure compared to microstrip technology [9]. In addition, modern compact systems impose a stringent requirement for the dimensions of the RF circuit components making the conventional SIW less favored in comparison to planar technology. Therefore, numerous techniques have recently been developed to miniaturize SIW structures by operating at frequencies below fundamental resonant modes. An overview of some of the miniaturization techniques is presented in this section.

The folded SIW (FSIW) is a miniaturized structure whose sides are folded around its central part. This miniaturization technique was first presented in [27] with a T-type folding structure. It reduces the broadside length of the cavity by

50 % with a slight increase in the losses. A C-type folding was developed in [28], showing similar performance to T-type folding. The cross-section view of C-type and T-type folded SIW are shown in Fig. 1.7(a,b). In [29], a double-folded SIW (DFSIW) Chebyshev filter using a multi-layer low-temperature co-fired ceramic was presented. The double-folded SIW resonator is constructed by placing a metal plate with two orthogonal slots into the cavity. This resonator structure reduces the footprint of the circuit size by about a quarter of the fundamental TE_{101} mode. With its multi-layer design, the stacked Chebyshev filter is able to reduce its area by 88 %. Moreover, quadri-folded SIW (QFSIW) was used for the first time to miniaturize the conventional SIW cavity by 89 % [30]. A fourth-order Chebyshev filter was designed using a QFSIW cavity with vertical C-shaped coupling slots. The double-folded and quadri-folded SIW cavities are shown in Figs. 1.7(c,d).

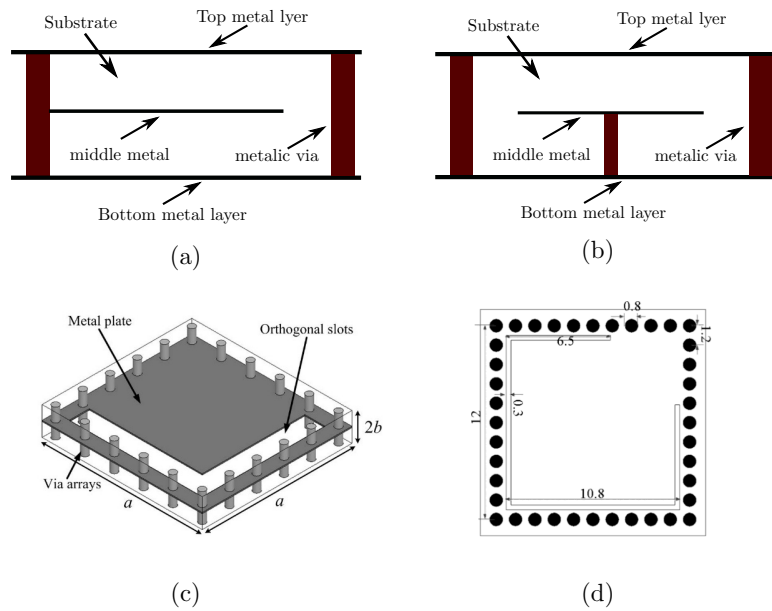


Figure 1.7: Cross section of folded SIW (a) C-type and (b) T-type. (c) A 3-d view of double folded SIW resonator cavity. (d) Top view of quadri-folded SIW resonator cavity (from [27–30]).

Another technique to reduce the SIW circuit size is using a slow-wave technique [31]. The slow-wave structure is composed of a double-substrate with embedded metallic vias in the bottom layer connected to the bottom metal layer, as shown in Figure 1.8. The slow-wave effect is generated by physically separating electric and magnetic fields within the structure. This configuration reduces the longitudinal dimension by more than 40 % due to a smaller phase velocity than the conventional SIW. The slow-wave technique was used in designing a fifth-order filter [32]. The filter was designed and measured at a center frequency of 11 GHz with a bandwidth of 900 MHz. A slow-wave effect enables to achieve more than 70 % size reduction compared to conventional SIW cavity filters. Another design methodology for a compact filter using the slow wave SIW technique was developed in [33]. The design approach combines a segmentation technique and polynomial fitting is provided to obtain accurate and fast design results. By incorporating a ladder coupling scheme with periodic blind vias embedded into a double-layer dielectric substrate, a bandpass filter at 11 GHz with a bandwidth of 1 GHz is realized. The filter obtained 60 % miniaturization.

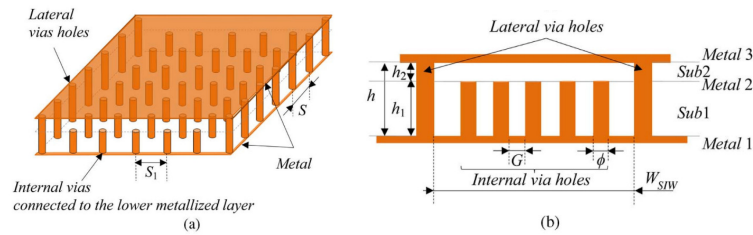


Figure 1.8: The slow-wave structure (a) 3-D View, and (b) side view (from [31]).

Sub-mode techniques of SIW resonators have been proposed to minimize SIW cavities by cutting the cavity of the dominant mode at its symmetric planes [34–38]. Half mode SIW (HMSIW), quarter mode SIW (QMSIW), eighth mode SIW (EMSIW), and sixteenth mode SIW (SMSIW) have all been proposed by cutting SIW resonators on their imaginary magnetic walls to obtain size reduction. The

electric field distributions of the fundamental mode of the abovementioned sub-modes are presented in Figure 1.9. The solid and dashed lines represent the electric and magnetic walls, respectively. The half-mode SIW can be realized by cutting the full-mode SIW cavity along its symmetrical plane A-A1, as shown in Figure 1.9b. The electric field remains unchanged, and the cavity resonates at the fundamental mode with 50 % size reduction. Similarly, the quarter-mode SIW achieves 75 % as demonstrated in [35]. The eighth, sixteenth, and thirty-second sub-modes techniques achieve highly compact filters compared to other SIW miniaturization techniques with 87 %, 93 %, and 96 % size reduction, respectively [36, 37]. In [38], a novel folded ridged half-mode SIW (FRHSIW) is characterized and implemented to design two miniaturized bandpass filters. By folding the fundamental mode of a ridged half-mode SIW (RHMSIW) around the ridge as shown in Figure 1.10, miniaturization of 96 % was achieved and demonstrated by a second-order filter at 1.13 GHz with a quality factor of 132. Similarly, the folded ridged quarter-mode SIW filter was designed using the concept, obtaining 98 % with a quality factor of 128. Overall, the sub-modes techniques exhibit excellent advantages in miniaturizing SIW structure. The drawback of these techniques is that the unloaded quality factor of these sub-modes is low due to increased radiation loss at the open edges.

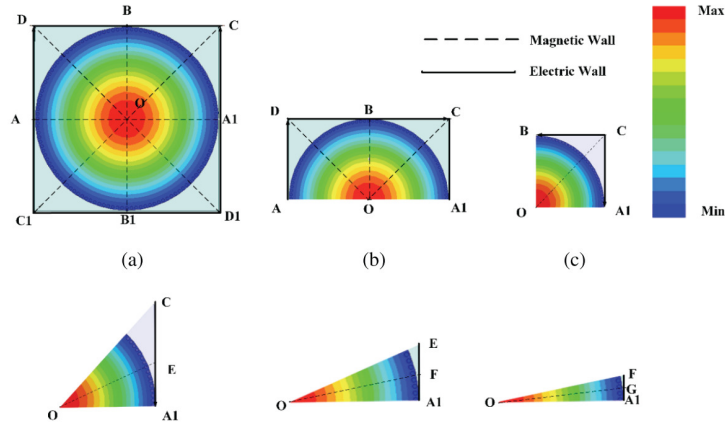


Figure 1.9: Field distribution of the circular SIW cavity resonator (a) full-mode, (b) half-mode, (c) quarter-mode, (d) eighth-mode, (e) sixteenth-mode, and (f) thirty-second-mode (from [37]).

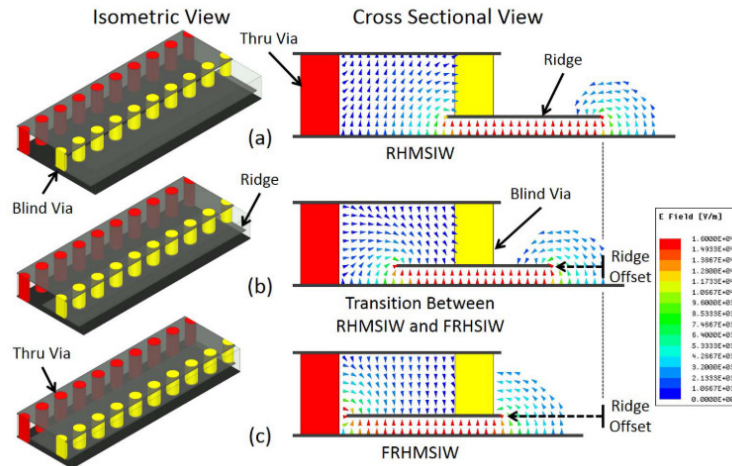


Figure 1.10: 3-D and cross-sectional views of (a) RHMSIW, (b) transition between RHMSIW and FRHMSIW, and (c) FRHMSIW along with their respective fundamental mode field patterns (from [38]).

Composite right/left handed (CRLH) resonators have been proposed in SIW technology to reduce the size of the SIW structure [39–41]. The CRLH structure is realized by series and shunt capacitance and inductance that exhibit negative refractive index allowing for much lower cutoff frequency [39]. The authors in [40] proposed CLRH structure based on SIW cavity as shown in Figure 1.11a. The CLRH structure behaves as shunt inductance and series capacitance. This circuit

configuration generates resonance below the cutoff frequency of the SIW cavity resonator. A second-order filter is designed at a center frequency of 6.1 GHz with a bandwidth of 6.5 %. The filter has an insertion loss of 1.59 dB and a quality factor of 50. A miniaturization of 45 % is achieved for the CLRH SIW filter. In [39], a CLRH unit-cell is incorporated with folded SIW resonator as shown in Figure 1.11b. The folded SIW technique is adopted to achieve 50 % miniaturization for the proposed resonator. Then, the CRLH is introduced to the structure to shift the cutoff frequency of the folded SIW down. Combining the folded and CRLH techniques in a single SIW structure enables 80 % miniaturization. A fourth-order filter is designed at a center frequency of 5.3 GHz with a 6.2 % bandwidth. The filter's insertion loss is 3.4 dB and has a quality factor of 176.

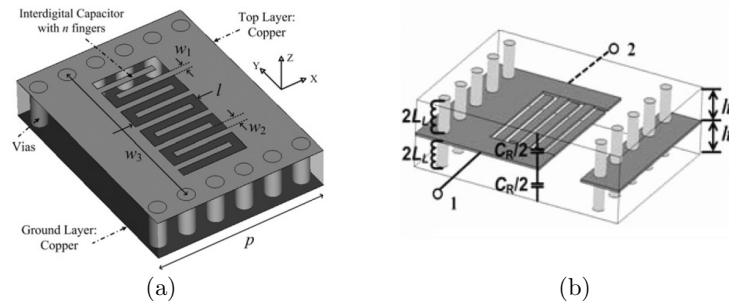


Figure 1.11: (a) Unit-cell of CLRH-based SIW cavity resonator (b) CLRH structure based on folded-SIW (from [40] and [39]).

The coaxial SIW was initially introduced in [42] as a novel topology for compact coupled resonator filters. The coaxial SIW consists of a conducting post at the center of the SIW cavity that is short-circuited at the bottom ground plane and opened at the top metallic layer using an annular gap as shown in Figure 1.12a. This short-circuited post behaves as the inner conductor of a transverse EM-mode coaxial line along the vertical substrate thickness, while the SIW via wall defines as the outer conductor of the coaxial line. The top annular gap formed the capacitance load that shifts the resonant frequency to the lower side

of the spectrum. A third-order Chebyshev filter using the proposed coaxial SIW resonator at a center frequency of 10 GHz and bandwidth of 2 %. The filter obtained an insertion loss of 3.5 dB and an unloaded quality factor of 177. The filter occupies 50 % less area than the conventional SIW implementation.

In [43], an embedded coaxial substrate integrated waveguide (ECSIW) filter is presented. Figure 1.12b depicts the embedded coaxial SIW resonator layout. The structure consists of metallic posts at the center of the square cavity connected to the ground from one end. The other end is connected to a circular metal plate below the top layer. The post diameter, length, and location in the cavity control the inductance of the cavity. The size and location of the metal patch determine the loading capacitance. To demonstrate the benefits of the structure, an in-line three-pole bandpass filter at 1.5 GHz with a 10 % bandwidth is designed in a low-temperature co-fired ceramic (LTCC) stack-up. The filter achieves 96.8 % of miniaturization with a wide spurious-free band of $7 \times f_0$. The insertion loss is 1.2 dB, and the quality factor is about 160. The quality factor is primarily affected by the dielectric material above the metal patch where the electric field is concentrated. Another example using embedded coaxial substrate integrated waveguide is presented in [44]. The authors proposed a fourth-order bandpass filter at 5.96 GHz. The structure is fabricated using standard PCB technology. By carefully tuning the design parameters, the filter obtained 96.4 % miniaturization with a quality factor of 320.

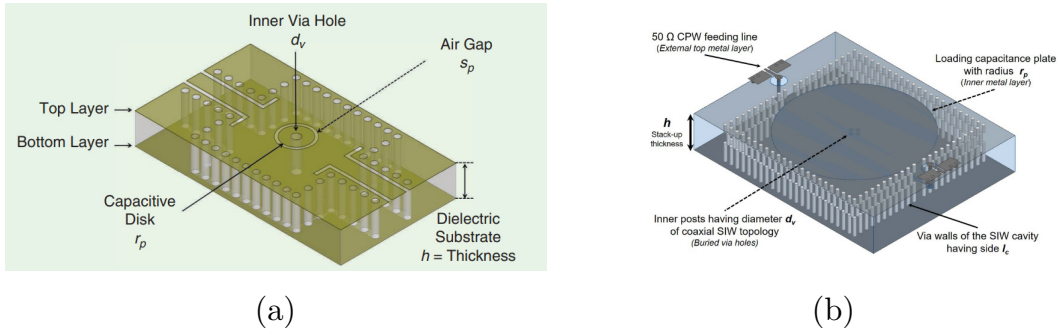


Figure 1.12: (a) Coaxial SIW cavity resonator , and (b) embedded coaxial SIW cavity resonator (from [42] and [43]).

The embedded coaxial SIW structure shows a good trade-off between the miniaturization and the quality factor compared with other structures mentioned above. The ECSIW demonstrates the capability of achieving a miniaturization factor higher than 96 % with a moderate quality factor of 320. Yet, the quality factor of ECSIW is still lower than the conventional SIW resonator. However, the quality factor can be improved by removing the dielectric material above the metal patch, eliminating the dielectric loss between the two metals, and reducing the effect of conductor loss. As a result, an air gap forms on top of the patch, which becomes the key component of a high-Q embedded loaded coaxial substrate integrated waveguide resonators and filters. This can only be obtained by overcoming the challenges of creating a thin and robust air gap structure. This research illustrates the feasibility of designing and integrating low-loss, compact, low-cost, and lightweight filters using ELCSIW cavity resonators.

1.4 Dissertation Outline

Chapter 2 presents the modeling and analysis of the proposed ELCSIW structure. Utilizing the ELCSIW resonator, a second-order ELCSIW bandpass filter is designed and implemented. Validations are given through simulated and measured

results for the second-order filter to verify the design concept. Detailed step-by-step materials selection and fabrication guidelines in standard PCB technology are provided. A comparison between the ELCSIW filter and the current state of miniaturized substrate-integrated filters is presented. Then, a mixed coupling technique to improve the stopband rejection is presented. This technique is implemented on second-order ELCSIW filters to demonstrate the feasibility of the mixed coupling in the proposed structure. Also, the power handling capability of the ELCSIW filter is investigated in this work.

Chapter 3 presents a novel post-fabrication frequency tuning mechanism for the ELCSIW filter. An investigation of the tolerances of the materials and the fabrication process is provided. Then, the circuit model and the working mechanism of the frequency tuning circuit are explained. Using the proposed tuning circuit, two mistuned ELCSIW filters are tuned back to their design frequency to demonstrate the proposed method's effectiveness.

Chapter 4 present an investigation of the capability of the ELCSIW technology to scale to Ka-band frequencies. Material selections and design guidelines at a higher frequency are presented. A second-order ELCSIW filter is designed and simulated at 30 GHz to verify the operation in Ka-band. Next, simulation results are presented for two mix-coupled ELCSIW filters at 30 GHz to demonstrate the benefit of mixed coupling on stopband rejection.

Finally, in Chapter 5, the main outcomes of the research presented in this dissertation are provided. Also, a summary of the contributions of this work and suggestions for future work are highlighted.

Chapter 2

Ultra-Miniaturized Substrate Integrated Resonators and Filters

RF/microwave filters are crucial elements in modern wireless systems. Filters are used to select RF signals and prevent unwanted signals from passing through the system. The recent developments in wireless applications continue to impose stringent requirements on RF/microwave filters and demand higher performance, compact size, lighter weight, and lower cost. In this regard, compactness and a high-quality factor are critical characteristics to be addressed for future microwave filters; hence, recent efforts have been made to further reduce the footprint of RF/microwave filters while maintaining a high-quality factor. To achieve these characteristics, selecting a suitable resonator technology is the first step in designing a microwave filter. Among RF/microwave resonator technologies, waveguides have shown the highest quality factor. However, their bulky size limits their usage in many applications. Planar transmission line technologies, such as microstrip line and coplanar waveguide, are favored over waveguide due to their ease of integration and small footprint, but at the expense of a low-quality factor due to inherent dielectric and radiation losses. On the other hand, ELCSIW resonators have the potential to achieve ultra-miniaturization capability while maintaining a high-quality factor, low cost, and low complexity.

This chapter presents the characteristics and modeling of the ELCSIW resonators. The design criteria and their trade-offs with regard to quality factors and miniaturization are highlighted. Multiple filters are designed to demonstrate the advantages of ELCSIW resonator technology. Finally, measurements and discussions of the fabricated filters are presented.

2.1 Embedded Loaded Coaxial Substrate Integrated Waveguide Resonator Modeling

Embedded loaded coaxial substrate-integrated waveguide cavity resonators have been analytically investigated and demonstrated in the literature [43–45]. Compared to previously reported resonators, the proposed ELCSIW cavity resonator achieves a higher quality factor while being ultra-miniaturized in size. The ELCSIW cavity resonator shown in Figure 2.1 comprises of a 3.37 mm dielectric substrate, a 0.069 mm prepreg, and three metallic layers. Through a copper-plated post of diameter D , the middle metallic patch is short-circuited to the bottom layer to form a highly capacitive loading coaxial cavity resonator. The prepreg is cut over the metallic patch to remove the dielectric layer and create a capacitive air-filled gap. As a result, the dielectric loss between the patch and the top layer, where the maximum electric fields are present, is eliminated. The proposed ELCSIW cavity resonator can achieve 99 % miniaturization with an overall unloaded quality factor (Q_u) of 500.

Using the eigenmode HFSS solver, the field distribution inside the proposed ELCSIW cavity resonator is simulated and depicted in Figure 2.2. It can be observed that the magnetic-field around the post has uniform ring-shaped distribution. On the top part, it can be noticed that the electric-field is strong and uniformly distributed between the patch and the cavity top. Thus, the resonator’s structure can be divided into two regions: capacitive dominant and

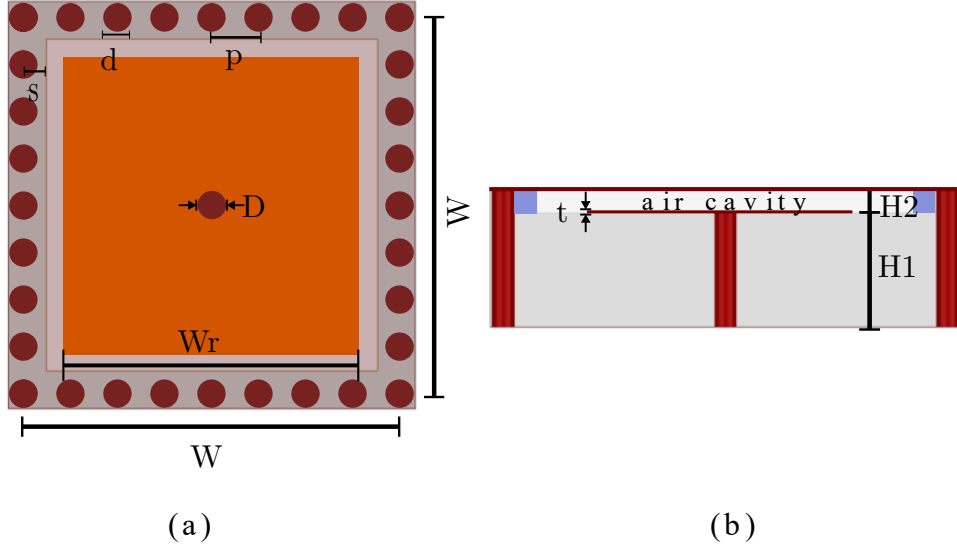


Figure 2.1: Proposed ELCSIW resonator (a) top view, and (b) cross-section view. The image is not drawn to scale and dimensions are in mm. ($W = 10$, $W_r = 7.5$, $D = 0.5$ mm, $s_1 = 0.2$, $H_1 = 3.37$, $H_2 = 0.069$, $t = 0.017$, $d = 0.5$, $p = 1$).

inductive dominant. As a result, the resonator can be modeled as short-circuited coaxial line and parallel plate capacitor, as shown in Figure 2.3. Considering the equivalent circuit model, the susceptance $B(\omega)$ of the resonator can be expressed as [45]

$$B(\omega) = \omega C_p - Y_0 \cot(\beta H_1), \quad (2.1)$$

where

$$\beta = \omega \sqrt{\epsilon_r} / c.$$

c is the speed of light in free space, and Y_0 is the characteristic admittance of the coaxial line formed by the loading patch, the posts, and the outer square via walls. The capacitance between the patch and cavity top and bottom is denoted by C_p and can be estimated using the parallel plate capacitor model. ϵ_r is the dielectric constant of the H_1 substrate.

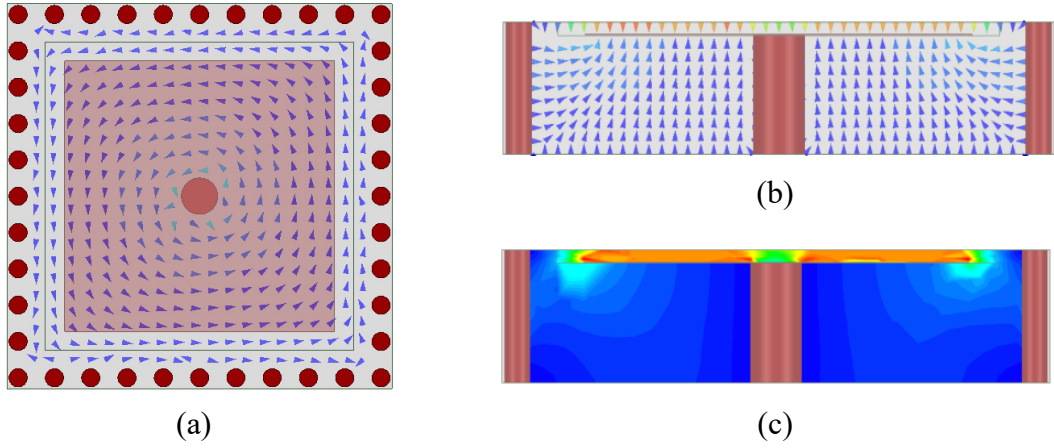


Figure 2.2: (a) Top view of the magnetic field distribution, (b) cross-section view of the electric field distribution, and (c) cross-section view of the electric field intensity inside the ELCSIW cavity. The magnetic field distribution in the lower side of the cavity resembles that of a coaxial line. The electric field is primarily concentrated between the patch and the cavity top.

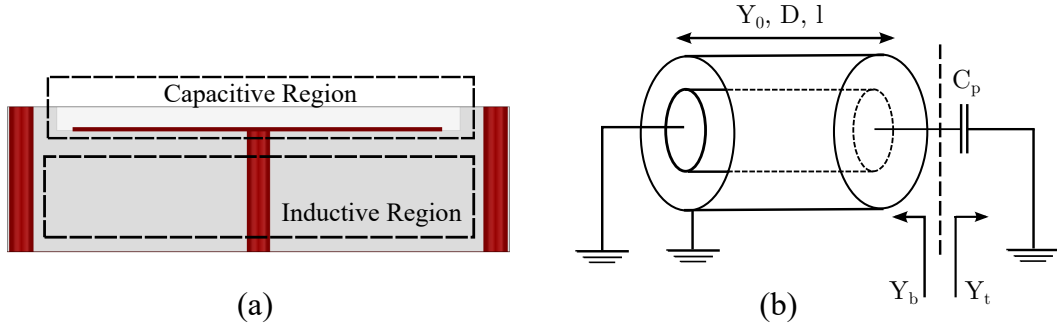


Figure 2.3: Quasi-static model of ELCSIW cavity resonator, (a) capacitive and inductive regions in ELCSIW resonator, and (b) equivalent circuit model.

At the resonance frequency,

$$B(\omega) = 0 \quad (2.2a)$$

$$Y_t + Y_b = 0 \quad (2.2b)$$

$$\omega C_p - Y_0 \cot \beta h = 0 \quad (2.2c)$$

$$\omega = \frac{Y_0 \cot \beta h}{C_p}. \quad (2.2d)$$

For thick substrates,

$$\cot(\beta H_1) \approx \frac{1}{\beta H_1}.$$

Then, the resonant frequency of the ELCSIW cavity shown in Figure 2.3 can be determined by [44]

$$f_r = \frac{1}{2\pi} \left[\frac{Y_0 c}{C_p \sqrt{\epsilon_r} H_1} \right]^{1/2}. \quad (2.3)$$

The capacitance C_p has two components; a capacitance between the patch and the cavity top (C_t) and the cavity bottom (C_b) and can be written as

$$C_p = C_t + C_b.$$

When the perpendicular fields and fringing fields are considered, C_t and C_b can be determined by [46]

$$C = \epsilon_r \epsilon_0 \frac{W_r^2}{g} \left[1 + \frac{2g}{\pi W_r} \left(1 + \ln \left(\frac{\pi W_r}{g} \right) \right) \right], \quad (2.4)$$

where W_r is the patch width and g is the separation between parallel plates which are the thicknesses of substrates H_1 and H_2 . ϵ_0 denotes the free space permittivity. The characteristic admittance of the coaxial line can be written as [45]

$$Y_0 = \frac{1}{2\pi} \left[\frac{60}{\sqrt{\epsilon_r}} \ln \left(R_{eff} \frac{W_{eff}}{D} \right) \right]^{-1}, \quad (2.5)$$

where D is the diameter of the coaxial inner conductor. R_{eff} is the outer shield factor for a coaxial line with a circular inner conductor and a square outer conductor, which is equal to 1.079 [47]. W_{eff} is the effective width of the SIW cavity

and can be written as [48]

$$W_{eff} = W - 1.08 \frac{d^2}{p} + 0.1 \frac{d^2}{W}, \quad (2.6)$$

where W is the width of the SIW cavity, d is the diameter of the wall vias, and p is the spacing between the vias.

Alternatively, the resonant frequency of the coaxial resonator can be determined using the lumped element model shown in Figure 2.4. All the lumped capacitors are assumed to be in parallel and can be expressed as

$$C_{total} = C_t + C_b + C_{coax}, \quad (2.7)$$

where C_t and C_b are determined by (2.4). C_{coax} and L_{coax} are the coaxial line parameters per unit length and can be determined by [4]

$$C_{coax} = \frac{2\pi\epsilon_0}{\ln\left(\frac{R_{eff}W}{D}\right)} \quad (2.8)$$

$$L_{coax} = \frac{\mu_0}{2\pi} \ln\left(\frac{R_{eff}W}{D}\right), \quad (2.9)$$

where μ_0 is the free space permeability.

Then, the resonant frequency of the ELCSIW resonator is determined by [4]

$$f_r = \frac{1}{2\pi\sqrt{C_{total}L_{coax}}}. \quad (2.10)$$

Figure 2.5 and Figure 2.6 compare the resonant frequency of the ELCSIW resonator found by the analytical models in (2.3) and (2.10). Figure 2.5 shows the relationship between the resonant frequency, f_r , and the air gap, H_2 , for an ELCSIW resonator with a cavity width of $W = 10$ mm, dielectric substrate

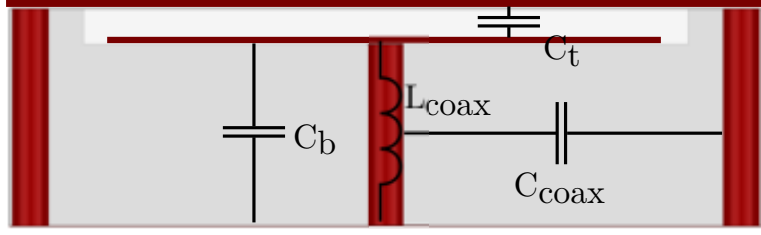


Figure 2.4: Lumped element model of an ELCSIW cavity resonator.

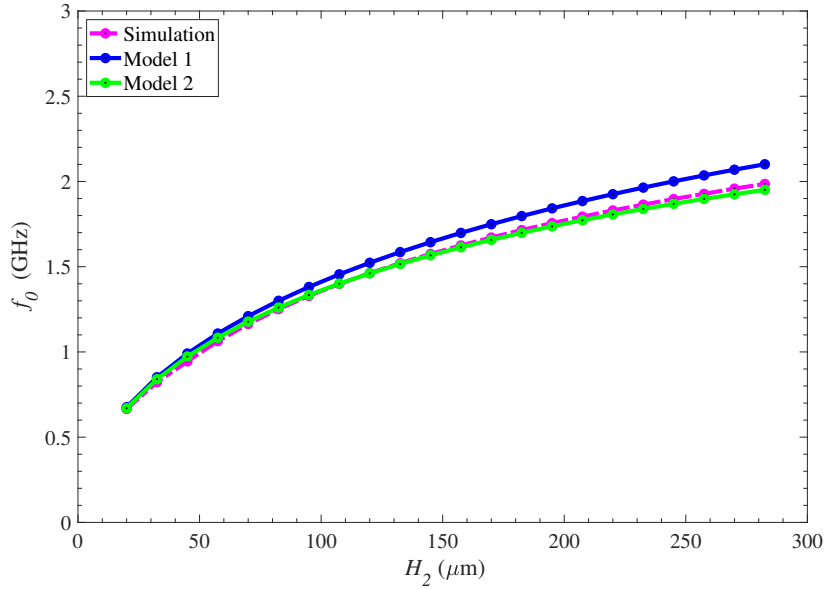


Figure 2.5: A comparison of the resonant frequency versus air gap thickness for the ELCSIW resonator shown in Figure 2.1. Simulation: eigenmode ANSYS solver solution, Model 1: Loaded coaxial line model from (2.3), Model 2: Lumped element model from (2.10).

thickness of $H_1 = 3.55$ mm, patch width of $W_r = 7.5$ mm, and post diameter of $D = 0.5$ mm. This figure includes eigenmode simulation results using the eigenmode HFSS solver as a reference. The lumped element model using (2.10) shows more accurate results over the range of H_2 . Figure 2.6 shows the relationship between f_r and patch width, W_r , for an ELCSIW resonator. In this graph, the lumped element model using (2.3) comparable results to the coaxial equivalent model over a range of W_r values. Overall, the lumped element model shows more consistent results for the resonance frequency over different parameters.

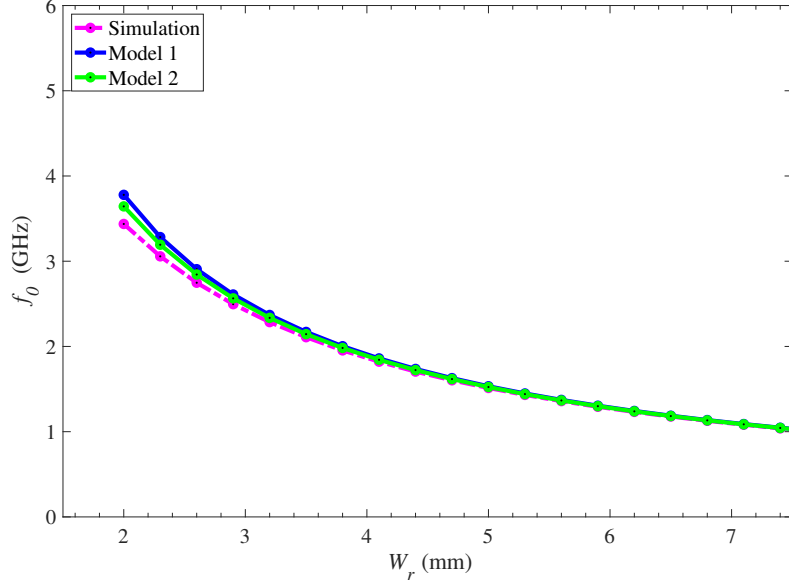


Figure 2.6: A comparison of the resonant frequency versus patch width for the ELCSIW resonator shown in Figure 2.1. Simulation: eignemode ANSYS solver solution, Model 1: Loaded coaxial line model from (2.3), Model 2: Lumped element model from (2.10).

The unloaded quality factor of the ELCSIW cavity resonator can be modeled into dielectric and conductor quality factors as [4]

$$\frac{1}{Q_u} = \frac{1}{Q_d} + \frac{1}{Q_c}, \quad (2.11)$$

where Q_d denotes the dielectric quality factor and Q_c the conductor quality factor, respectively. Q_d describes the effect of material dielectric loss and can be defined as

$$Q_d = \frac{1}{\tan\delta}. \quad (2.12)$$

where $\tan\delta$ is the loss tangent of the dielectric material. The effect of the conductor loss of the capacitors and inductors in the cavity is represented by Q_c . It considers the loss between the posts and the outside vias, the patch and the top layer, the patch and the bottom layer, and the post's inductance. A capacitor's

quality factor (Q_{cap}) can be expressed as [4]

$$Q_{cap} = \frac{1}{\omega R_s C}, \quad (2.13)$$

where ω denotes the angular frequency, R_s denotes the surface resistivity, and C is the parallel plate capacitance. Equation (2.13) can be used to determine the quality factors of the coaxial capacitance (C_{coax}), top capacitance (C_t), and bottom capacitance (C_b). The post via inductance quality factor is defined as

$$Q_{ind} = \frac{\omega L}{R_s}, \quad (2.14)$$

where L is the post via inductance.

The fact the air gap is constructed by an adhesive prepreg layer raises concern about the frequency sensitivity for the variation of air gap thickness. Due to the high pressure necessary to cure the adhesive layer, the prepreg's thickness tends

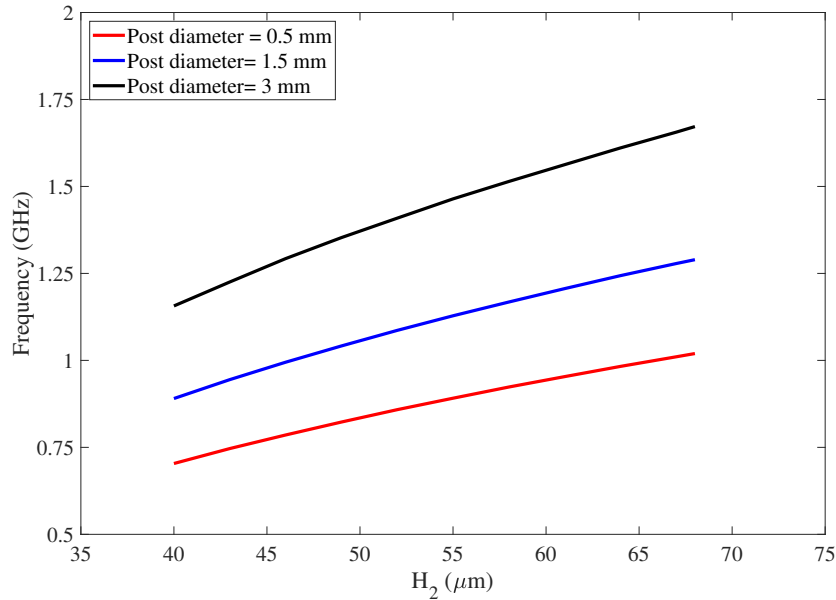


Figure 2.7: Variation in frequency as a function of the prepreg thickness at three different post sizes, demonstrating the frequency sensitivity.

to decrease during the lamination process. The amount of decrease in thickness is heavily dependent on the material selection. Therefore, full-wave eigenmode simulations were performed to determine the sensitivity of the coaxial resonator's resonant frequency with respect to the air gap thickness. The simulations were run with three different post sizes over a range of H_2 thicknesses, as shown in Figure 2.7. The cavity's dimensions are similar to those in Figure 2.1. The graph depicts a high sensitivity of the resonant frequency to H_2 fluctuation, with the frequency shifting by 4 % for every 5 μm variation in H_2 . The resonant frequency sensitivity slightly increases when the diameter of the post has increased. This offers design flexibility in regard to post size. Additional details in this regard are presented in the following sections.

One of the benefits of an ELCSIW resonator is its potential to achieve compactness. To demonstrate this benefit, the miniaturization factor (MF) is used to compare the sizes of an ELCSIW cavity resonator with an unloaded substrate integrated waveguide cavity resonator. It quantifies, in percentages, the degree of miniaturization that can be accomplished with an ELCSIW resonator operating. The factor of miniaturization can be expressed as

$$\text{Miniaturization factor (MF)} = \frac{A_{SIW} - A_{ELCSIW}}{A_{SIW}} \cdot 100 \%, \quad (2.15)$$

where A_{SIW} and A_{ELCSIW} are the area of an unloaded substrate integrated waveguide cavity resonator and an ELCSIW resonator, respectively.

The primary goal for the proposed ELCSIW design is to achieve ultra miniaturization while maintaining a high-quality factor. At a fixed cavity size, (2.3) and (2.10) suggest that the resonant frequency is affected mainly by the dielectric substrate thickness, patch width, air gap thickness, and post diameter. An analytical investigation using an eigenmode solver is performed for each parameter to evaluate their effects on the miniaturization factor and the quality

factor of the ELCSIW resonator. From Figure 2.8 to Figure 2.11, each graph shows the miniaturization factor and the quality factor over a range of values of each parameter. Figure 2.8 demonstrates that an increase in H_1 will result in higher compactness. This effect is anticipated by (2.10), which indicates that an increase in H_1 will increase the coaxial line inductance, hence decreasing the resonant frequency. Furthermore, the graph illustrates that increasing H_1 allows for a higher quality factor. This increase in Q_u can be attributed to the cavity becoming larger in volume, increasing stored energy capacity. Also, the figure illustrates that increasing the thickness of H_1 over 3 mm has a small impact on the miniaturization and quality factor of the ELCSIW cavity. This indicates that the optimal thickness range of the dielectric substrate is between 2.5 mm to 3.5 mm, as raising the thickness increases the overall volume and production cost without significant improvement on performance.

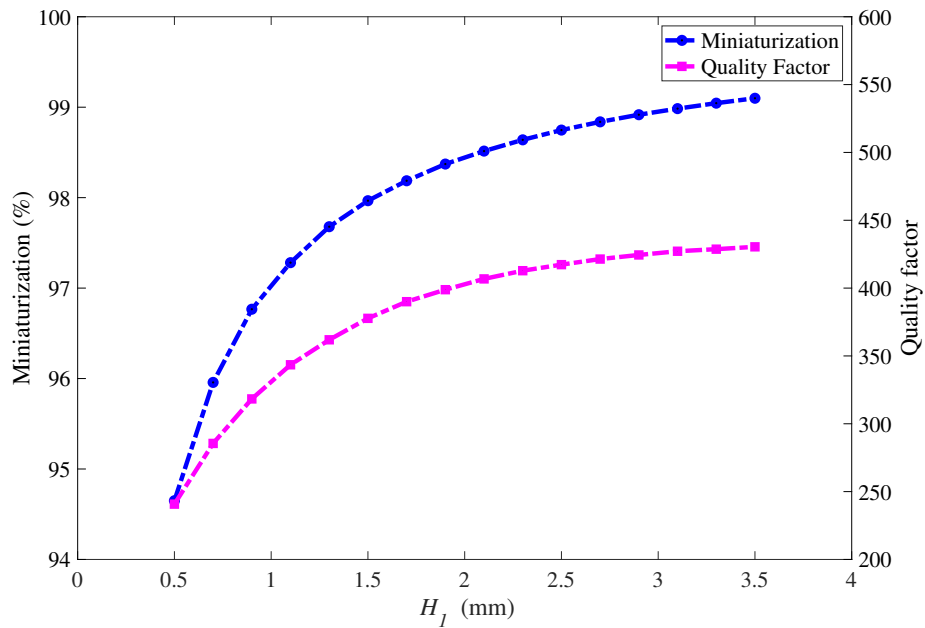


Figure 2.8: Miniaturization factor and quality factor of the ELCSIW resonator versus dielectric substrate thickness (H_1).

In Figure 2.9, the miniaturization factor increases as the patch width increases

due to increasing the capacitance between the patch and the cavity top (C_t). On the other hand, the quality factor declined by more than 35 % across the entire range. As the patch size increases, the electric field concentration between the patch and the cavity top increases, increasing the conductor loss and lowering the quality factor. In Figure 2.10, the effect of the air gap thickness variation on the ELCSIW resonator is investigated. As seen in (2.10), the air gap is inversely proportional to the capacitance C_t , implying that decreasing the air gap allows for a higher miniaturization factor. Furthermore, the quality factor increases exponentially with increasing H_2 before beginning to decline at 150 μm of air gap thickness. This trend suggests that the air gap of the ELCSIW resonator should be in the range between 70 μm to 100 μm to optimize the quality factor and maintain a high miniaturization factor. Figure 2.11 demonstrates that lower post diameters provide a higher miniaturization factor, whereas larger diameter sizes improve the quality factor.

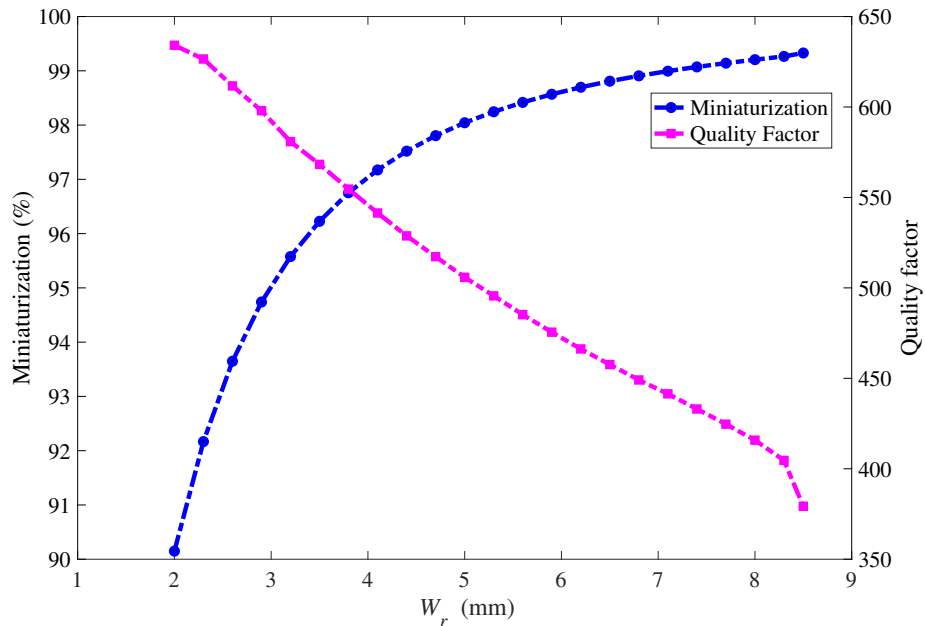


Figure 2.9: Miniaturization factor and quality factor of the ELCSIW resonator versus patch width (W_r).

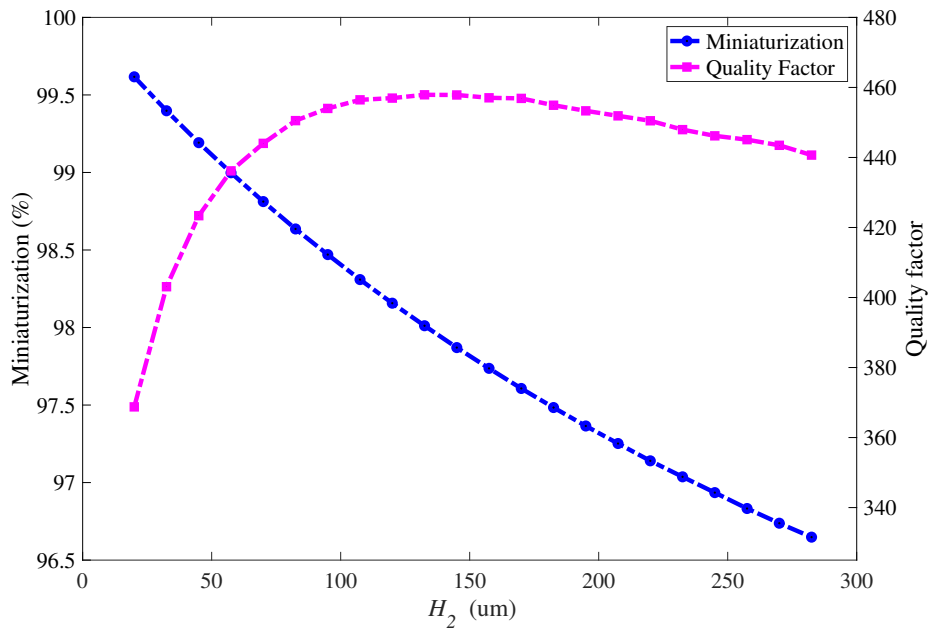


Figure 2.10: Miniaturization factor and quality factor of the ELCSIW resonator versus air gap (H_2).

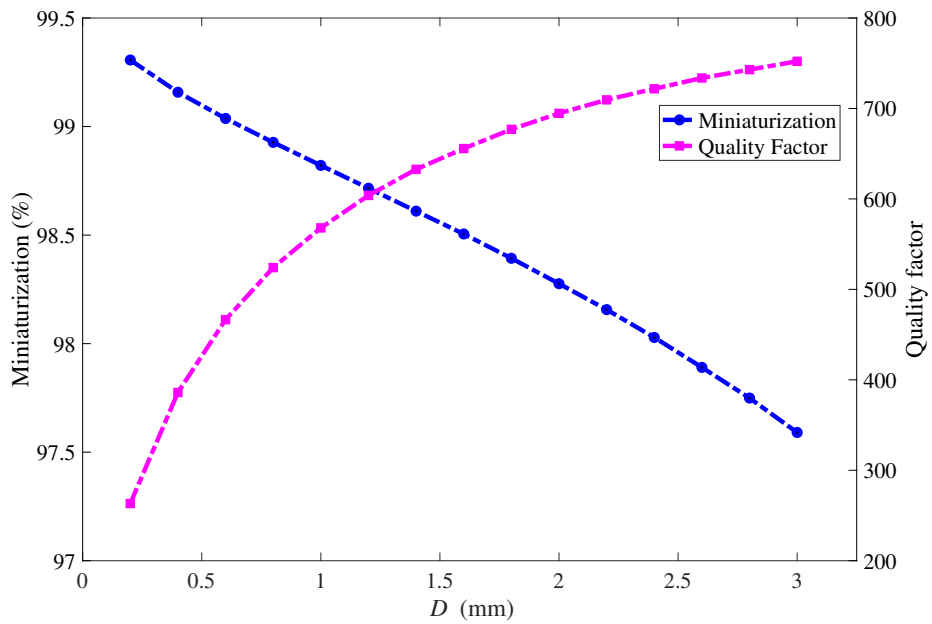


Figure 2.11: Miniaturization factor and quality factor of the ELCSIW resonator versus post diameter (D).

In summary, the cavity parameters analysis for the quality factor and miniaturization yields a few recommendations. To begin, the dielectric substrate thickness should be about 3 mm in order to achieve the maximum miniaturization factor and quality factor. Second, to fully benefit from the capacitive loading between the patch and the cavity top, the patch width should be maximized. Figure 2.12 and 2.13 provide two comparisons of the air gap thickness and the post diameter in terms of MF and Q_u to determine their optimal dimensions. Figure 2.12 demonstrates that more than 99 % miniaturization factor can be attained using posts with a diameter up to 2.0 mm at an air gap thickness of 40 μm . This range of posts offers a quality factor between 300 and 620. However, the optimal dimensions for the air gap are constrained by the prepreg thicknesses available on the market which will be discussed in depth in the ELCSIW resonator design section.

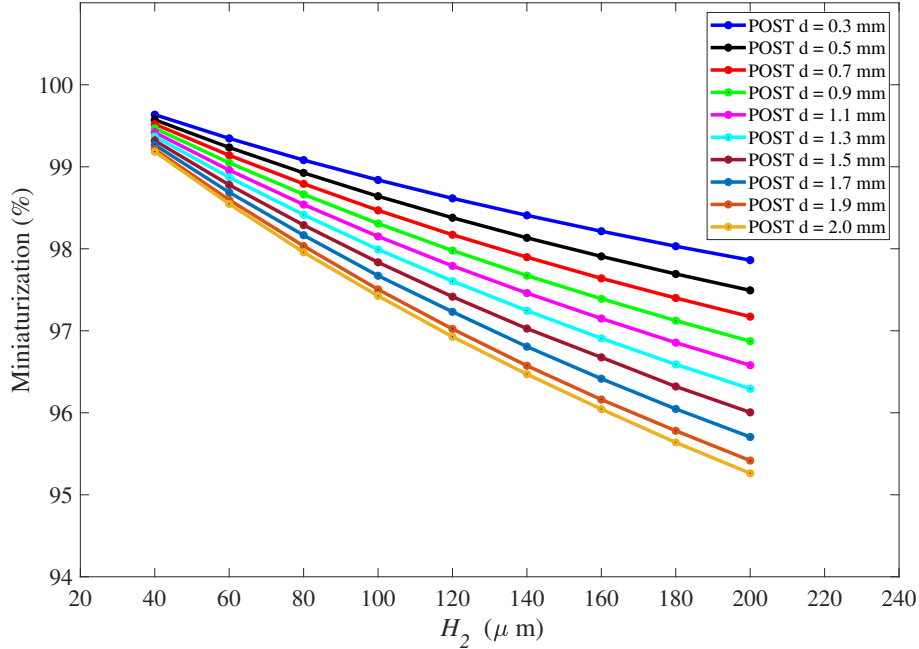


Figure 2.12: The miniaturization factor as function of H_2 for multiple post diameters values.

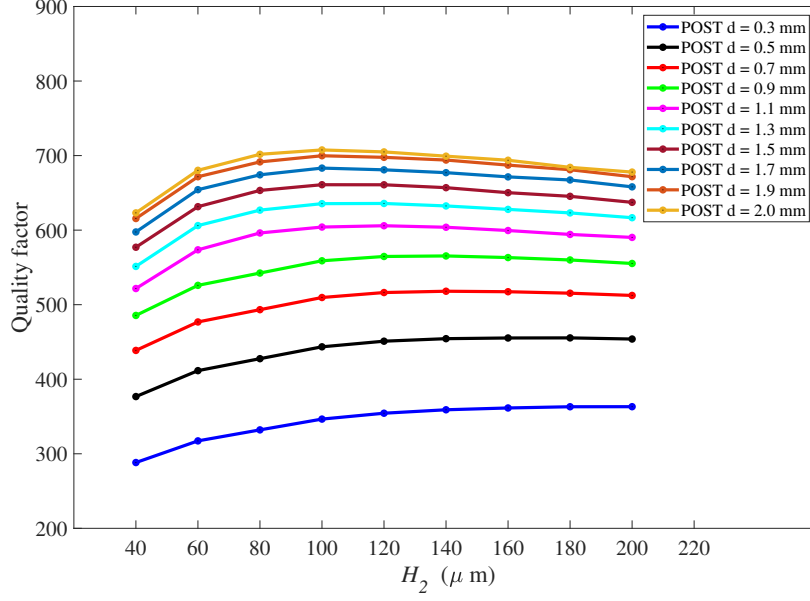


Figure 2.13: The unloaded quality factor as function of H_2 for multiple post diameters values.

The unloaded quality factor analysis performed here assumes the copper conductivity of all metallic surfaces is 5.8×10^7 S/m. This assumption does not hold in practice, especially when considering in-house fabrication, which involves manual fabrication process steps and a flawed electroplating process. These imperfections are the results of surface roughness and non-uniformity of the electroplated copper. The electroplating process is a controlled electrodeposition process that coats the surfaces of the substrate and the walls of drilled vias with the desired copper thickness. This procedure does not result in a smooth copper surface. The copper roughness of the acid copper electroplating process could exceed $10 \mu\text{m}$ as reported in [49]. Several criteria, such as the condition of the electrolyte solution and the rate of copper deposition during electroplating, affect the roughness of copper surfaces. Consequently, this imperfection in the copper coating can decrease the quality factor of the cavity resonator. This decrease is attributable to the conductor loss at the surface of posts and outer vias, where

currents pass through the top, patch, and bottom metallic layers. Thus, a parametric analysis is performed to demonstrate the effect of copper surface roughness on the ELCSIW cavity resonator quality factor. The simulations are performed on the sample cavity resonator in Figure 2.1 using the eigenmode HFSS solver and shown in Figure 2.14. These simulations account for the in-house copper electroplating on the post and outer cavity vias. As the manufacturer suggests, the patch, top, and bottom copper layers are assumed to have $2\ \mu\text{m}$ of surface roughness since they don't receive the in-house copper coating. In Figure 2.14, the quality factor of an ELCSIW resonator can suffer a considerable drop in the case of higher surface roughness. At $5.8 \times 10^7\ \text{S/m}$ of conductivity and $10\ \mu\text{m}$ surface roughness, the resonator can only achieve 70 % of its best quality factor of 440.

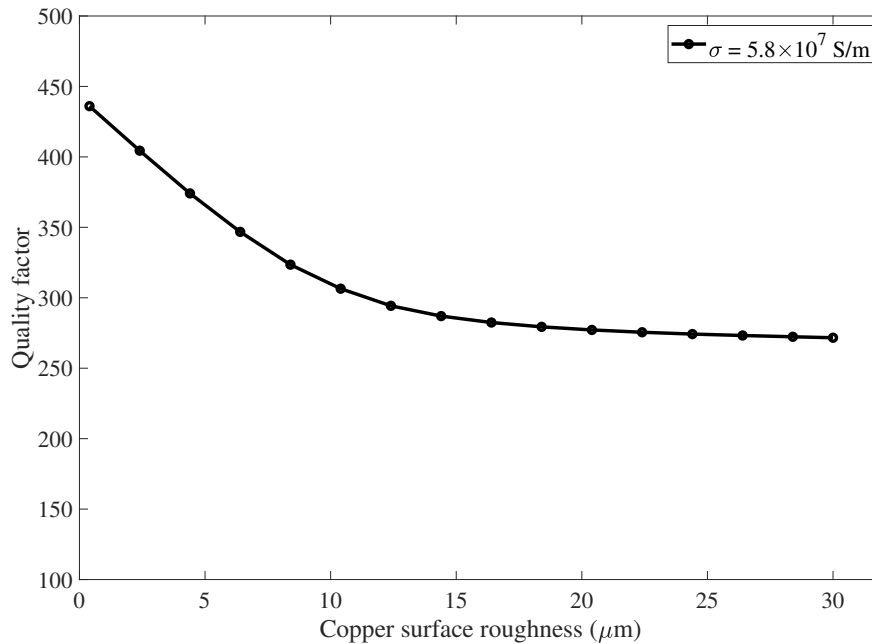


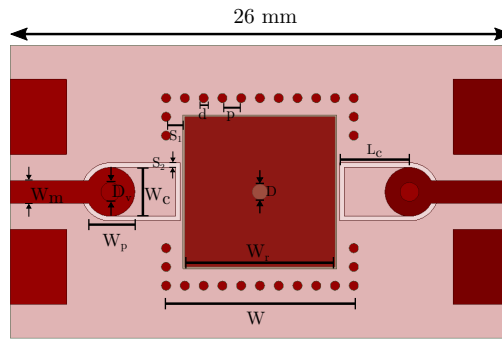
Figure 2.14: The unloaded quality factor as a function of copper surface roughness at $5.8 \times 10^7\ \text{S/m}$ copper conductivity for the ELCSIW resonator in Figure 2.1.

2.2 Embedded Loaded Coaxial Substrate-Integrated Waveguide Resonator

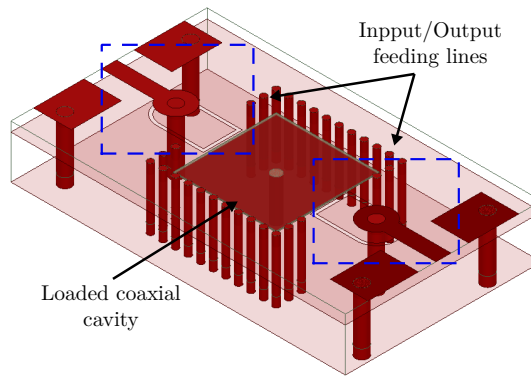
An embedded loaded coaxial substrate integrated waveguide cavity resonator is developed in this section to demonstrate the proposed concept's advantages. This resonator serves as a building block for ELCSIW filters. The resonator is designed to operate in the lower L band frequency. The goal of the proposed ELCSIW resonator is to achieve 99 % of miniaturization, and an estimated quality factor of 500. The full-wave HFSS solver is used to implement the design. The fabrication method is based on standard PCB processing. The structure of the ELCSIW cavity resonator is shown in Figure 2.15. It is composed of an input and output feeding line, a capacitively loaded cavity, and an outer via cage. The feed line is formed using a microstrip line connected to a coplanar waveguide through a vertical via transition. The cavity contains a copper-plated post connecting a metal patch to the cavity's bottom. The air cavity above the patch is created using a prepreg layer. The ELCSIW cavity resonator is formed by connecting the top and bottom metal layers with a cage of copper-plated vias. In this section, The structure of the embedded loaded coaxial substrate-integrated waveguide resonator is explained, and the materials selection guidelines are outlined.

2.2.1 Material Selection

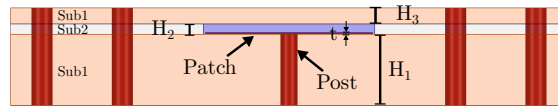
The theoretical analysis performed in section 2.1 imposes no constraints on the dimensions of the coaxial cavity resonator's design parameters. In reality, fabrication limitations such as lab equipment capabilities and availability of PCB materials continue to be a challenge. In addition, the properties of available the PCB materials, such as loss tangent and thermal expansion coefficient, contribute significantly to the quality of the fabrication process. In order to optimize the fabrication process and increase its likelihood of success, material selection



(a)



(b)



(c)

Figure 2.15: Design illustration of the ELCSIW cavity resonator, (a) the top view, (b) a 3D structure view, and (c) side view.

guidelines are presented in this section.

One of the objectives of the proposed design is to have a high-quality factor. As demonstrated in (2.11) and (2.12), the dielectric loss significantly affects the resonator's total unloaded quality factor. The initial Sub1 selection should therefore have a low-loss tangent. According to the analysis in Figure 2.8, Sub1 is preferable to have 3 mm+ of thickness to attain high quality and miniaturization factors. Yet, thinner substrates can be adapted to build ELCSIW cavities with the cost of low quality and miniaturization factors. The exact thickness

is controlled by the PCB materials available. The manufacturer offers dielectric substrates at certain thickness values, which might not match the desired thickness of Sub1. Thus, multiple substrates could be stacked using prepreg layers to get the desired thickness. An advantage of stacking substrates is the flexibility to implement the external and internal coupling circuits of ELCSIW filters into Sub1 at varying heights, hence allowing for the control of coupling strength. This is explained in detail in section 2.3. The drawbacks of stacking substrates are that it increases manufacturing costs and restricts Sub1 thickness selections.

Furthermore, manufacturers provide a range of copper cladding thicknesses for the dielectric substrate. To prevent increasing the surface resistivity, it is critical to evaluate the influence of the skin depth of the copper traces at the resonant frequency. At the resonance frequency, the copper cladding must be at least three times greater than the skin depth of the traces [50]. The skin depth at the resonant frequency is expressed as

$$\delta = \sqrt{\frac{2\rho}{2\pi f_r \mu}}, \quad (2.16)$$

where f_r denotes the resonant frequency (Hz), μ denotes permeability (Henry/m) and ρ denotes copper bulk resistivity ($\Omega\text{-m}$). The skin depth is about $2.0 \mu\text{m}$ at 1 GHz resonant frequency, which is substantially lower than the two standard copper clads. As a result, the $17.5 \mu\text{m}$ is sufficient for the proposed design. Additionally, the thickness of the copper clad affects the capacitive loading in the ELCSIW cavity. The effective air gap is determined by the thickness of the prepreg and the patch metal and is defined as

$$H_{airgap} = H_2 - t,$$

where H_2 is the thickness of the prepreg used to create the air cavity and t

denotes the copper thickness of the metal patch.

When selecting dielectric materials, it is also essential to evaluate the stiffness of the materials. During the lamination of the Sub1, Sub2, and Sub3, as depicted in Figure 2.16, a portion of the Sub3 above the air cavity is susceptible to bending due to the high pressure and high temperature. This bending significantly affects the capacitive loading as the air gap will be partially reduced. As a result, Sub3 should be chosen to have a lower risk of bending at high pressures. Flexural strength is used to identify this property in the materials data sheet. Flexural strength is the capability of a dielectric material to resist physical stress without fracturing, and it is measured in pounds per square inch (kpsi). This means that the material with a lower flexural strength is less likely to bend.

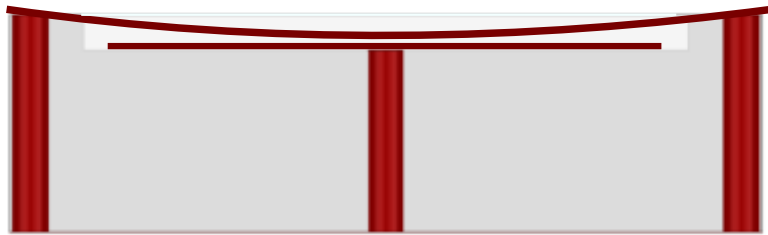


Figure 2.16: The effect of the lamination process on the air gap thickness.

The stacked materials will undergo a thermal lamination procedure during the fabrication process at a high temperature. Based on its coefficient of thermal expansion (CTE), the dielectric material will expand in the x, y, and z directions. Since the production process involves copper electroplating, the CTE of the desired dielectric material should be chosen as close as possible to the thermal expansion coefficient of copper, which is 15 ppm/K° . This requirement minimizes the risk of introducing fractures or imperfections in the plated copper during lamination, which could lead to device failure.

Table 2.1 compares various substrate materials for the ELCSIW resonator design depending on the aforementioned criteria. Thermoset Microwave Material (TMM3) exhibits most of the desired properties for the suggested design.

While other materials, such as RO3003 and RT5880, have a low loss tangent, TMM3 has a lower CTE, in the z-direction in particular, and higher flexural strength, which is critical for avoiding lamination failure. Sub1 is recommended to have a minimum thickness of 3 mm and multiple stacked substrates to provide implementation flexibility for the internal and external coupling circuits. This will require stacking three substrates of thicknesses 1.27 mm, 0.635 mm, and 1.27 mm. For Sub3, the available thickness that meets its requirements is 0.635 mm.

Table 2.1: Comparison of selected available PCB lamination materials.

Materials	ϵ_r	$\tan\delta$	Coefficient of Thermal Expansion in (x,y,z)-direction (ppm/K)	Flexural Strength (kpsi)
RO3003	3	0.001	(17,16,25)	-
RO4003	3.55	0.0021	(11,14,46)	40
RO4350B	3.66	0.0031	(10,12,32)	37
TMM3	3.45	0.002	(15,15,23)	16
RT5880	2.2	0.0009	(22,28,237)	97

For the prepreg layer, the same criteria as previously mentioned must be fulfilled. Table 2.2 compares the available prepreg materials for the resonator's design. Among these prepreg materials, SpeedWave 300P closely matches the copper coefficient of thermal expansion and hence is suitable for bonding the Sub1 substrates. The available thickness of SpeedWave 300P prepreg is 0.1016 mm (4 mils). In comparison, Sub2 requires a prepreg that can maintain its thickness during lamination to achieve the desired air gap thickness. A large percentage of prepreg materials have a high resin flow, which is desirable for enhancing adhesion between bonding layers. However, high resin flow prepreg materials are not suitable for constructing air cavities. Isola FR406N is a unique material that allows for minimal resin flow and consistency in lamination. This material is

available in thicknesses of 0.043 mm (1.7 mils) and 0.069 mm (2.7 mils). For the proposed design, a thickness of 0.069 mm of ISOLA FR406N meets the design specifications.

Table 2.2: Comparison of selected available prepreg materials.

Materials	ϵ_r	$\tan\delta$	Coefficient of Thermal Expansion in (x,y,z)-direction (ppm/K)	Thickness (mm)
RO4450T	3.26	0.0037	(18,18,58)	0.063,0.0762, 0.0889, 0.1016
RO1200	2.99	0.0012	(29,29,29)	0.063,0.0762, 0.1016
RO2929	2.94	0.003	(50,50,50)	0.0381, 0.0508, 0.0762
SpeedWave 300P	3.16	0.0021	(15,15,35)	0.0508, 0.063,0.0762, 0.0889, 0.1016
Isola FR406N (low-flow)	4.3	0.025	(17,20,75)	0.043, 0.069

2.2.2 Effective Dielectric Constant and Loss Tangent

Figure 2.17 shows the stack-up of the Sub1, which consist of three TMM3 dielectric substrates and two SpeedWave 300P prepregs. The prepreg is chosen to have electrical properties that match the TMM3 dielectric substrate as closely as possible. TMM3 substrate has a dielectric constant (ϵ_{r1}) of 3.45 and loss tangent ($\tan\delta_1$) of 0.002, and SpeedWave 300 prepreg has dielectric constant (ϵ_{r2}) of 3.16 and loss tangent ($\tan\delta_2$) of 0.0021. Due to electrical properties differences, the combination of TMM3 substrates and SpeedWave prepregs will be represented by a single homogeneous substrate with effective dielectric constant (ϵ_{reff}) and loss tangent ($\tan\delta_{reff}$), as illustrated in Figure 2.17b. These electrical parameters are utilized to calculate the resonant frequency and quality factor of the ELCSIW resonator, as explained in the section 2.1. The effective electrical properties of

the stack-up (Sub1) are defined by the thickness of each layer and its characteristics. Weighted averages or eigenmode simulations can be used to predict the effective dielectric constant and loss tangent. First, the effective dielectric constant and loss tangent using weight average is estimated by

$$\epsilon_{eff} = \frac{\epsilon_{r1}(h_1 + h_3 + h_5) + \epsilon_{r2}(h_2 + h_4)}{h_1 + h_2 + h_3 + h_4 + h_5} \quad (2.17)$$

and

$$\tan\delta_{eff} = \frac{\tan\delta_2(h_1 + h_3 + h_5) + \tan\delta_2(h_2 + h_4)}{h_1 + h_2 + h_3 + h_4 + h_5}. \quad (2.18)$$

The effective dielectric constant and loss tangent of Sub1 using the weighted average method is found to be 3.432 and 0.002006, respectively. For an accurate estimate of the effective dielectric constant of the stack-up layers, eigenmode simulation is performed at the resonant frequency of 1 GHz for the resonator sample in Figure 2.17a using TMM3 substrates and SpeedWave prepreg with dielectric constants of 3.45 and 3.16, respectively. Then, parametric analysis for the effective dielectric constant is carried out using eigenmode simulations for the sample resonator in Figure 2.17b. The dielectric constant of the single homogeneous substrate is varied from 3.25 to 3.5, and the corresponding operating frequency is obtained. Then, the operating frequency is normalized to the resonant frequency of sample resonator Figure 2.17a and plotted with respect to the effective dielectric constant in Figure 2.18. The effective dielectric constant of Sub1 using the eigenmode extraction method is found to be 3.426. Similarly, the effective loss tangent can be extracted from the quality factor of the sample resonator using eigenmode simulations. For the presented stack-up, the prepregs layers and dielectric substrates have minimal loss tangent differences and therefore have negligible impact on the effective loss tangent.

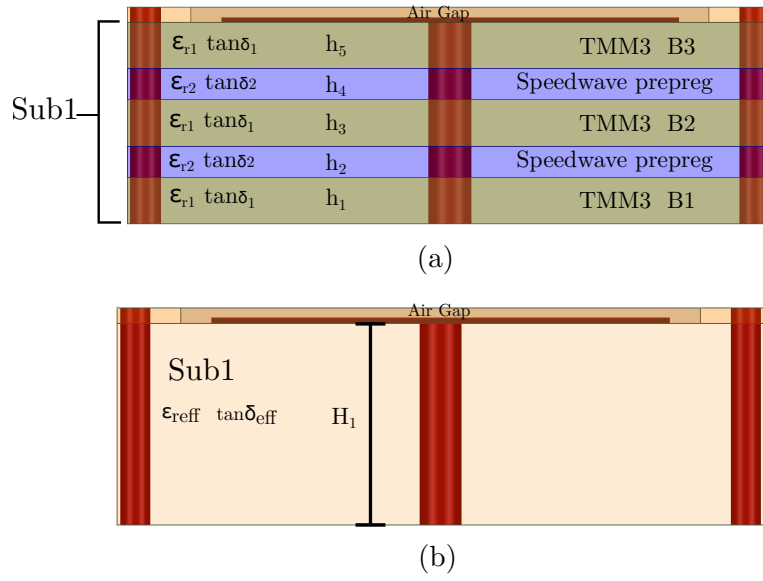


Figure 2.17: (a) Side view of the stack-up layers of the ELCSIW cavity resonator, (b) side view of the single homogeneous substrate with an effective dielectric constant (ϵ_{ref}) and loss tangent ($\tan\delta_{ref}$). Note that some wall vias of the cavity are not shown for clarity. All dimensions are in mm, and the image is not drawn to scale. ($h_1 = 1.27$, $h_2 = 0.1016$, $h_3 = 0.635$, $h_4 = 0.1016$, $h_5 = 1.27$, $H_1 = 3.3782$).

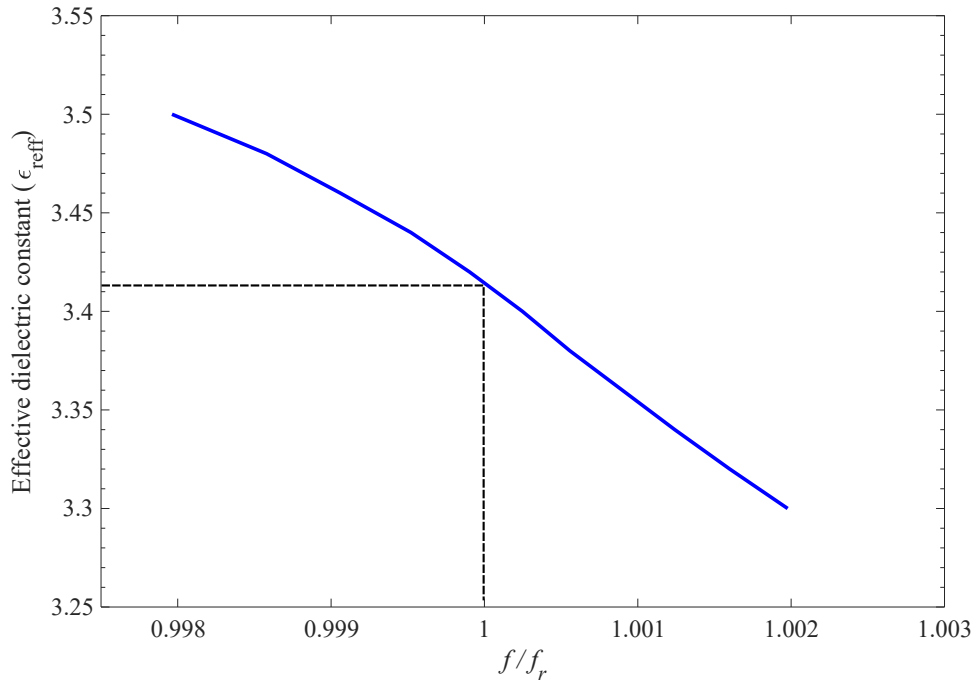


Figure 2.18: Effective dielectric constant of Sub1 versus the normalized frequency with respect to the design resonant frequency of 1 GHz.

2.2.3 Resonator Design

The proposed ELCSIW cavity resonator is designed at the lower L-band frequency, following the guidelines listed in sections 2.1 and 2.2.1. Figure 2.19 depicts the stack-up of the resonator layers. The resonator is fed by a 50Ω microstrip line that is connected to a coplanar waveguide through a vertical transition via. The cavity dimensions and substrate thicknesses are listed in Table 2.3.

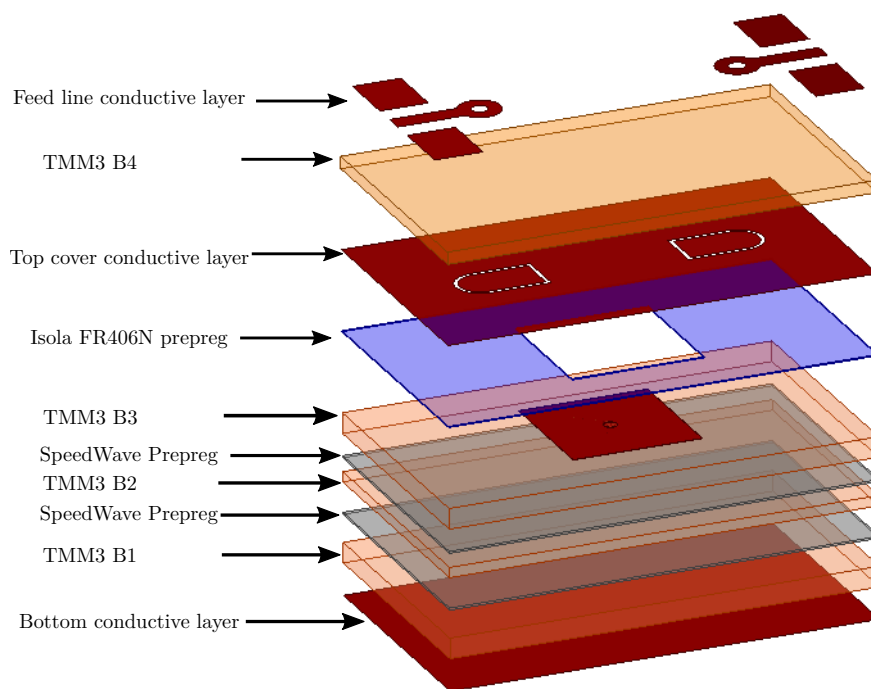


Figure 2.19: 3D view of the stack-up layers of the ELCSIW cavity resonator. Note that the vias of the ELCSIW cavity are not shown for clarity.

The transmission coefficient (S_{21}) of the full-wave HFSS simulation for the proposed resonator is shown in Figure 2.20. The resonator is weakly coupled, and its unloaded quality factor can be extracted using [50]

$$Q_u = \frac{Q_l}{1 - |S_{21}|}, \quad (2.19)$$

where,

$$Q_l = \frac{f_r}{\Delta f_{3dB}}.$$

Δf_{3dB} is the bandwidth at which S_{21} is lower by 3 dB from the maximum value at the resonance frequency.

Table 2.3: Resonator design parameters. All dimensions are in mm.

Design Parameter	Value
Cavity length (W)	10
Patch width (W_r)	8
Post diameter (D)	0.8
Coplanar waveguide width (W_c)	2.6
Microstrip line width (W_m)	1.2
Microstrip pad (W_p)	2.6
Vertical via transition diameter (D_v)	1
Air cavity to via spacing (S_1)	0.9
Coplanar waveguide length (L_c)	3.7
Coplanar waveguide gap (S_2)	0.25
Outer via diameter (d)	0.5
Outer via spacing(p)	1
Bottom substrate thickness (H_1)	3.378 (133 mils)
Isola prepreg thickness (H_2)	0.0685 (2.7 mils)
Top substrate thickness (H_3)	0.635 (25 mils)
Copper clad thickness (t)	0.0175
SpeedWave prepreg thickness	0.1016 (4 mils)

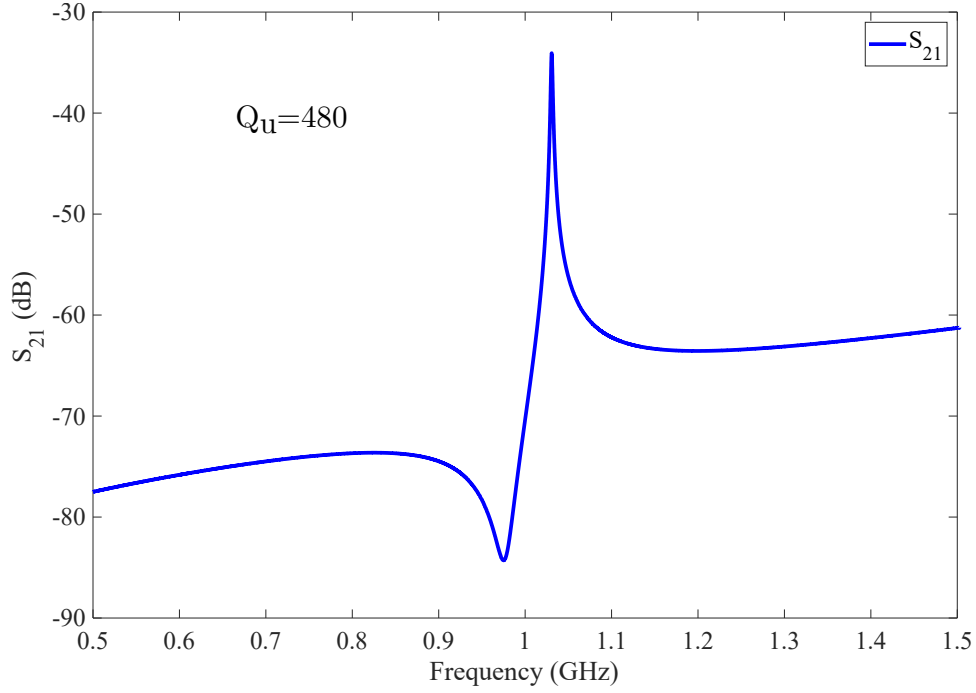
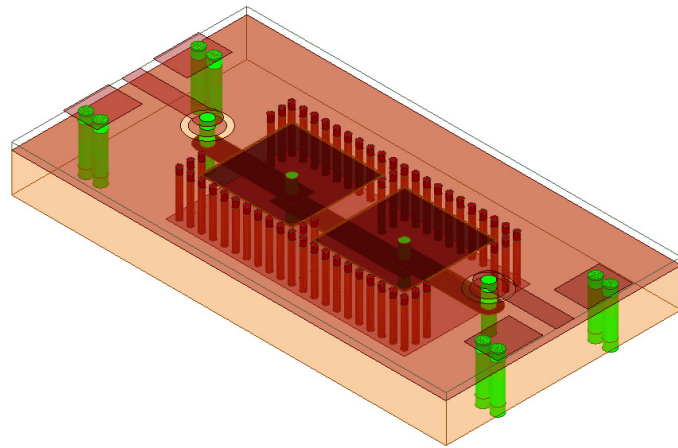


Figure 2.20: The transmission coefficient (S_{21}) of a weakly coupled ELCSIW cavity resonator.

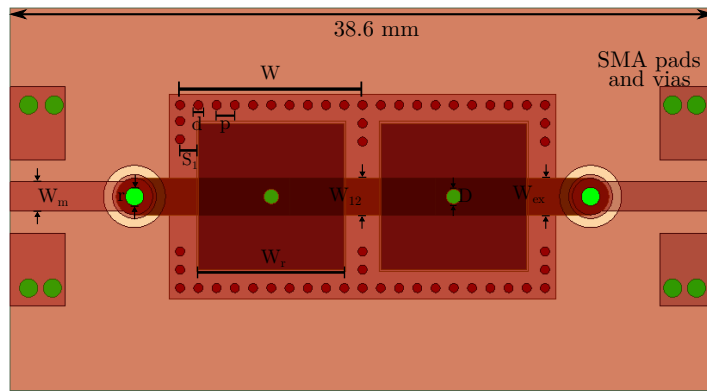
The proposed ELCSIW cavity resonator has dimensions of $10.5 \text{ mm} \times 10.5 \text{ mm}$, or $0.067\lambda_g \times 0.067\lambda_g$. Compared to a conventional SIW cavity resonator, this cavity size has achieved a miniaturization factor of 99.9 %. In addition, the ELCSIW cavity resonator has a quality factor of 480. These features illustrate the advantages of the proposed ELCSIW technology for developing and constructing compact filters that meet the requirements of future modern communications systems.

2.3 Second-Order Embedded Loaded Coaxial Substrate-Integrated Waveguide Filter

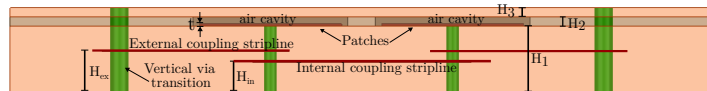
A second-order Chebyshev ELCSIW filter is developed to demonstrate the proposed concept at the L-band frequency. The filter is designed to operate at an arbitrary 1.1 GHz to validate the fundamental principle and benefits at a low microwave frequency. Two ELCSIW resonators are placed adjacent to each other



(a)



(b)



(c)

Figure 2.21: Design illustration of the second-order ELCSIW filter, (a) a 3D structure view, (b) top view, and (c) side view. The image is not drawn to scale.

to form the filter, as shown in Figure 2.21. The filter has 70 MHz bandwidth, or 6.3 % of fractional bandwidth, and an equi-ripple of 20 dB. The input/output feed lines consist of 50Ω microstrip lines connected to tap striplines through vertical transition vias. These tap striplines are short-circuited to the post of the resonator and allow for magnetic coupling to the cavity. The filter achieves 99 % percent miniaturization, which provides an integration advantage for RF substrates.

The design procedure for the second-order ELCSIW filter is demonstrated as follows:

1. Obtain the filter design specifications and determine its external and internal coupling coefficients.
2. Select the stack-up materials and the adhesive prepreg that meet the guidelines explained in section 2.2.1.
3. Design 50Ω microstrip lines given the materials selection and their thicknesses in step 2.
4. Design the microstrip lines to striplines vertical via transitions to mitigate the discontinuity effect of the vias on the input/output signal path.
5. Design the tap striplines for the external coupling to attain the designed coupling coefficient.
6. Design the tap striplines for the internal coupling to attain the designed coupling coefficient.
7. Design the cavity parameters to achieve the desired miniaturization using (2.4), (2.7), (2.8), (2.9), (2.10), and (2.15).
8. Simulate the filter using the full-wave HFSS solver and tune the cavity parameters to obtain the desired resonant frequency and bandwidth of the second-order filter.

The coupling coefficient and the external coupling of an n^{th} filter can be determined by [50]

$$\begin{aligned}
 M_{i,j+1} &= \frac{FBW}{\sqrt{g_i \cdot g_{i+1}}} \\
 Q_{e1} &= \frac{g_0 \cdot g_1}{FBW} \\
 Q_{en} &= \frac{g_n \cdot g_{n+1}}{FBW},
 \end{aligned} \tag{2.20}$$

where FBW is the fractional bandwidth of the filter and g_i are lowpass prototype coefficients for the desired filter shape. The g -values of the n^{th} degree Chebyshev function can be obtained by [50]

$$\begin{aligned}
g_0 &= 1.0 \\
g_1 &= \frac{2}{\gamma} \sin\left(\frac{\pi}{2n}\right) \\
g_i &= \frac{1}{g_{i-1}} \frac{4 \sin\left[\frac{(2i-1)\pi}{2n}\right] \cdot \sin\left[\frac{(2i-3)\pi}{2n}\right]}{\gamma^2 + \sin^2\left[\frac{(i-1)\pi}{n}\right]} \text{ for } i = 2, 3, \dots, n \\
g_{n+1} &= \begin{cases} 1.0 & \text{for } n \text{ odd} \\ \coth^2\left(\frac{\beta}{4}\right) & \text{for } n \text{ even} \end{cases}
\end{aligned} \tag{2.21}$$

where

$$\begin{aligned}
\beta &= \ln\left[\coth\left(\frac{L_{Ar}}{17.37}\right)\right] \text{ and} \\
\gamma &= \sinh\left(\frac{\beta}{2n}\right),
\end{aligned}$$

where L_{Ar} is the passband ripple. The Chebyshev polynomial coefficients, the calculated inter-resonator coupling coefficient, and external coupling for the second-order ELCSIW filter are listed in Table 2.4.

Table 2.4: The filter's Chebyshev polynomial coefficients, inter-resonator coupling coefficient, and the external quality factor of of the second-order Chebyshev ELCSIW filter.

g_0	g_1	g_2	g_3	k_{12}	Q_{ex}
1	0.6667	0.5455	1.2222	0.0779	10.48

Following material selection guidelines, the selected substrate material is Rogers TMM3, and the adhesive prepreg is SpeedWave 300P. The air cavity is constructed on a low-flow Isola FR406N prepreg. The stacked-up layers of the second-order ELCSIW filter are shown in Figure 2.22.

The microstrip lines are designed on the top copper surface of Substrate 4 with

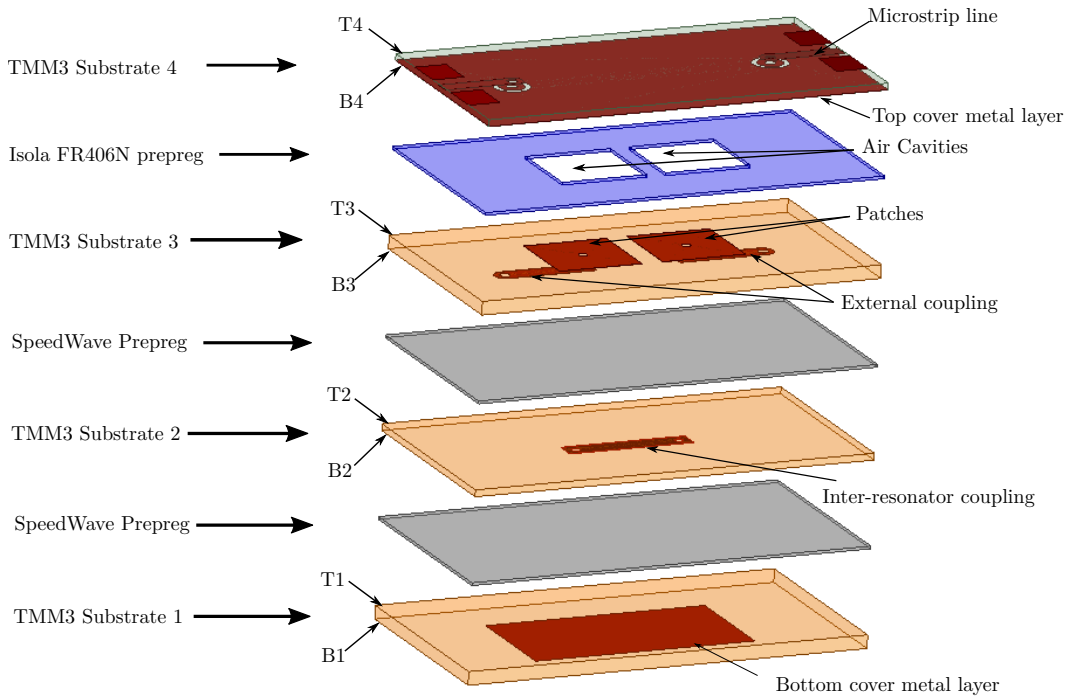


Figure 2.22: A 3-D view of the stack-up layers of the second-order ELCSIW filter. Note that the plated vias that form the walls of the ELCSIW filter are not shown for clarity.

pair of copper pads on both sides that short-circuited to the ground plane through plated vias. The microstrip lines are connected to the external tap striplines through plated vertical transition via. The external coupling tap striplines are shorted to the posts on the bottom side of Substrate 3 (B3) at the height of H_{ex} . The internal coupling tap stripline is placed on the bottom side of Substrate 2 (B2) at the height of H_{in} . It is magnetically coupling the two resonators through the metal connection between their posts [43]. The metal patches are on the top side of Substrate 3 (T3). The following subsections will provide details on how to determine the ELCSIW filter parameters.

2.3.1 Input/Output Feed Lines Design

The 50Ω microstrip lines are designed on the top side of Substrate 4. The characteristic impedance of the transmission line is determined by the height

and the dielectric constant of the substrate and the width of the line and is given by [4]

$$Z_0 = \begin{cases} \frac{60}{\sqrt{\epsilon_e}} \ln \left(\frac{8h}{W_m} + \frac{W_m}{4h} \right) & \text{for } W_m/h \leq 1 \\ \frac{120\pi}{\sqrt{\epsilon_e} [W_m/h + 1.393 + 0.667 \ln(W_m/h + 1.444)]} & \text{for } W_m/h \geq 1, \end{cases} \quad (2.22)$$

where W_m is the microstrip line width and h is the thickness of the microstrip line substrate. ϵ_e is the effective dielectric constant and can be approximated by

$$\epsilon_e = \frac{\epsilon_r + 1}{2} + \frac{\epsilon_r - 1}{2} \frac{1}{\sqrt{1 + 12h/W_m}}. \quad (2.23)$$

Next, the vertical via transition, which causes discontinuity in the signal path, is appropriately designed to reduce its impact on the filter's insertion loss. The vertical transition is shown in Figure 2.23. It can be seen that the signal propagates on the microstrip line and through the bottom of the substrate. Capture pads are formed on the bottom side of Substrate 4 to ensure the continuity of the vertical plated vias, and they are isolated from the ground plane with an anti-pad. The via transitions are then connected to the striplines to couple the energy to the resonators. This configuration creates capacitive and inductive discontinuities on the vertical transition that contributes to the degradation of the signal. These discontinuities can be modeled in lumped element model as shown in Figure 2.24. The configuration of this lumped element model is similar to the low-pass filter circuit model. Thus, the impact of the vertical via transition is comparable to a low pass filter. The capacitance C_1 in the lumped circuit model can be approximated by [51]

$$C_1 \approx \frac{1.41\epsilon_r D_1 t}{D_2 - D_1}, \quad [\text{pF}] \quad (2.24)$$

where D_1 and D_2 are the diameters of the capture and the anti pads, respectively, and t is the thickness of the copper traces. All the dimensions are in inches.

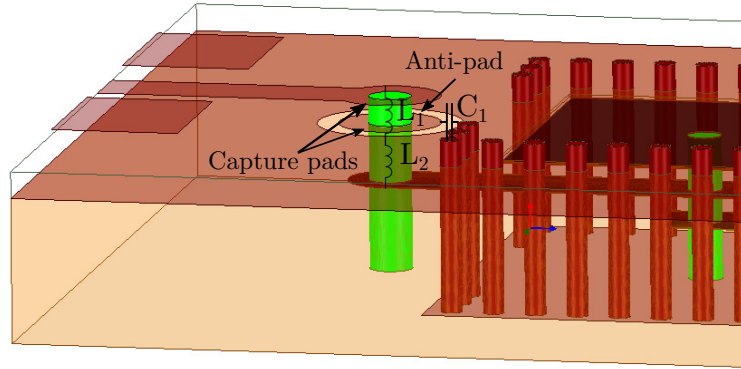


Figure 2.23: A 3D view of the input/output feed line and vertical transition.

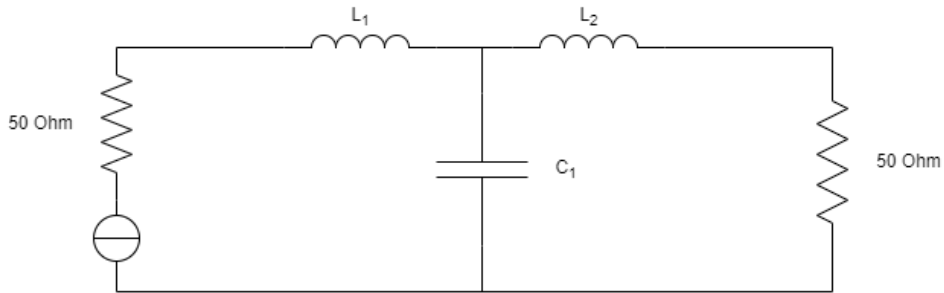


Figure 2.24: Vertical via transition equivalent lumped element circuit model.

The inductance of the via is divided into two parts. The first inductance is between the microstrip line capture pads and the second capture pads on the bottom of Substrate 4. The second inductance is formed between the second capture pad and the stripline tap. Both inductances can be approximated by [51]

$$L_i \approx 5.08h \left[\ln\left(\frac{4h}{r}\right) + 1 \right] \quad [\text{nH}] \quad i = 1, 2, \quad (2.25)$$

where h and r are the vertical vias' lengths and diameters in inches, respectively. It can be seen from (2.24) that minimizing the effect of the capacitance

is obtained by decreasing the capture pad diameter and increasing the anti-pad diameter. Similarly, the inductance can be minimized by reducing the length of the via, which means reducing the substrate thickness. However, the substrate thickness is associated with other parameters that can affect the filter design. Hence, increasing the vertical via diameter can help reduce the inductance. Taking all these into consideration, the capture pads and the anti-pads are made to be 2.4 mm and 3.4 mm, respectively. The vertical vias are selected to be 1 mm. The calculated values of the via capacitance and inductance are shown in Table 2.5.

Table 2.5: Calculated capacitance and inductance of the vertical via transition lumped circuit model elements.

Lumped Element	Value
C_1	0.006987 pF
L_1	0.2454 nH
L_2	0.6668 nH

The circuit model in Figure 2.24 is implemented in AWR Microwave Office Design. The S-parameters of the circuit model are shown in Figure 2.25. The figure shows that at 1.1 GHz, the return loss is greater than 20 dB, and the insertion of only 0.0165 dB, which ensures the minimum effect of the overall filter insertion loss. Also, the vertical via transition's low pass filter cutoff frequency is at 18 GHz.

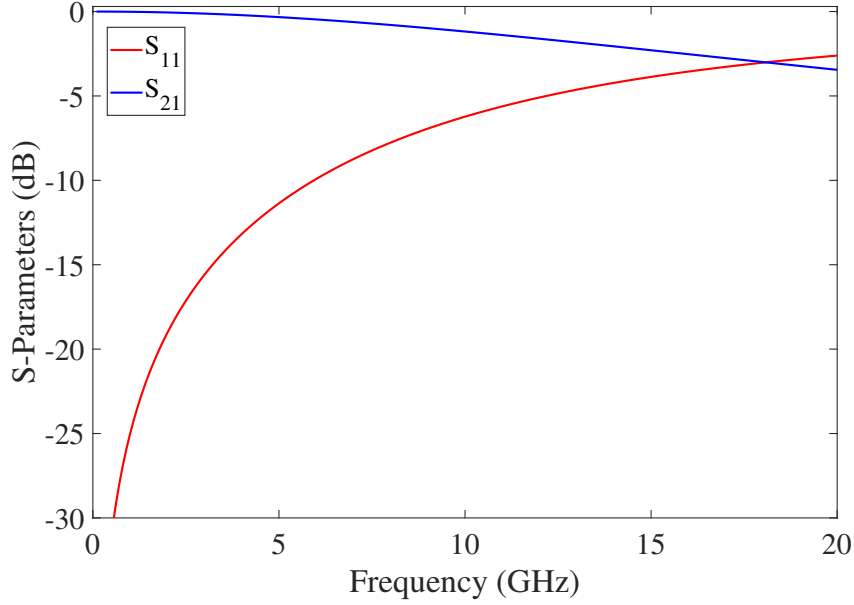


Figure 2.25: S-parameters of the vertical transition via lumped element circuit model.

2.3.2 External Coupling Mechanism

As depicted in Figure 2.2, the ELCSIW cavity has a strong uniform magnetic field around the post. This configuration allows for direct input/output tapped-line coupling to the plated post. The magnetic coupling can be varied by adjusting the height of the tapped line between the vertical via and central posts [43]. The external coupling is represented by the external quality factor, with a strong external coupling resulting in a low external quality factor.

To obtain the physical realization of the calculated Q_{ex} , a single loaded resonator is simulated in the full-wave HFSS solver as a function of the tapped-line height and width. Then, the external quality factor can be extracted by [50]

$$Q_e = \frac{\omega_0 \cdot \tau_{S_{11}}(\omega_0)}{4}, \quad (2.26)$$

where ω_0 denotes the angular resonant frequency and $\tau_{S_{11}}$ denotes the group

delay at the angular resonant frequency. Figure 2.26 shows the extracted external quality factor as a function of the external stripline tap height and width. It can be seen that the stripline height is inversely proportional to the external quality factor. The highest external coupling can be achieved when the stripline is short-circuited to the metal patch. In addition, a fine tuning of the external coupling is achieved by varying the stripline width. This enables optimization flexibility after choosing stack-up substrate thicknesses and allows to finely adjust the Q_{ex} . The desired Q_{ex} is 10.48 and it can be physically realized with a direct stripline tap to the cavity post at $H_{ex} = 2.1$ mm as seen Figure 2.26. The width of the external stripline tap can be fine tuned to achieve the desired coupling.

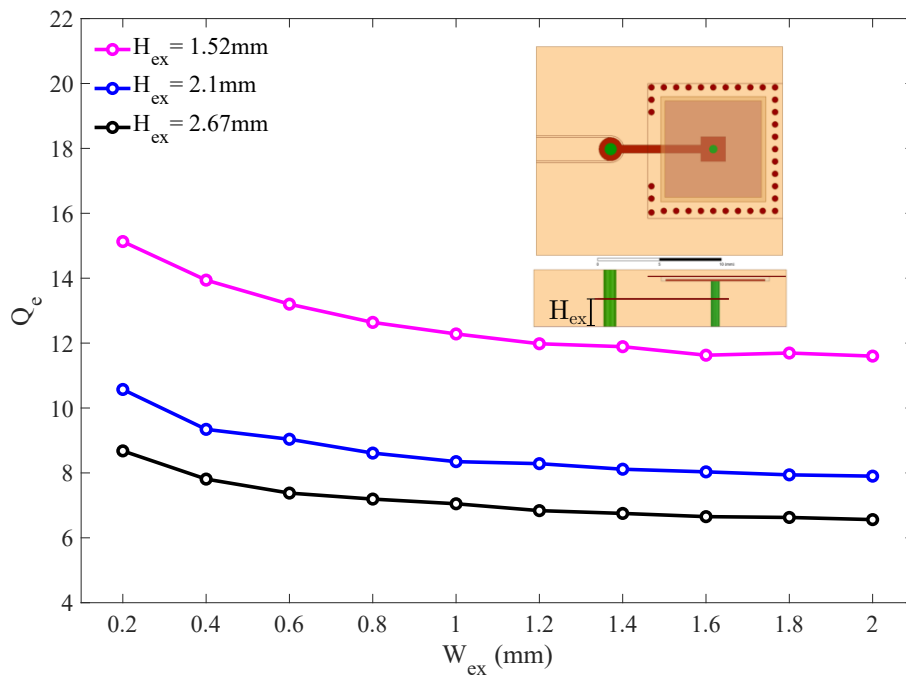


Figure 2.26: External quality factor of an ELCSIW resonator as a function of the external tap width at different tap heights.

2.3.3 Inter-Resonator Coupling Mechanism

Similarly, the inter-resonator coupling is achieved by short-circuiting the two resonators with a stripline between their posts. The height of the stripline

determines the strength of the magnetic coupling, which determines the filter bandwidth [43].

To extract the physical dimensions of the inter-resonator stripline, two coupled resonators are simulated using the eigenmode HFSS solver as a function of the tapped-line height and width. The coupling coefficient, k , can be extracted by [50]

$$k = \frac{f_2 - f_1}{f_2 + f_1}, \quad (2.27)$$

where f_1 and f_2 are the coupled resonators' split resonant-mode frequencies. Figure 2.27 shows that the stripline height is proportional to the inter-resonator coupling. The desired k_{12} is 0.0779 and it can be physically realized with a direct stripline tap between the cavity posts at $H_{in} = 1.3716$ mm as can be extracted from Figure 2.27. The width of the internal stripline tap can be fine tuned to achieve the desired coupling. Nevertheless, the heights of the striplines are limited by the stack-up substrate thickness. Therefore, the selection stack-up substrates must consider the external and inter-resonator coupling parameters.

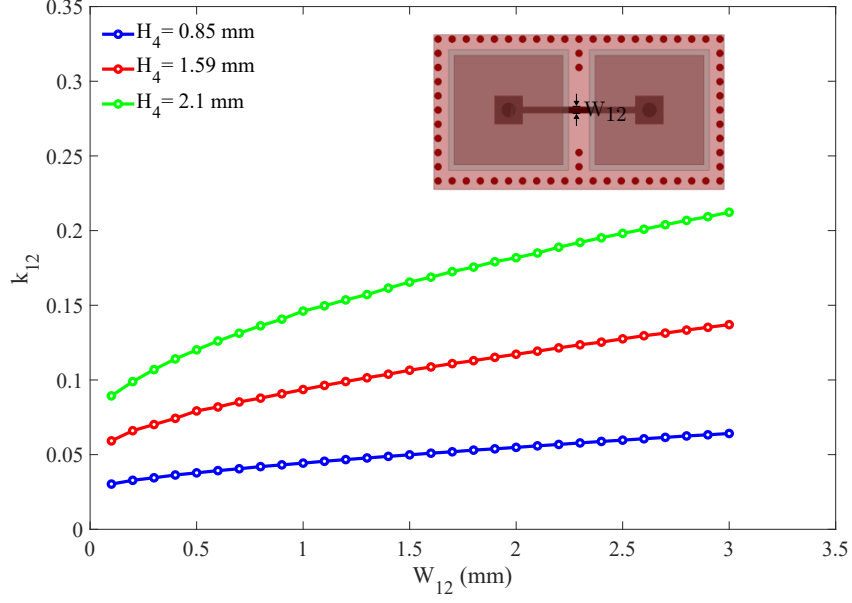


Figure 2.27: Inter-resonator coupling coefficient of two coupled ELCSIW resonators as a function of the internal tap width at different tap heights.

2.3.4 Simulation Results

The designed filter in Figure 2.22 is simulated using the full-wave HFSS solver. The filter parameters' dimensions and thicknesses are listed in Table 2.6. The second-order filter's S-parameters are shown in Figure 2.28. The insertion loss of the simulated filter is 0.26 dB, which includes the input/output feed lines losses and the filter cavities losses. To extract the losses of the filter only, back-to-back input/output feed lines are simulated, and their S-parameters results are shown in Figs. 2.29 and 2.30. The input/output feed lines contribute 0.065 dB of losses into the overall insertion loss. Thus, the insertion loss of the filter is estimated to be 0.195 dB. To extract the unloaded quality factor of the filter, the following equation determines the quality factor based on its insertion loss and bandwidth [52]

$$IL = 4.343 \frac{1}{\Delta Q_{un}} \sum_{i=1}^n g_i \quad (\text{dB}), \quad (2.28)$$

where Δ is the fractional bandwidth, Q_{un} is the unloaded quality factor of the resonators, and g_i are the low-pass filter prototype coefficients which are listed in Table 2.4. The summation of the coefficients is found to be 1.2122. Using (2.28), the extracted unloaded quality factor of the second-order ELCSIW filter is found to be 415 where the unloaded quality factor of the ELCSIW resonator is found to be 480. This reduction in quality factor is due to additional conductor loss introduced by the inter-resonator coupling as current flowing on the stripline tap between the two highly loaded resonators.

Table 2.6: Second-order ELCSIW filter design parameters. All dimensions are in mm.

Design Parameter	Value
Cavity length (W)	10
Patch width (W_r)	8
Post diameter (D)	0.8
Microstrip line width (W_m)	1.2
Microstrip pad (W_p)	2.6
Vertical via transition diameter (D_v)	1
Air cavity to via spacing (S_1)	0.9
Outer via diameter (d)	0.5
Outer via spacing (p)	1
Bottom substrate thickness (H_1)	3.378 (133 mils)
Isola prepreg thickness (H_2)	0.0685 (2.7 mils)
Top substrate thickness (H_3)	0.635 (25 mils)
External tap height (H_{ex})	2.1082 (83 mils)
Inter-resonator tap height (H_{in})	1.3716 (54 mils)
Copper clad thickness (t)	0.0175
SpeedWave prepreg thickness	0.1016 (4 mil)
Inter-resonator stripline width (W_{12})	2
External coupling stripline width (W_{ex})	2

Figure 2.31 shows the filter free spurious stopband. It can be noticed that the stopband is spurious-free up to $7 \times f_r$. This demonstrates one of the many advantages of the ELCSIW filters. In appendix A.1, a fourth-order ELCSIW filter is designed and simulated to demonstrate the scalability of ELCSIW to higher orders.

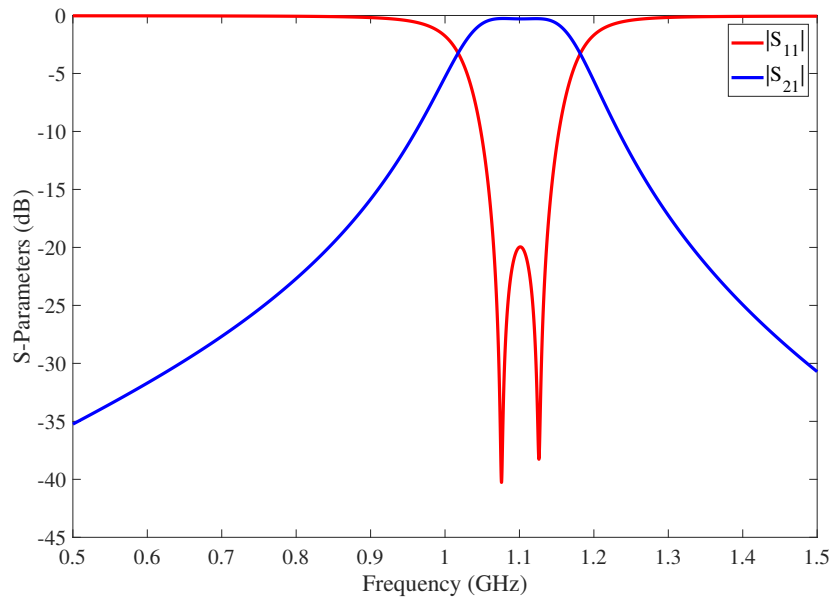


Figure 2.28: Simulated S-parameters of the second-order ELCSIW filter.

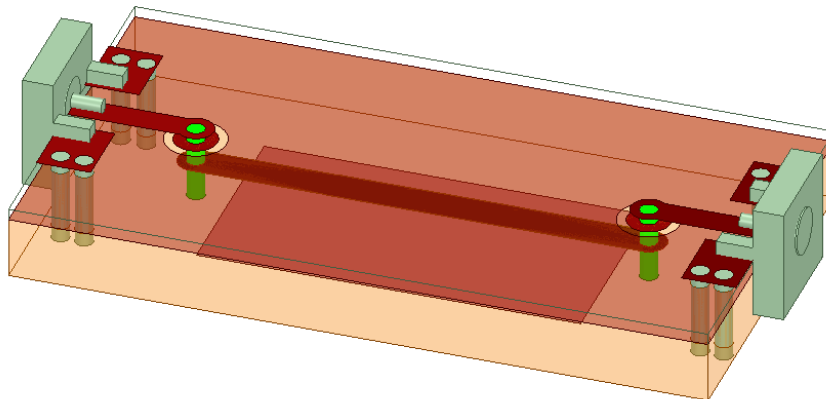


Figure 2.29: A 3D view of the back-to-back input/output feed lines for the second-order ELCSIW filter.

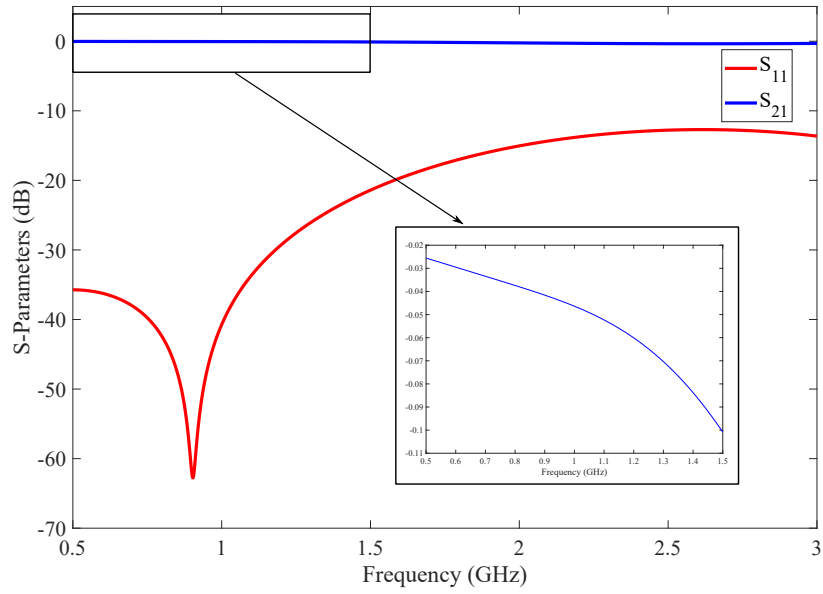


Figure 2.30: Simulated S-parameters of the back-to-back input/output feed lines for the second-order ELCSIW filter.

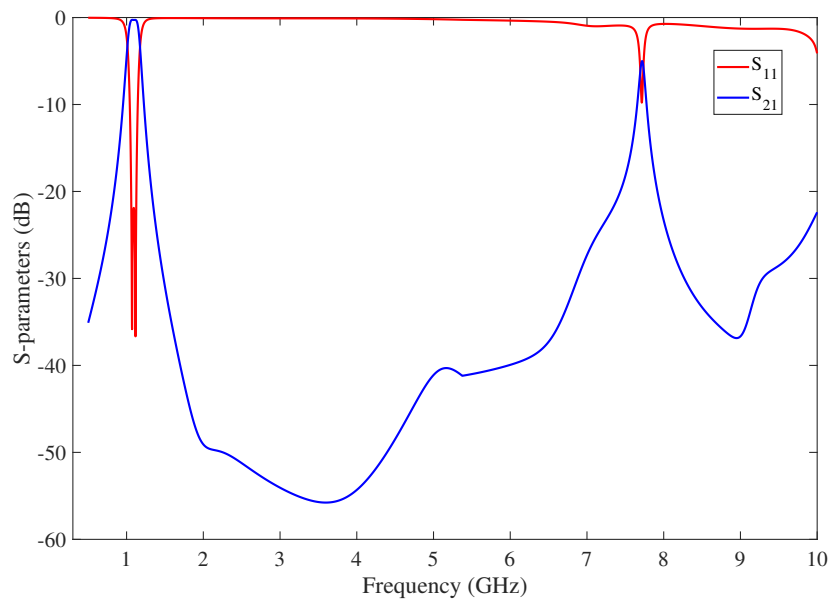


Figure 2.31: Simulated S-parameters of the second-order ELCSIW filter showing the achieved wide spurious free stopband.

2.3.5 Fabrication Procedure

The designed resonator and second-order ELCSIW filter shown in Figure 2.15 and 2.21, respectively, are fabricated using a standard PCB process. The dimensions and the substrate thickness of the stack-up layers for the designed resonator and filters are presented in Table. 2.3 and 2.6, respectively. The fabrication steps are designed to meet the capabilities of the ARRC fabrication lab. A summary of the fabrication guidelines as follows:

1. Generate all Gerber and drill files needed for each layer.
2. Stack up all the dielectric substrates and drill the alignment and fiducial vias.
3. Remove the copper from Substrate 1 top and Substrate 2 top layers using the photolithography process and hydrochloric acid etchant.
4. Pattern the Substrate 1 bottom, Substrate 2 bottom, and Substrate 2 top copper using a photolithography process. Then, the unwanted copper is removed through an etching process.
5. Clean all layers with a micro etching bath and prepare them for the lamination process.
6. Stack up and laminate Substrates 1, 2, and 3 with the Speedwave prepreg in between using lamination guidelines in [53].
7. Drill the posts in the stacked layers and then clean them with a micro etchant bath to prepare for the plating process. additional details on copper plating are included in Appendix A.2.
8. Perform electroless copper plating on the stacked layers to deposit a copper seed layer for the post walls.

9. Cover the top side of the stacked layer with Kapton tape to preserve the thickness of the copper patch on Substrate 3 top during the electroplating process.
10. Perform pulsed electroplating on the stacked layer with a slow deposition rate to ensure uniform copper plating.
11. Pattern the Substrate 3 top copper layer to form the metal patches using the photolithography process, and the remaining copper is etched away.
12. Pattern the Isola prepreg in which the air cavities are formed and prepare it for the lamination process.
13. Pattern the Substrate 4 bottom copper layer using LPKF U4 ProtoLaser.
14. Stack up and laminate the subassembly and Substrate 4.
15. Drill cage vias and SMA pads vias using LPKF S104 ProtoMat milling machine.
16. Perform electroless plating and electroplating processes on the stacked boards to plate the drilled vias.
17. Mill the top side of Substrate 4 and the bottom side of Substrate 1 using the LPKF U4 ProtoLaser.
18. Cut filter sample out of the board.
19. Solder two 50 Ω SMA connectors to the input/output microstrip lines.

The resonator and filter are fabricated using the capabilities of the ARRC. Multiple duplicate prototypes for the designed resonator and the filter are implemented on one board through the same fabrication process.

2.3.6 Measurements and Discussion

The designed ELCSIW resonator shown in Figure 2.15 is fabricated following the procedure outlined in section 2.3.5. The photograph of the fabricated resonator is shown in Figure 2.32. An Agilent N5225A network analyzer is used to conduct the measurements and a calibration is performed on the network analyzer ports using an N4691-60006 electronic calibration kit to shift the reference plane to the end of the coaxial cables. The resonator transmission coefficient is measured and compared with the simulation results in Figure 2.33. The figure shows a 106 MHz frequency shift from the simulation results. This can be attributed to the manual fabrication process steps and the frequency sensitivity to the thickness of substrate H_2 as shown in Figure 2.7. During the fabrication process, the metallic patches had to be polished to remove any copper bumps at the edges of the plated posts. As this was performed by hand, the copper thickness of the metallic patch (t) could have become less than $17.5 \mu\text{m}$ and resulted in a larger air gap and thus a higher resonant frequency. Also, the Isola prepreg used to construct the air gap has a manufacturer tolerance of $\pm 7 \mu\text{m}$, which can contribute to the frequency shift. The unloaded quality factor of the fabricated ELCSIW resonator is extracted using (2.19) and found to be 312. In the simulation, the copper conductivity is assumed to be $5.8 \times 10^7 \text{ S/m}$ and has no surface roughness, resulting in a 480 unload quality factor. However, the electroplating process generates a copper surface with finite roughness, which causes an additional conductor loss. The copper roughness of the acid copper electroplating process could exceed $10 \mu\text{m}$ as reported in [49]. From Figure 2.14, the estimated copper surface roughness of the plated surfaces based on the measured unloaded quality factor is found to be $10 \mu\text{m}$.

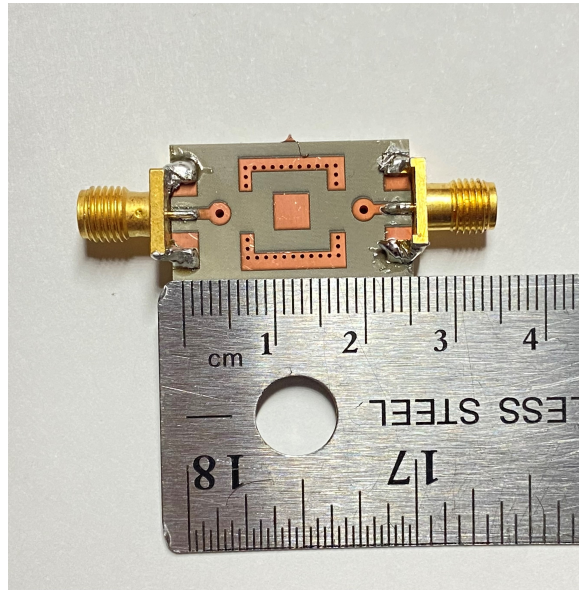


Figure 2.32: Photograph of the fabricated ELCSIW resonator.

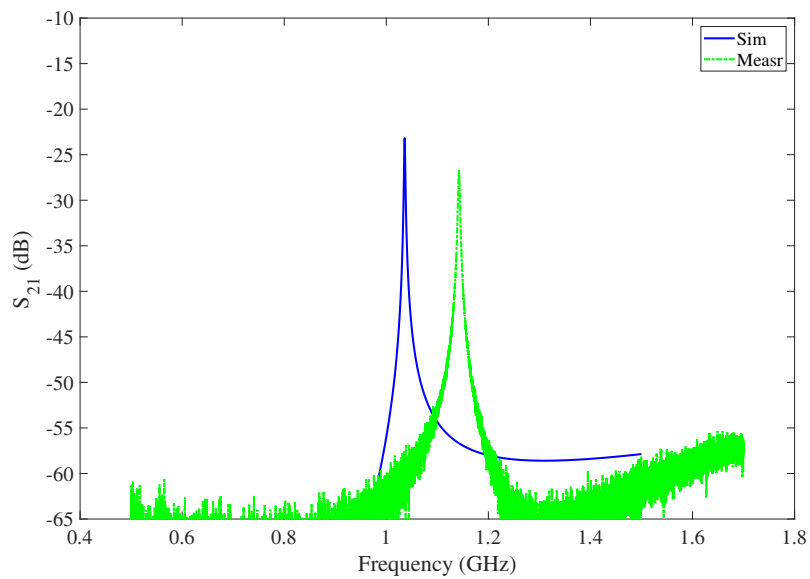


Figure 2.33: Comparison between the simulated and measured S_{21} of the proposed ELCSIW resonator.

The second-order ELCSIW bandpass filter shown in Figure 2.21 is fabricated following the procedure outlined in section 2.3.5. The photograph of the fabricated filter is shown in Figure 2.34. The measurements of the filters are performed using an Agilent N5225A network analyzer. A calibration is performed

on the network analyzer ports using an N4691-60006 electronic calibration kit to shift the reference plane to the end of the coaxial cables. The simulated and measured S-parameters of the filter are presented in Figure 2.35. Since the filter and the resonator are built on the same board, the filter exhibits similar resonant frequency discrepancies due to fabrication tolerances. The measured center frequency of the filter is 1.156 GHz, which is 5.1 % higher than the desired resonant frequency. The measured insertion loss of the filter is less than 0.54 dB, and the measured return loss is greater than 15 dB. The simulated insertion loss is found to be 0.26 dB. There is a 0.28 dB additional insertion loss in the measured results, which can be attributed to the additional conductor loss caused by the copper surface roughness produced by the in-house electroplating process. In Figure 2.36, the filter exhibits a spurious free band of up to 7.8 GHz with a rejection of at least 20 dB. This indicates the spurious-free band is larger than $7 \times f_r$.

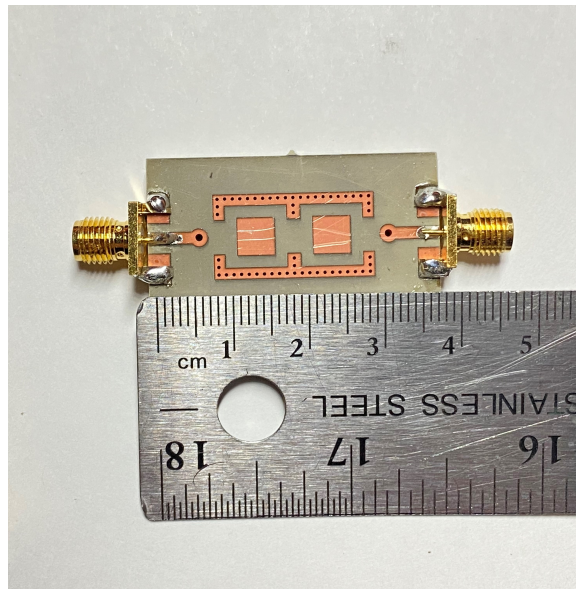


Figure 2.34: Photograph of the fabricated second-order ELCSIW filter.

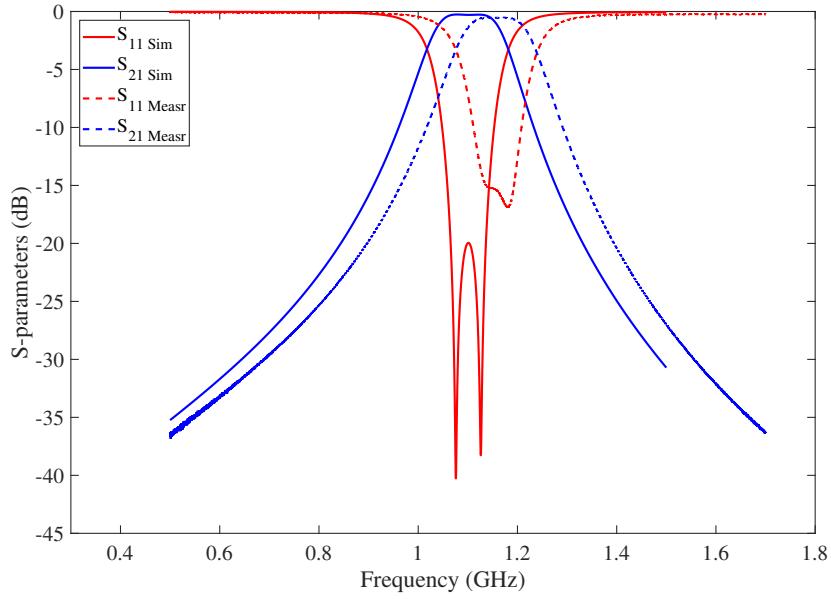


Figure 2.35: Comparison between the simulated and measured wideband response of the second-order ELCSIW filter.

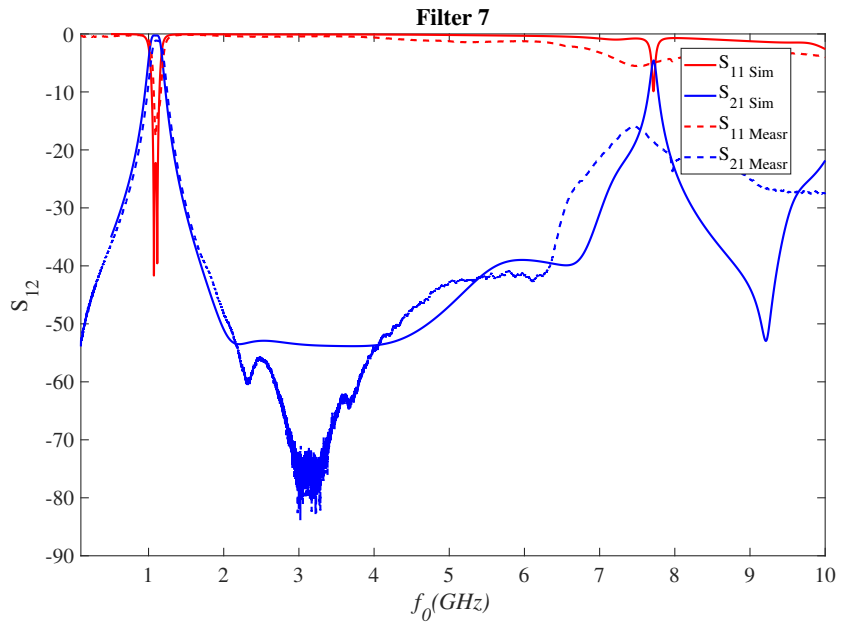


Figure 2.36: Comparison between the simulated and measured results of the second-order ELCSIW filter with a wide frequency sweep.

To verify that the variation of the H_2 has affected the resonant frequency, clamps are used to tune the filter by applying a force on the top cover substrate

to reduce the thickness of the air gap. The setup of this post-fabrication tuning is shown in Figure 2.37. The filter's resonators are tuned separately since the fabrication tolerance and errors might impact each resonator differently. The S-parameters of the measured tuned filter are compared to the simulated results and presented in Figure 2.38. The measured insertion loss is less than 0.47 dB, and the measured return loss is greater than 20 dB. The fractional bandwidth of the measured filter is 5.56 %, which is 0.7 % smaller than the fractional bandwidth predicted by the simulation. This decrease in fractional bandwidth is caused by the mistuned frequency of one or two of the filter's resonators.

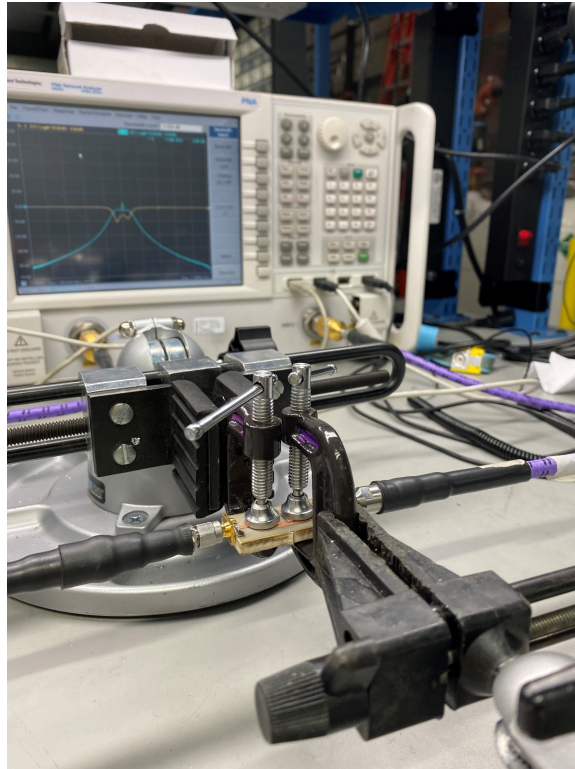


Figure 2.37: Post-fabrication tuning setup for the second-order ELCSIW filter.

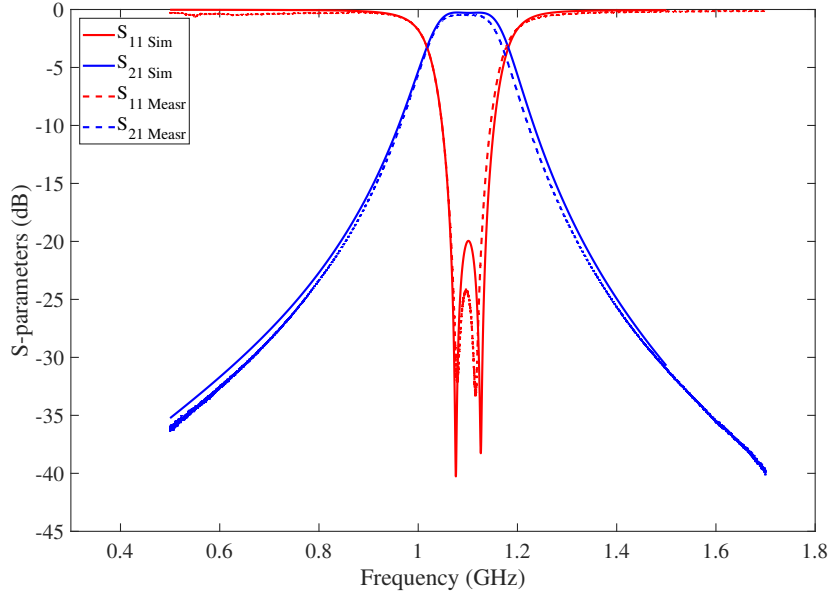


Figure 2.38: Comparison between the simulated and measured results of the designed second-order ELCSIW filter after the post-tuning.

As can be seen from the results of the measurements, the resonant frequency is affected by the tolerances and errors encountered during the fabrication. These effects result in a frequency shift either above or below the desired frequency. Hence, post-fabrication frequency tuning is necessary to account for fabrication defects and material tolerances. The next chapter proposes a novel post-fabrication frequency tuning method in ELCSIW technology to compensate for the fabrication tolerances.

In conclusion, the proposed ELCSIW filter achieves a miniaturization factor of 99 % while providing a wide spurious free band with a quality factor greater than 480. The filter performance in terms of miniaturization factor, unloaded quality factor, and spurious-free band are summarized and compared to related works in the literature and presented in Table 2.7. In [54], the authors developed a miniaturized SIW cavity by folding the cavity at its center plane four times. This allows achieving 89 % miniaturization factor with low Q_u . In [37], a second-order thirty-second mode SIW filter is proposed by cutting the SIW resonators

on their imaginary magnetic walls to obtain size reduction. This technique exhibits excellent advantages in miniaturizing SIW structures. The drawback of this technique is that the unloaded quality factor is low due to increased radiation loss at the open edges. In [38], a novel folded ridged quarter-mode SIW is characterized and implemented to design a miniaturized bandpass filter. By folding the fundamental mode of a ridged quarter-mode SIW around the ridge, miniaturization of 98 % was achieved and demonstrated by a second-order filter with a quality factor of 128. This high miniaturization factor comes with the expense of a low-quality factor. In [43] and [44], two bandpass filters are developed using the embedded coaxial SIW structure, achieving a high miniaturization factor of 96 % with an unloaded quality factor of 165 and 325, respectively. The proposed ELCSIW filter in this work shows superior filter characteristics compared to the reported work. Among the reported SIW miniaturization techniques, the ELCSIW technology has the highest reported miniaturization factor, and the highest reported unloaded quality factor. In addition, the filter exhibits a large spurious-free band of seven times the resonant frequency, which matches the best spurious-free range amongst miniaturized filters in the literature. These advantages of the ELCSIW technology demonstrate its capacity to meet the stringent requirements of compact modern communications systems.

Table 2.7: Comparison between the related works in the literature and the proposed ELCSIW filter.

Ref	Miniaturization Technique	f_r (GHz)	Miniaturization factor	Area (λ_g^2)	Q_u	Order	FBW	IL (dB)	Spurious-free band
[54]	Quadri-folded SIW	3.2	89 %	$0.24\lambda_g \times 0.24\lambda_g$	120*	4	9.6 %	1.6	NA
[37]	Thirty-second Mode SIW	2.45	96.8 %	$0.2\lambda_g \times 0.24\lambda_g$	65*	2	36.7 %	0.25	$2.94 \times f_r$
[38]	Folded-ridge QMSIW	1.59	98 %	$0.12\lambda_g \times 0.24\lambda_g$	92	2	5.53 %	2.72	$3.6 \times f_r$
[43]	Embedded coaxial SIW	1.5	96.8	$0.426\lambda_g \times 0.126\lambda_g$	165	3	10 %	1.2	$7 \times f_r$
[44]	Embedded coaxial SIW	1	96.4 %	$0.237\lambda_g \times 0.237\lambda_g$	325	4	3.8 %	1.8	$3 \times f_r$
This Work	Embedded loaded coaxial SIW	1.1	99 %	$0.07 \lambda_g \times 0.26\lambda_g$	480	2	6.3 %	0.47	$7 \times f_r$

*Extracted using Cohn formula [55].

2.4 Second-order Embedded Loaded Coaxial SIW Filter with Mixed Electric and Magnetic Coupling

Designing filters with transmission zeros is desirable to improve the stopband rejection. The coupling mechanism and filter topology are utilized to achieve transmission zeros in the stopband. Source-load coupling and cross-coupling are common mechanisms used to generate transmission zeros [56–58]. These mechanisms achieve the desired requirements with the cost of degrading isolation between input and output ports since they often require folded cross-coupled topology. Low-order filters can achieve the stopband requirements that are typically met by high-order filters by using the generated transmission zeros. This adds an additional advantage to low-order filters, which generally are smaller in size and have a lower insertion in comparison to high-order filters. In [59], a method of generating transmission zeros is developed by mixing electric and magnetic coupling. An inline filter topology and configuration that allows for two controllable separate electric and magnetic coupling is characterized to generate transmission zeros. One transmission zero can be generated in an inline two-pole filter by controlling the intensity of the electric and magnetic coupling. The location of the transmission zero is determined by which coupling is dominant. This mixed-coupling mechanism can be used in second-order topology to obtain a compact filter with excellent stopband rejection.

One of the benefits of the ELCSIW filter is its capacity to generate two electric and magnetic coupling paths with minimal additional fabrication cost. The proposed technology's unique structure allows two adjacent resonators to electrically couple by extending striplines from the resonator patches and form interdigital capacitor, as shown in Figure 2.39. In conjunction with direct tap magnetic coupling, this extra coupling mechanism provides mixed-coupling that can produce a transmission zero on either side of the passband. The intensity of

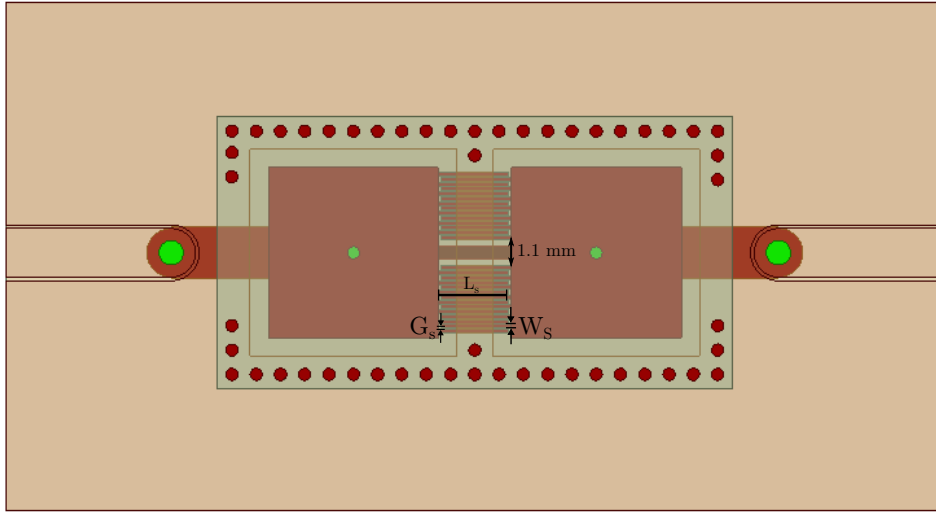


Figure 2.39: Design illustration of the second-order ELCSIW filter with mixed magnetic and electric coupling mechanisms.

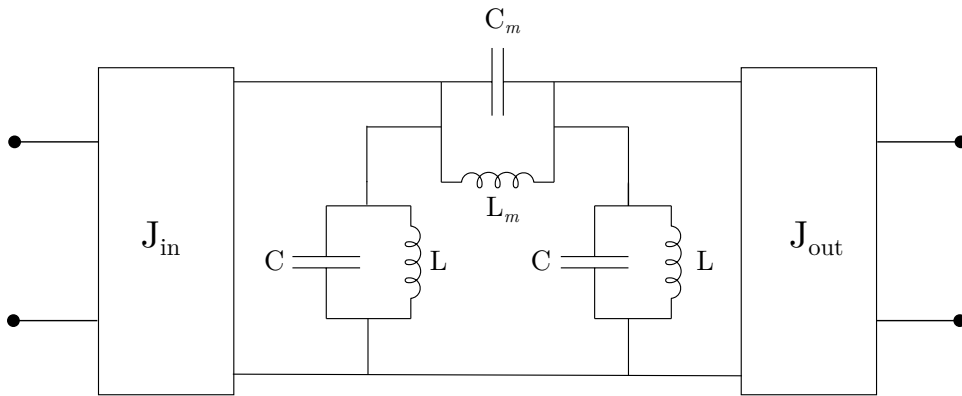


Figure 2.40: Equivalent lumped element circuit model of the mixed-coupling second-order ELCSIW filter.

electric coupling demonstrated in Figure 2.39 is adjusted by the length and the width of the striplines, and the spacing between them. To illustrate the effect of the mixed-coupling mechanism, an equivalent lumped element circuit model of the second-order mixed-coupling ELCSIW filter is presented in Figure 2.40. L and C denote each resonator's total inductance and capacitance, respectively. L_m represents the direct tap inductance from the flowing current between the resonator posts. C_m represents the capacitance of the interdigital capacitor between the resonator patches.

The inter-resonator coupling of a mixed-coupling filter can be extracted by [60]

$$k = \frac{\omega_{odd}^2 - \omega_{even}^2}{\omega_{odd}^2 + \omega_{even}^2} = \frac{M_c - E_c}{1 - M_c E_c}, \quad (2.29)$$

where

$$\omega_{even} = (LC)^{-1/2} \quad \omega_{odd} = \left[\frac{LL_m(C + 2C_m)}{2L + L_m} \right]^{-1/2} \quad (2.30)$$

are the even and odd frequencies modes, respectively. The electric and magnetic coupling can be determined by the

$$E_c = \frac{C_m}{C + C_m}, \quad M_c = \frac{L}{L + L_m}. \quad (2.31)$$

The resonant frequency of the individual resonator is determined by

$$\omega_r = \left[\frac{LL_m(C + C_m)}{L + L_m} \right]^{-1/2}. \quad (2.32)$$

The frequency at which the transmission zero is generated by the mix coupling can be represented by

$$\omega_m = (L_m C_m)^{-1/2}. \quad (2.33)$$

Figure 2.41 shows the extracted inter-resonator coefficients of two weakly mixed-coupling ELCSIW cavity resonators. The plot illustrates the coupling coefficient (k) as a function of stripline length (L_s) at different heights of the direct tap coupling. In an interdigital capacitor, the longer the strip length, the higher the capacitance and the stronger the electric coupling between the strips. For direct tap coupling, the higher the position of the tap (H_{in}), the smaller the inductance (L_m), and the stronger the magnetic coupling. As (2.29) suggests, the coupling coefficient becomes positive when the magnetic coupling M_c is larger

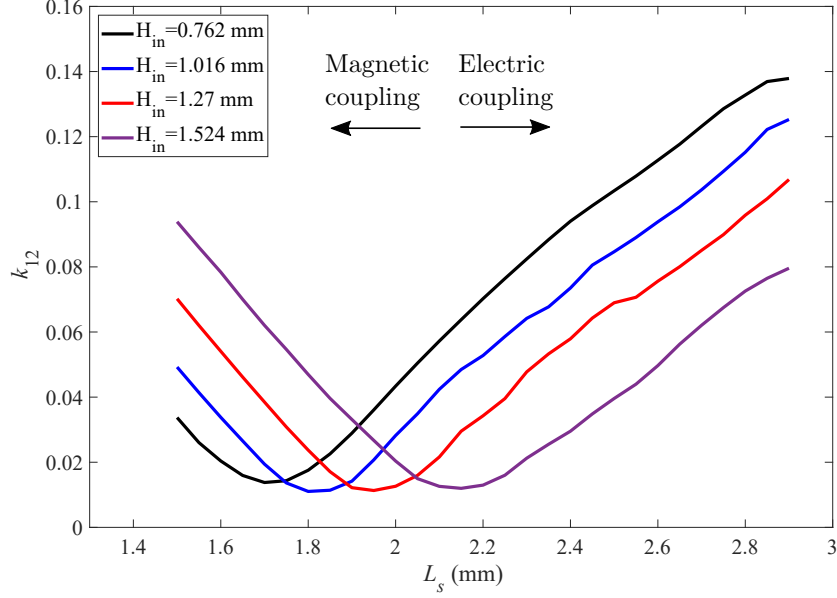


Figure 2.41: Inter-resonator coupling coefficient (k_{21}) as a function of the electric coupling strip length at different heights of the inter-resonator tap.

than electric coupling E_c and vice versa. Thus, it can be noticed that the increase of L_s leads to an overall electric dominant coupling, which can be countered by placing the direct tap at a higher position. Two examples of mixed-coupling second-order ELCSIW filters, namely filter A and filter B, are designed and simulated to demonstrate the benefits of mixed-coupling. Figure 2.42 shows the S-parameters of filter A where the magnetic coupling is dominant. This generates a transmission zero in the upper stopband of the filter.

In Figure 2.43, the plot shows the location of the transmission zero in the lower stopband of the filter when the inter-resonator coupling is dominant by the electric coupling. The parameters of filter A and filter B are listed in Table 2.8. In Figure 2.44, transmission zeros locations as function of the strip length (L_s) are illustrated. When the length of the interdigital strip is increased, the transmission zero shifts from the upper side of the filter passband to the lower side. This increase causes the mixed-coupling to change from magnetically dominant to electrically dominant.

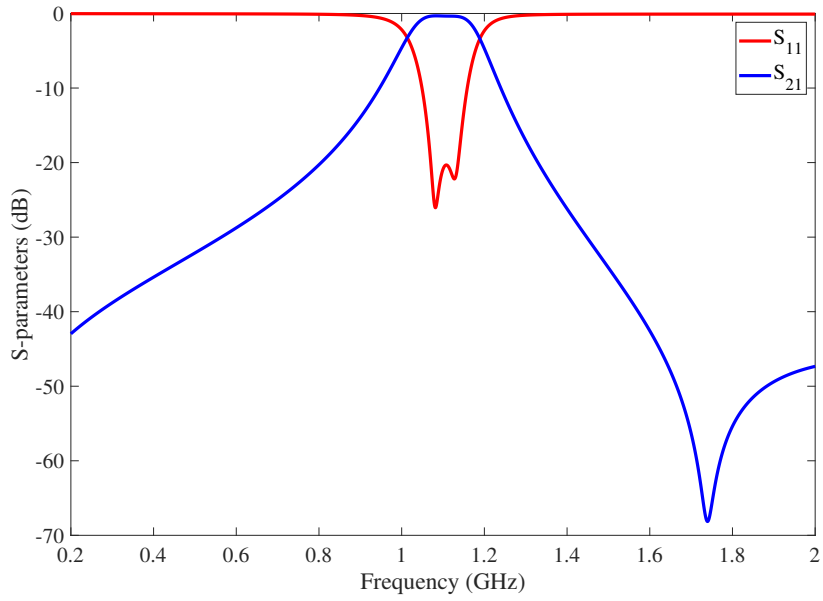


Figure 2.42: Second-order embedded loaded mixed-coupling coaxial SIW filter with dominant magnetic coupling.

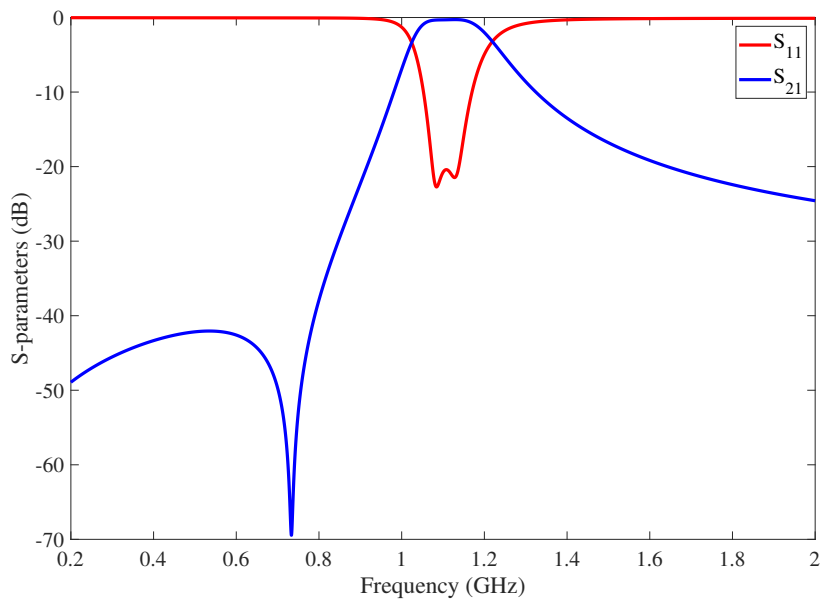


Figure 2.43: Second-order embedded loaded mixed-coupling coaxial SIW filter with dominant electric coupling.

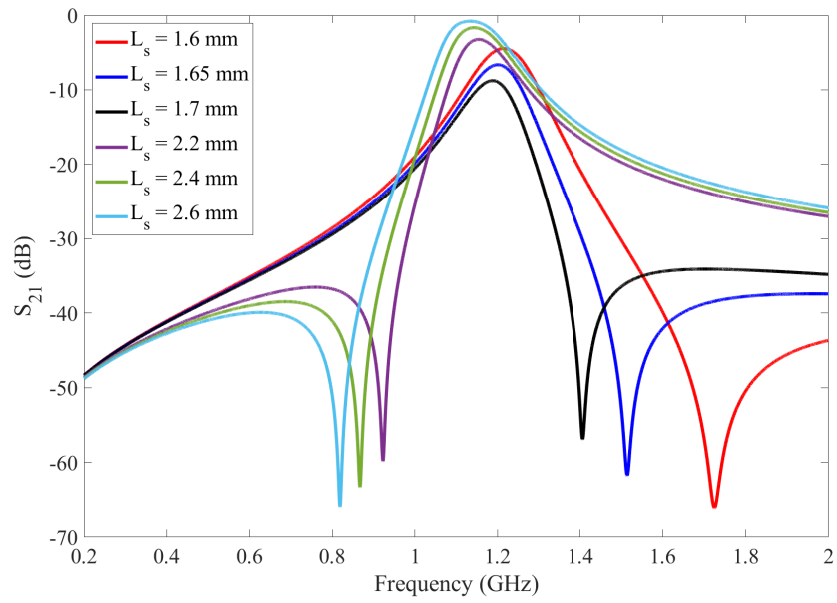


Figure 2.44: Simulated second-order mixed-coupling filter B showing the transmission zero locations as a function of the strip length (L_s).

Table 2.8: Mixed-coupling second-order filters design parameters. All dimensions are in mm.

Design Parameter	Filter A	Filter B
	value	value
Cavity length (W)	10	10
Patch width (W_r)	7	7
Post diameter (D)	0.8	1.3
Coplanar waveguide width (W_c)	2.6	2.6
Microstrip line width (W_m)	1.2	1.2
Microstrip pad (W_p)	2.6	2.6
Vertical via transition diameter (D_v)	1	1
Air cavity to via spacing (S_1)	0.9	0.9
Outer via diameter (d)	0.5	0.5
Outer via spacing (p)	1	1
Bottom substrate thickness (H_1)	3.378 (133 mils)	3.378 (133 mils)
Isola prepreg thickness (H_2)	0.0685 (2.7 mils)	0.0685 (2.7 mils)
Top substrate thickness (H_3)	0.635 (25 mils)	0.635 (25 mils)
External tap height (H_{ex})	2.3622 (93 mils)	1.524 (60 mils)
Inter-resonator tap height (H_{in})	1.524 (60 mils)	1.27 (50 mils)
Copper clad thickness (t)	0.0175	0.0175
Inter-resonator stripline width (W_{12})	1.75	1
External coupling stripline width (W_{ex})	1.8	2
Strip length (L_s)	1.55	2.95
Strip width (W_s)	0.15	0.15
Strip gap (G_s)	0.05	0.5

2.5 Power-Handling Capabilities

Power-handling capability is a key factor in designing RF filters. It determined the maximum power that a filter can handle at any point in time without performance failure. Dielectric breakdown, gas ionization breakdown, and thermal-related high-power breakdown are a few examples of failure causes [61]. In an ELCSIW cavity resonator, the electric fields are concentrated in the air gap between the patch and the top cover, as shown in Figure 2.2. Therefore, the focus of this power-handling capability is going to be on the air ionization breakdown in an ELCSIW cavity resonator at room temperature and at 1 atmosphere pressure. The ionization effect results from highly energetic electrons colliding and

releasing new electrons. This effect creates a conducting path enabling a sharp increase in the current and causing resonator breakdown. The ELCSIW filter's power-handling capability analysis can be performed using a full-wave solver. Knowing the stored energy in each resonator and the peak electric field in the resonator, the maximum power-handling capacity can be determined by [62]

$$P_{max} = \left(\frac{E_{air\ breakdown}}{E_{max-norm}} \right)^2 \times \frac{1}{W_{stored-max}}, \quad (2.34)$$

where $E_{air\ breakdown}$ is the air ionization breakdown, $E_{max-norm}$ is the maximum electric field in the cavity normalized to 1 nJ of stored energy, and $W_{stored-max}$ is the stored energy in the resonator. In [63], high-power RF gas discharge in a highly loaded evanescent-mode cavity is investigated. The electric field in the evanescent-mode cavity is concentrated between the loading post and the top wall. The study found that increasing input power leads to gas ionization and discharge inside the cavity resonator. The air ionization breakdown is found to be 7.9 MV/m in air gaps of tens of micrometers. The following section presents a step-by-step procedure for predicting the ELCSIW filter's power-handling capability.

- First, the second-order filter is modeled using the full-wave HFSS solver. All structure details must be included to achieve a high-accuracy prediction. In addition, the designed filter must avoid a load mismatch between the input/output port and the filter. The load mismatch raises the stored energy by a factor of $(1-|\Gamma|)^2$ where Γ is the reflection coefficient [61]. Moreover, the sharp edges and corners inside the resonator can cause a significant increase in the electric fields and consequently lower power capability [64]. Thus, any sharp features in the design should be eliminated if possible.

- Next, the stored energy (W_{stored}) in each resonator is extracted. The stored energy can be expressed as

$$W_{stored} = \frac{1}{2}\epsilon \int |E|^2 dv, \quad (2.35)$$

where ϵ is the free space permittivity and E is the electric field in the examined volume. Full-wave HFSS solver simulation is performed for the filter shown in Figure 2.21. Since the E-field is concentrated in the air gap between the patch and the top cover, it's important to assign fine meshing in the air volume for accurate stored energy results. After the simulation is performed, the stored energy can be calculated using the post-processing field calculator. The extracted stored energy for the second-order ELCSIW filter at different frequency locations in passband is presented in Figure 2.45. In Figure 2.46, the locations of the extracted stored energy are plotted on the filter passband S-parameters. It can be observed that Resonator 1 has greater stored energy than Resonator 2. Also, the maximum stored energy is occurred at the edge of the passband, as shown in Figure 2.45 and Figure 2.46. The maximum stored energy is found to be 2.223 nJ at 1.17 GHz.

- The next step is to extract the normalized electric field in the resonator. First, the stored energy obtained in the previous step is normalized by

$$W_{stored-norm} = \frac{1 \text{ nJ}}{W_{stored}}. \quad (2.36)$$

The $W_{stored-norm}$ value is then inserted in the excitation source magnitude in the full-wave HFSS simulation. The electric field can be plotted where the maximum field intensity is using the 'ComplexMag_E' function. The

electric field is plotted on a plane at the center of the resonator as shown in Figure 2.47. The normalized electric field is observed at the edge of the post via. This increase in the maximum electric field at the edge of the posts is a result of the current crowding at the via edge. The $E_{max-norm}$ is found to be 0.498 MV/m. To eliminate the sharp feature at of the post, solid filled-via can be used to reduce the maximum field at the post and as results increase the power-handling capability. The electric field is plotted on a plane at the center of the resonator with solid filled-via, as shown in Figure 2.48. The maximum electric field is observed at the patch edge, and its found to be 0.452 MV/m.

Eventually, the power-handling capability of the filter with through-metalized posts can be determined using (2.34) to be

$$\left(\frac{7.9}{0.498} \right) \times \frac{1}{2.223} = 113 \text{ Watts} = 50.53 \text{ dBm}$$

and for the case of a solid post via, the maximum power capability is

$$\left(\frac{7.9}{0.452} \right) \times \frac{1}{2.223} = 137 \text{ Watts} = 51.3 \text{ dBm}.$$

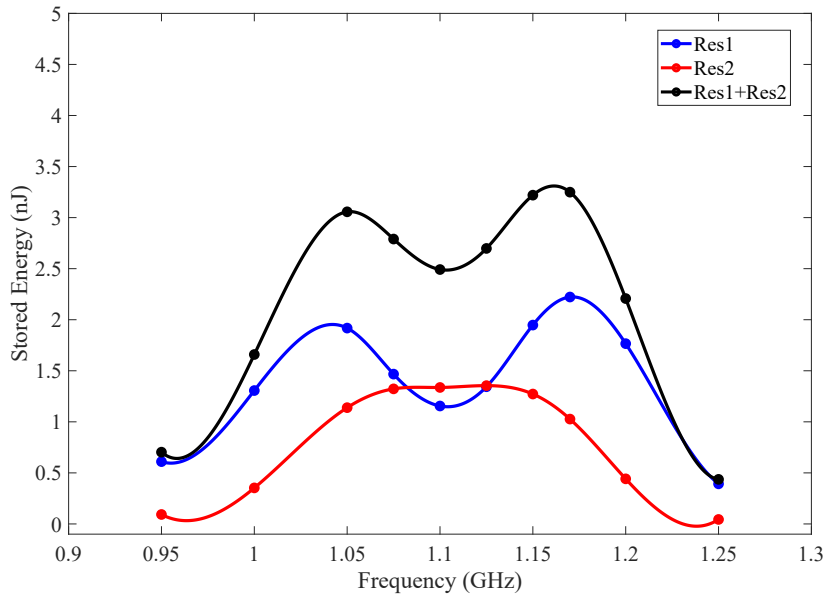


Figure 2.45: Simulated stored energy of the resonators of the second-order ELCSIW filter.

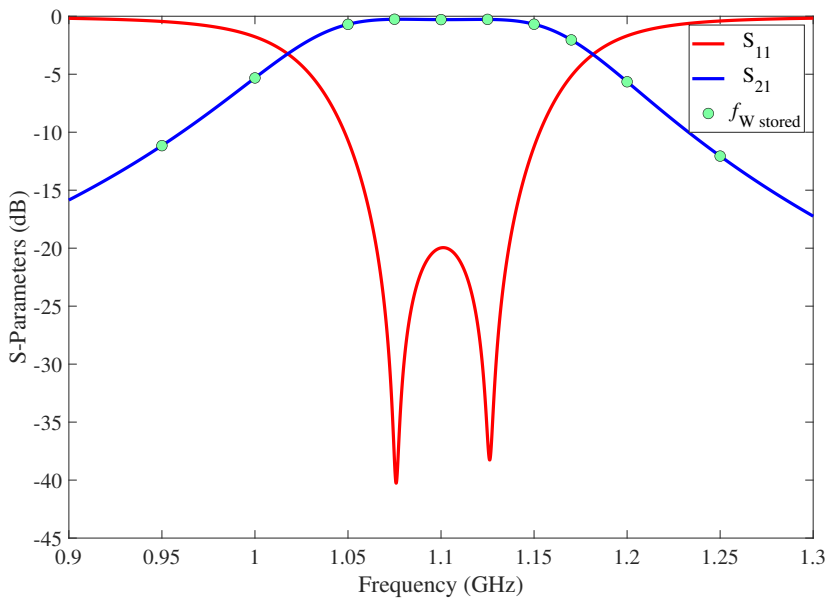


Figure 2.46: Frequency locations of the extracted stored energy of the second-order ELCSIW filter.

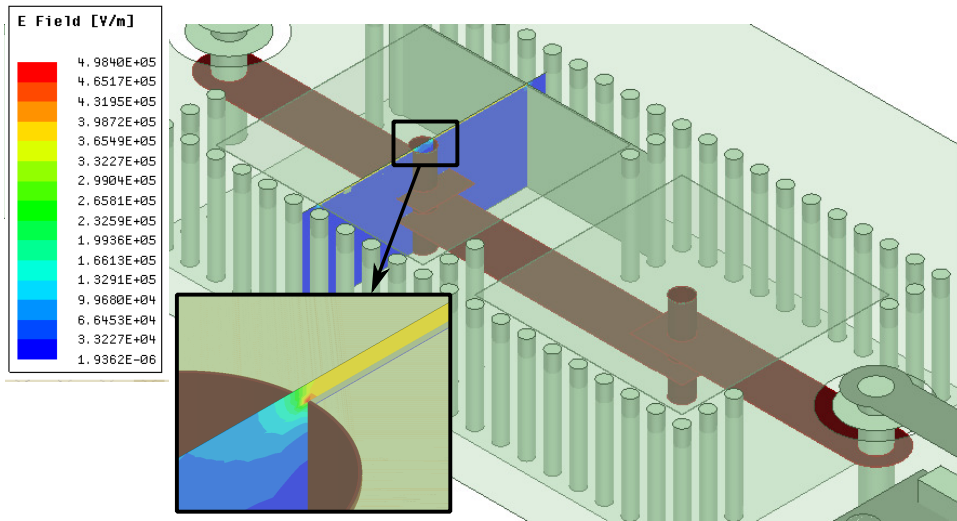


Figure 2.47: Electric-field distribution inside the second-order ELCSIW filter cavity with the posts modeled as through-plated vias. The inset figure shows a closer view of the electric-field at the edge of the post.

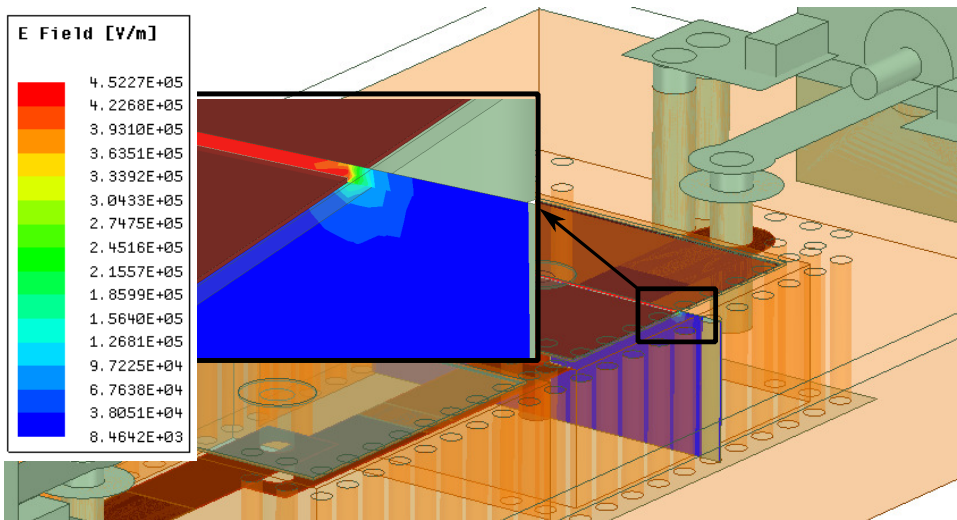


Figure 2.48: Electric-field distribution inside the second-order ELCSIW filter cavity with the posts modeled as copper-filled vias. The inset figure shows a closer view of the electric-field at the edge of the patch

In conclusion, the proposed ELCSIW filter is a significant advancement in the SIW filter technology and outperforms previous work in this area. This technology has been shown to have the highest miniaturization factor and the highest unloaded quality factor among the various miniaturization techniques reported for SIW filters. The ELCSIW filter also has a wide spurious-free band, seven times wider than its resonant frequency, making it an excellent choice for modern communications and radar systems that require compact and high-performance filters. These advantages make the ELCSIW filter a standout option to meet the demanding requirements of compact modern communications and radar systems.

Chapter 3

Post-Fabrication Frequency Tuning of Embedded Loaded Coaxial Substrate Integrated Waveguide Filters

Designing and manufacturing microwave filters involves multiple stages, each requiring a high degree of precision and attention to detail. The use of commercially available software has made designing and simulating a microwave filter's response much easier and more accurate. Despite the advanced software and the design process, the measurement response of a microwave filter after fabrication can still differ from the simulation results. There are various reasons for this discrepancy, including fabrication process tolerances and variations in the physical properties of the materials used. To account for these differences, post-fabrication tuning is an important step in the manufacturing process. This step involves measuring the actual response of the filter and making any necessary adjustments to bring it closer to the desired response. The tuning process is done using specialized test equipment and can involve adjusting the physical dimensions of the filter, adjusting the orientation of the components, and making other changes to the design.

The proposed embedded loaded coaxial substrate integrated waveguide filter can be accurately designed and tuned using the full-wave HFSS solver. However, the tolerances and variations in the dielectric permittivity and thicknesses of the prepreg and the dielectric substrates will ultimately determine the final filter

performance. These variations can introduce perturbation in the filter electromagnetic response, which can shift the center frequency. Figure 3.1 displays the S_{21} measurements of nine filters manufactured on the same circuit board. Even though all of the measured filters were fabricated on the same circuit board, the center frequencies of the filters varied. In addition, the manufacturing tolerances might vary amongst resonators within the same filter, as observed in Filter 5 performance shown in Figure 3.1. Hence, post-fabrication frequency tuning is required to compensate for manufacturing and material variations in each filter's resonator.

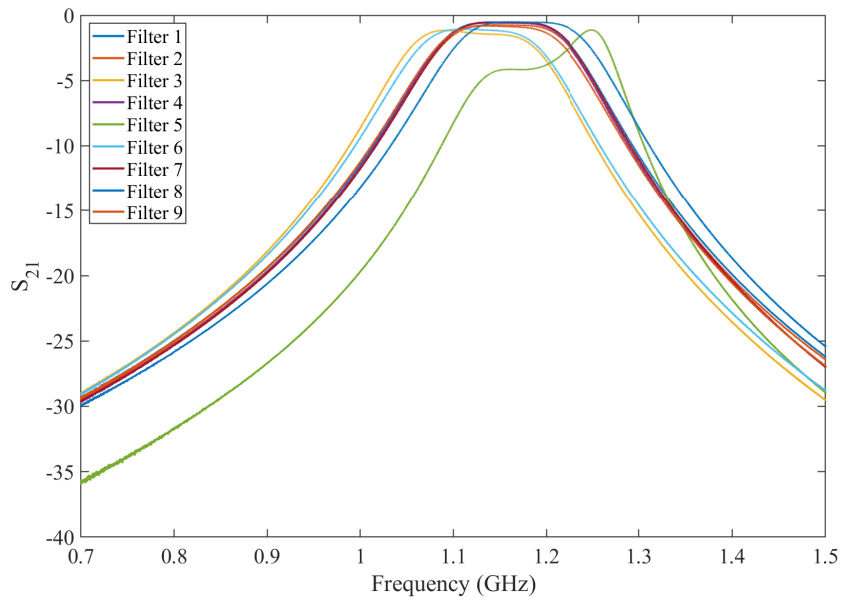


Figure 3.1: The measured S_{21} of the nine fabricated filters showing frequency variations due to the materials and fabrication tolerances.

The proposed ELCSIW resonator is composed of a bottom dielectric substrate (TMM3) and an upper air gap constructed in Isola prepreg. According to the manufacturer's datasheet, the dielectric constant of TMM3 substrate is 3.45, with a tolerance of ± 0.032 [65]. The resonator depicted in Figure 2.1 is simulated using the eigenmode HFSS solver with the variation in the dielectric constant, to analyze the impact of the dielectric constant tolerance on the resonator resonant

frequency, and the results are shown in Figure 3.2. In the figure, the tolerance range for the TMM3 dielectric constant is highlighted with a gray rectangle. Due to the electric field distribution being more concentrated in the air gap than in the dielectric substrate, it can be observed that the dielectric constant variation has a minimal effect on the resonant frequency. The tolerance of the dielectric constant of the substrate (H_1) causes a small perturbation in fields, leading to less than 0.2 % shift in the resonant frequency.

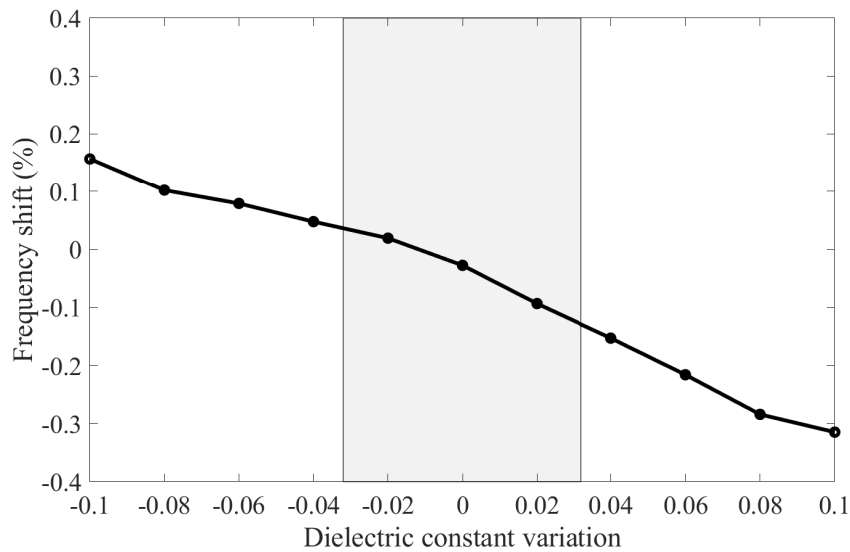


Figure 3.2: The shift in the resonant frequency of the proposed ELCSIW resonator versus the dielectric constant tolerance of the substrate of thickness $H_1 = 3.378$ mm).

Furthermore, the resonant frequency of the ELCSIW resonator is studied as a function of the dielectric substrate thickness (H_1) tolerance. The manufacturer estimates a thickness tolerance of $\pm 38.1 \mu\text{m}$ for a TMM3 substrate [65]. Since the substrate H_1 is stacked of three layers of TMM3, maximum tolerance of $\pm 114 \mu\text{m}$ may occur. In Figure 3.3, the variation of H_1 versus its impact on the resonant frequency is presented. A 1.5 % change in the resonance frequency is observable due to $114 \mu\text{m}$ substrate tolerance. This shift is caused by the variation in the cavity inductance, which is a function of the post length. However, this may

be mitigated by measuring the actual thickness of the substrate and taking it into account during the design process. For the SpeedWave prepreg used to bond between Sub1 layers, the manufacturer estimates a thickness tolerance of $\pm 12.7 \mu\text{m}$ [66]. Two SpeedWave prepreg are used in bonding three TMM3 substrates. Thus, maximum tolerance of $\pm 25.4 \mu\text{m}$ may occur. From Figure 3.3, A 0.3 % change in the resonance frequency is observable due to $25.4 \mu\text{m}$ prepreg tolerance affecting H_1 . The tolerance of the SpeedWave prepreg is found insignificant and it can be considered negligible.

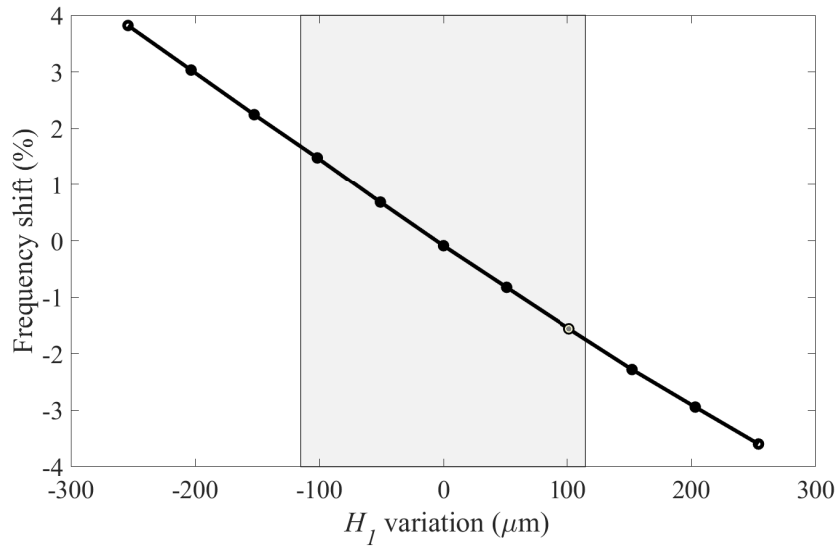


Figure 3.3: The shift in the resonant frequency of the proposed ELCSIW resonator versus the variation in the dielectric substrate of the thickness (H_1).

Additionally, the impact of Isola prepreg thickness (H_2) on resonant frequency is studied. Isola prepreg is a low-flow resin adhesive material that bonds dielectric substrates through a high-pressure and high-temperature lamination process. This prepreg has a thickness of $68.58 \mu\text{m}$ and a tolerance of $\pm 7.62 \mu\text{m}$. The lamination process may result in further thickness variations due to lamination imperfections such as uneven substrate surfaces. Therefore, eigenmode

simulations are performed to evaluate the effect of the H_2 thickness on the resonant frequency, and the results are shown in Figure 3.4. It can be seen that H_2 significantly impacts the resonant frequency of the ELCSIW resonator. With a tolerance of only $7.62 \mu\text{m}$, the resonant frequency can deviate by 10 % from the designed frequency. This resonant frequency fluctuation can significantly impact the practicality of using this technology for designing compact filters.

The investigation of the materials' properties showed that the thickness of the prepreg used to form the air gap is crucial in the fabrication process. From the characterization of the Isola prepreg lamination process, it has been observed that the final prepreg thickness (H_2) becomes between $50 \mu\text{m}$ to $64 \mu\text{m}$ after the lamination. Therefore, compensating for the frequency shift in the proposed ELCSIW resonator will primarily be for the Isola prepreg thickness tolerance.

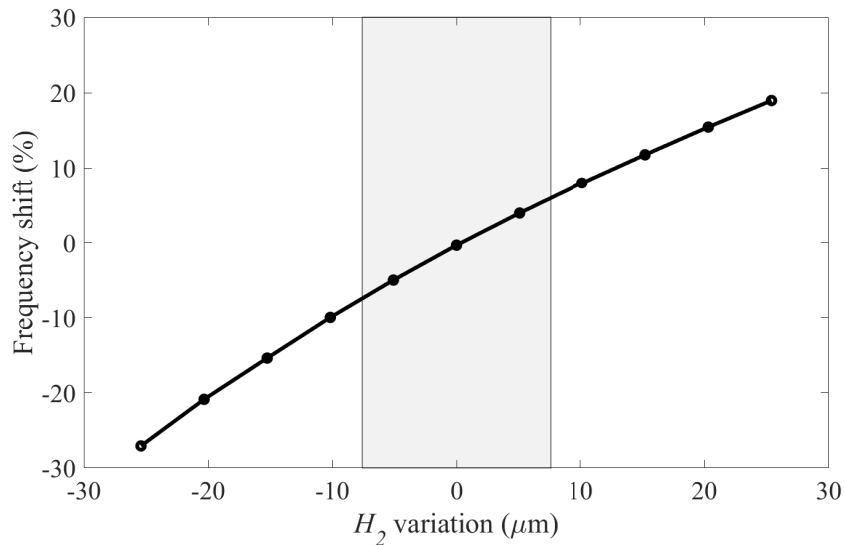


Figure 3.4: The shift in the resonant frequency of the proposed ELCSIW resonator versus the variation in the prepreg substrate thickness (H_2).

3.1 Post-Fabrication Tuning Circuit Model

Using screws and discs to mechanically adjust a resonator's frequency is widely used for post-fabrication tuning in dielectric resonators and waveguide filters

[67–70]. By altering the field distribution inside the resonating structure, metallic screws can be used to adjust the resonator’s frequency. For ELCSIW filters, the ability to insert screws in a compact cavity is limited due to the extremely small resonator size. The electric field is concentrated in the small micrometer-scale air gap, which is difficult to manually adjust using screws or other mechanical means. In addition, the metallic patch is extended over the cavity area, and inserting a screw while avoiding contact with the patch is challenging.

Electrical tuning using varactor diodes is another method of tuning the resonant frequency of a resonator [71]. Varactors diodes are semiconductor junction devices in which the junction capacitance is controlled by reverse-bias DC voltage. Filter tuning using varactors diodes has been realized in microstrip resonators, substrate-integrated cavity resonators, and evanescent-mode cavity resonators [72–76]. The low-quality factor of varactor diodes limits the quality factor of varactor-tuned cavity filters, which is generally in the range of 50–200 due to varactor semiconductor losses [77, 78]. In addition, the electrical tuning approach requires an extra circuit to adjust the DC bias of the variable capacitor. Therefore, the electrical tuning method is incompatible with the ELCSIW filter implementation.

A recent approach to cavity tuning consists of using Radio-Frequency Microelectromechanical System (RF-MEMS) tuning elements [79–82]. RF-MEMS switches, switches capacitors, and varactors are examples of RF-MEMS tuning elements. For instance, RF-MEMS varactors achieve variable gap parallel plate capacitance using micrometer-scale movable deflectable beams that is controlled by a DC bias. Low loss and high linearity are examples of the advantages of RF-MEMS varactors [83]. However, they also require extra circuitry and integration into the proposed ELCSIW filter to tune the resonant frequency, which adds additional complexity and fabrication cost.

In order to adjust the resonant frequency of the ELCSIW resonator while adhering to the design constraints, a novel post-fabrication tuning mechanism is invented. The novel tuning circuit is depicted in Figure 3.5. A single tuning configuration consists of a tuning stripline coupled to the patch and a through via to connect the stripline to the top layer and the ground plane. This configuration allows for two parallel plate capacitances between the tuning stripline and the patch and bottom ground plane. The stripline has a length L_t and width W_t , and it is separated from the patch by a substrate with a thickness H_t and dielectric constant ϵ_t . A tuning via with a diameter D_t and length H_m forms the tuning inductance. The tuning stripline can be electrically disconnected from the ground plane by removing the top copper strip (State OFF). The stripline can be connected again by soldering the via pad to the top copper layer (State ON). This reversible connection can be used to vary the inductance and capacitance of the tunable ELCSIW resonator, which as a result, varies the cavity's resonant frequency. The resonant frequency of the tuned cavity is determined by [4]

$$f_r = \frac{1}{2\pi\sqrt{C_{total}L_{total}}}. \quad (3.1)$$

This single tuning configuration can be duplicated and embedded into the ELCSIW cavity to have flexibility in the tuning range. Eight tuning elements are adopted in this design of the tunable ELCSIW resonator. To understand the effect of the tuning mechanism on the proposed resonator, a lumped element equivalent circuit for the tuned resonator is modeled and presented in Figure 3.6. All lumped capacitors are assumed to be in parallel. When all loading striplines are grounded, the total capacitance of the cavity can be expressed as

$$C_{total} = C_t + C_b + C_{coax} + (C_{st1} + C_{sb1}) + \dots + (C_{sti} + C_{sbi}), \quad i = 1, 2, \dots, N, \quad (3.2)$$

where C_{st} and C_{sb} are the capacitance between the stripline and the patch and the stripline and bottom metallic layer, respectively. N denotes the number of loading striplines embedded into the cavity. C_t , C_b , and C_{coax} can be determined using (2.4) and (2.8) as described in Chapter 2.

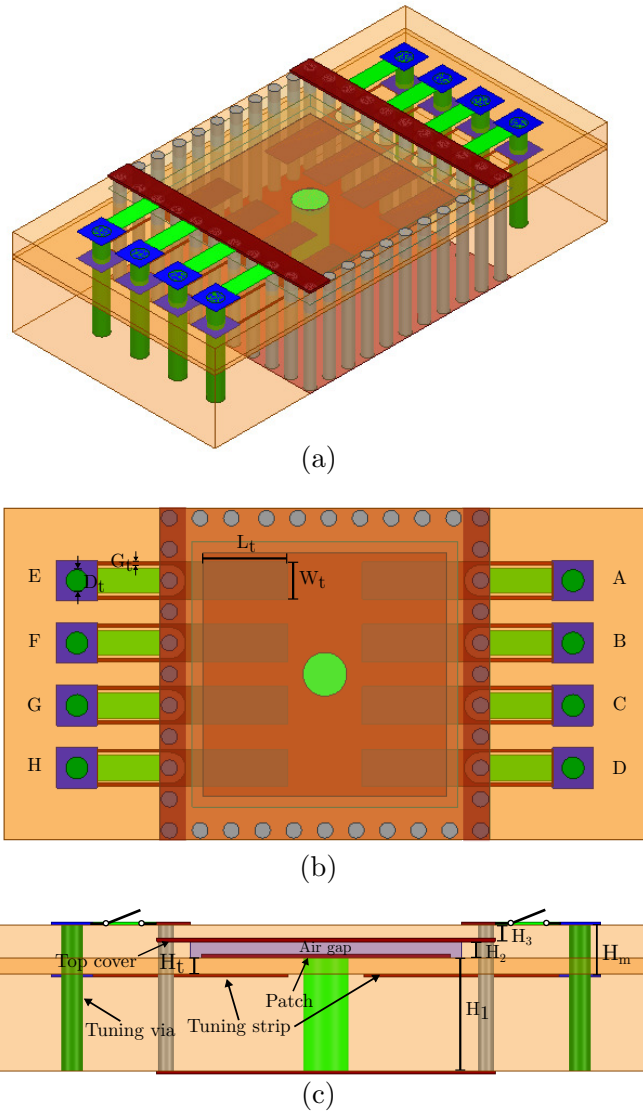


Figure 3.5: The structure of the proposed post-fabrication tunable ELCSIW resonator, (a) a 3D view, (b) top view, and (c) side view. The design parameters are presented in Table 3.1.

The tuning capacitances C_{st} and C_{sb} , including the fringing fields, can be

determined by [46]

$$C = \epsilon_t \epsilon_0 \frac{L_t W_t}{g} + \frac{\epsilon_t \epsilon_0 W_t}{\pi} \left(1 + \ln \left(\frac{\pi W_t}{g} \right) \right) + \frac{\epsilon_t \epsilon_0 L_t}{\pi} \left(1 + \ln \left(\frac{\pi L_t}{g} \right) \right), \quad (3.3)$$

where g is the separation between the parallel plates. The first term in (3.3) represents the parallel plate capacitance between the loading stripline and the patch, whereas the other two terms represent the fringing field effect on both ends of the stripline. The capacitance of the tuning stripline varies based on its length and width and distance from the patch. Also, the dielectric constant of the substrate that separates the stripline from the patch can be selected to increase or decrease tuning capacitance.

Table 3.1: The post-fabrication tunable ELCSIW resonator design parameters. All dimensions are in mm.

Design Parameter	Value
Cavity length (W)	10
Patch width (W_r)	7.8
Post diameter (D)	1.4
Air cavity to via spacing (S_1)	0.9
Outer via diameter (d)	0.5
Outer via spacing (p)	1
Bottom substrate thickness (H_1)	3.378 (133 mils)
Isola prepreg thickness (H_2)	0.0685 (2.7 mils)
Copper clad thickness (t)	0.0175
Tuning via diameter (D_t)	0.7
Tuning stripline length (L_t)	2.7
Tuning stripline width (W_t)	1.2
Tuning thin stripline width (G_t)	0.1
Tuning substrate thickness (H_t)	0.2032 (8 mils)

The lumped inductance of the post and the vias connecting tuning striplines to the ground are also assumed to be in parallel. The total inductance of the tuned cavity is expressed as

$$L_{total} = \frac{1}{\frac{1}{L_{coax}} + \frac{1}{L_{t1}} + \frac{1}{L_{t2}} + \dots + \frac{1}{L_{ti}}}, \quad i = 1, 2, \dots, N, \quad (3.4)$$

where N denotes the number of tuning striplines embedded into the cavity. L_{coax} can be determined by (2.9) as discussed in Chapter 2. The inductance of the tuning via connecting the tuning stripline to the ground plane is approximated by [51]

$$L_{ti} \approx 5.08h \left[\ln\left(\frac{4h}{r}\right) + 1 \right] \quad [\text{nH}] \quad i = 1, 2, \dots, N, \quad (3.5)$$

where h and r are the vias' length and diameter in inches, respectively. The tuning inductance is proportional to the length of the via and inversely proportional to its diameter.

3.2 Post-Fabrication Tuning Mechanism

The post-fabrication tuning mechanism compensates for the frequency shifts introduced by the materials and fabrication tolerances by connecting or disconnecting the embedded tuning elements. The frequency tuning range and step size are determined by the tuning substrate of thickness H_t and its dielectric constant ϵ_t . The tuning striplines can be identical in size or with different lengths to obtain different frequency tuning steps.

As was previously mentioned, the resonant frequency can fluctuate by 10 %

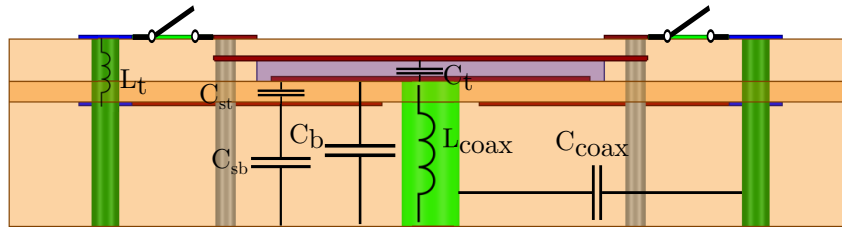


Figure 3.6: Circuit model of the proposed post-fabrication tunable ELCSIW resonator.

depending on the tolerance of the Isola prepreg thickness (H_2). Measurements, taken during experiments designed to characterize the lamination process, have indicated that H_2 ranges between 50-64 μm , despite 68.58 μm being reported as the nominal thickness. This decrease in the thickness increases the capacitance between the patch and the top cover, hence decreasing the resonant frequency. Thus, the post-fabrication tuning primarily focuses on addressing this issue to obtain the desired operating frequency.

To evaluate the impact of H_2 on the resonant frequency of the tunable ELCSIW resonator, full-wave HFSS simulations are performed for the resonator in Figure 3.5, and the results are shown in Figure 3.7. It can be observed that a 3 μm decrease in Isola prepreg thickness causes a 20 MHz downward shift of the resonant frequency. At an Isola prepreg thickness of 56 μm , the tunable resonator's resonant frequency shifts by approximately 9 %. Multiple tuning striplines may be disconnected to unload the cavity to compensate for this frequency shift. Figure 3.8 demonstrates the effect of disconnecting the tuning striplines on the mistuned ELCSIW resonator with H_2 thickness of 56 μm . The switches are labeled alphabetically in Figure 3.5, and the switches' states are defined in Table 3.2. It is necessary to turn off all switches but switch H to compensate for the frequency shift caused by the Isola prepreg tolerance, as shown in Figure 3.8. This can demonstrate the benefit of the proposed post-fabrication tuning method, which requires no active elements or additional control circuits. Also, the proposed post-fabrication tuning circuit does not require complex integration and can be implemented using the standard PCB fabrication process.

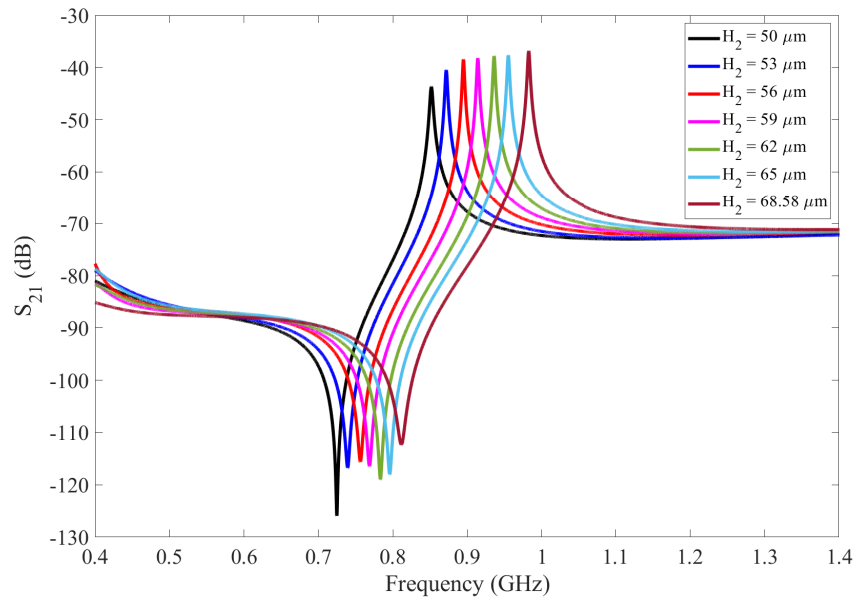


Figure 3.7: The effect of the H_2 tolerance on the resonant frequency of the sample resonator in Figure 3.5.

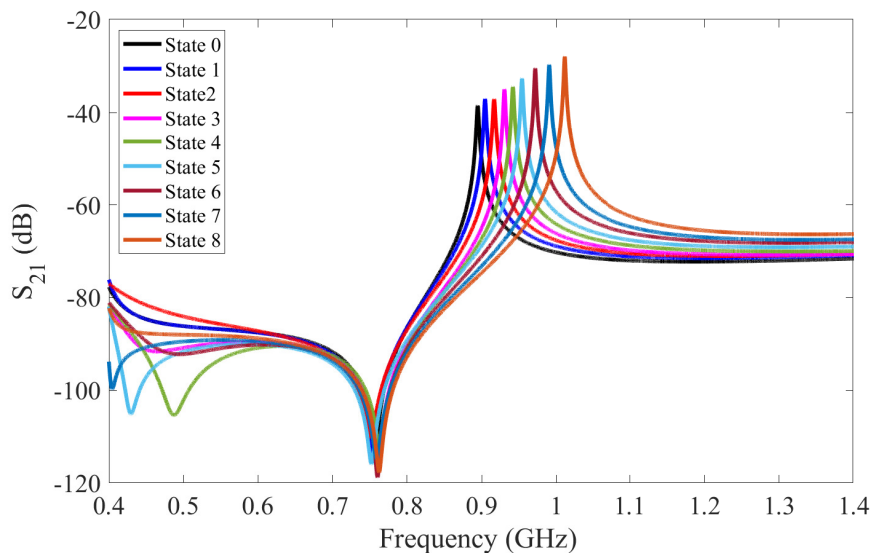


Figure 3.8: The impact of all switch states on the resonant frequency of the sample resonator in Figure 3.5.

Table 3.2: Switch states of the tunable ELCSIW filter. ON: switch is connected, OFF: switch is disconnected.

State\Switch	A	B	C	D	E	F	G	H
0	ON	ON	ON	ON	ON	ON	ON	ON
1	OFF	ON	ON	ON	ON	ON	ON	ON
2	OFF	OFF	ON	ON	ON	ON	ON	ON
3	OFF	OFF	OFF	ON	ON	ON	ON	ON
4	OFF	OFF	OFF	OFF	ON	ON	ON	ON
5	OFF	OFF	OFF	OFF	OFF	ON	ON	ON
6	OFF	OFF	OFF	OFF	OFF	OFF	ON	ON
7	OFF	OFF	OFF	OFF	OFF	OFF	OFF	ON
8	OFF	OFF	OFF	OFF	OFF	OFF	OFF	OFF

The post-fabrication tuning mechanism is affected by the tuning stripline area, the dielectric constant of the tuning substrate (ϵ_t), and the substrate thickness (H_t). Full-wave HFSS simulations of the tunable resonator in Figure 3.5 are conducted to evaluate the impact of each parameter on the resonant frequency. The resonator is implemented in the full-wave HFSS solver with a weak external coupling. The tuning striplines' length and width are 2.7 mm and 1.2 mm, respectively. The dielectric constant of the tuning substrate is set to 3.45. The simulations are performed on three different tuning substrate thicknesses. Figure 3.9 shows the transmission coefficient (S_{21}) of the tunable resonator in two switch states, State 0 and State 8. State 0 indicates that all switches are connected, whereas State 8 indicates that all switches are disconnected. The two states reflect the circuit's maximum tunability at each value of H_t . For a thin tuning substrate of 0.127 mm, it can be noticed that the resonant frequency can shift 25 % by disconnecting all the striplines. With such a small gap filled with dielectric material between the tuning striplines and the patch, the tuning capacitance (C_{st}) can change significantly depending on the switch configuration. Increasing H_t will decrease C_{st} and restrict the tuning range to 8 % at a tuning

substrate thickness of 0.3048 mm. Figure 3.10 shows the tuning range of the sample resonator as a function of the tuning substrate thickness. The plot shows that a frequency tuning range of 60 % can occur at a 0.05 mm tuning substrate thickness. The limitation to having such a wide range is the availability of thin dielectric substrates.

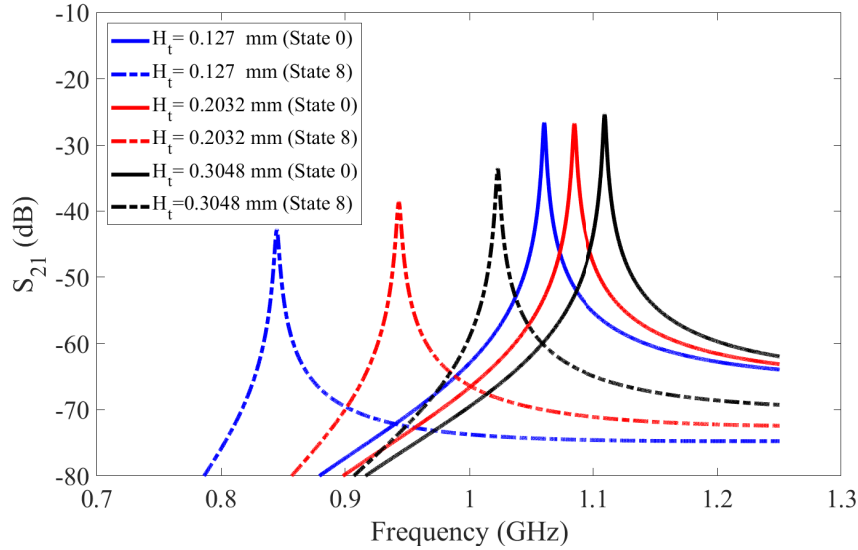


Figure 3.9: The impact on the resonant frequency tuning of the sample resonator when all switches are connected (State 0) and when all switches are disconnected (State 8). This impact shows that maximum tunability can be obtained for the sample resonator with $\epsilon_t = 3.45$, $L_t = 2.7$ mm, and $W_t = 1.2$ mm.

Moreover, the tuning substrate dielectric constant is proportional to the tuning capacitance as suggested by (3.3). In Figure 3.11, the relationship between the frequency tuning range and ϵ_t is presented. It can be seen that increasing the tuning substrate dielectric constant allows for a large tuning range of 40 % at a substrate thickness of 0.2032 mm. The ability to use a dielectric substrate with a high dielectric constant provides additional design freedom and allows an increase in C_{st} to realize a wider tuning range.

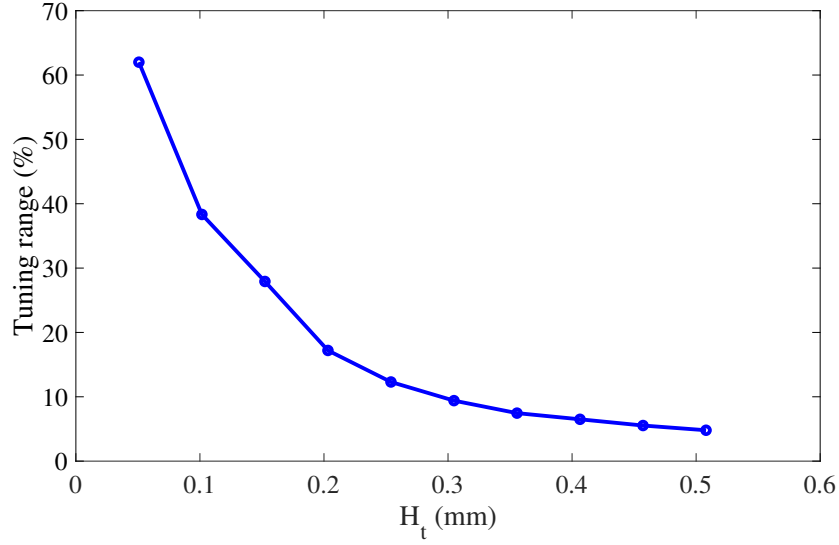


Figure 3.10: The maximum tuning range as a function of the tuning substrate thickness for the sample resonator with $\epsilon_t = 3.45$, $L_t = 2.7$ mm, and $W_t = 1.2$ mm.

In addition to the substrate properties, the length of the tuning striplines can be adjusted to obtain the desired tuning range to compensate for any tolerance in H_2 . Figure 3.12 shows the relationship between the length of the tuning striplines and the achievable tuning range. The plot shows a tuning range that increases by increasing the length of the tuning striplines. At a tuning substrate thickness of 0.127 mm, the tuning stripline length can achieve a frequency variation of 25 % when disconnecting the striplines. In comparison to the tuning range provided by the tuning substrate parameters, the range provided by the stripline length is limited. Hence, having tuning striplines of various lengths allows for finer tuning step adjustments.

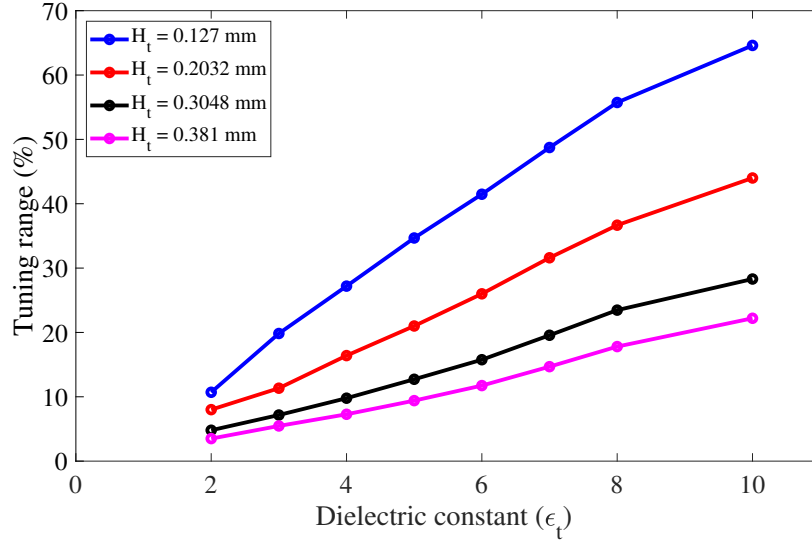


Figure 3.11: The maximum tuning range as a function of the tuning substrate dielectric constant at different tuning substrate thicknesses for the sample resonator with $L_t = 2.7$ mm and $W_t = 1.2$ mm.

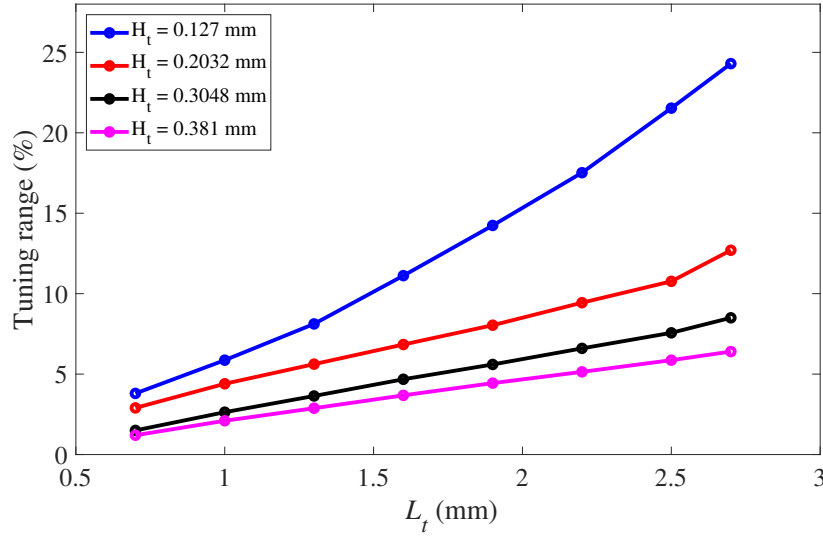


Figure 3.12: The maximum tuning range as a function of the tuning stripline length at different tuning substrate thicknesses for the sample resonator with $\epsilon_t = 3.45$ mm and $W_t = 1.2$ mm.

Equally significant to the tuning range that the circuit can provide is the quality factor that the tunable ELCSIW resonator can achieve. The primary goal of designing the ELCSIW resonator is to achieve an ultra-miniaturized resonator

with a high-quality factor. Embedding loading striplines into the ELCSIW cavity can perturb the fields in the cavity and cause additional losses. Thus, the impact of the tuning circuit on the quality factor of the sample tunable ELCSIW resonator in Figure 3.5 must be investigated. The tunable ELCSIW resonator has a tuning substrate thickness and a dielectric constant of 0.2032 mm and 3.45, respectively. The loss tangent of the tuning substrate ($\tan\delta_t$) is 0.002, and the stripline length is 2.7 mm. In Figure 3.13, the quality factor of the proposed tunable ELCSIW resonator and the frequency tuning range are presented as a function of tuning substrate thickness. Quality factors are observed to be lower when all switches are connected compared to when they are disconnected. This impact is a result of the change in the intensity of the electric field between the tuning stripline and the patch. Also, the quality factor drops considerably as the thickness of the tuning substrate decreases. This can be attributed to the increase of the electric field which results in higher currents crowding on the striplines and the patch. This leads to higher conductor loss and lower quality factor for the ELCSIW resonator. Selecting a tuning substrate with a high dielectric constant of 10 can decrease the quality factor by more than 40 %, as shown in Figure 3.14. This loss in the tunable ELCSIW cavity resonator is caused by the increase in the conductor loss, as a result of higher currents flowing on the metallic surfaces [4].

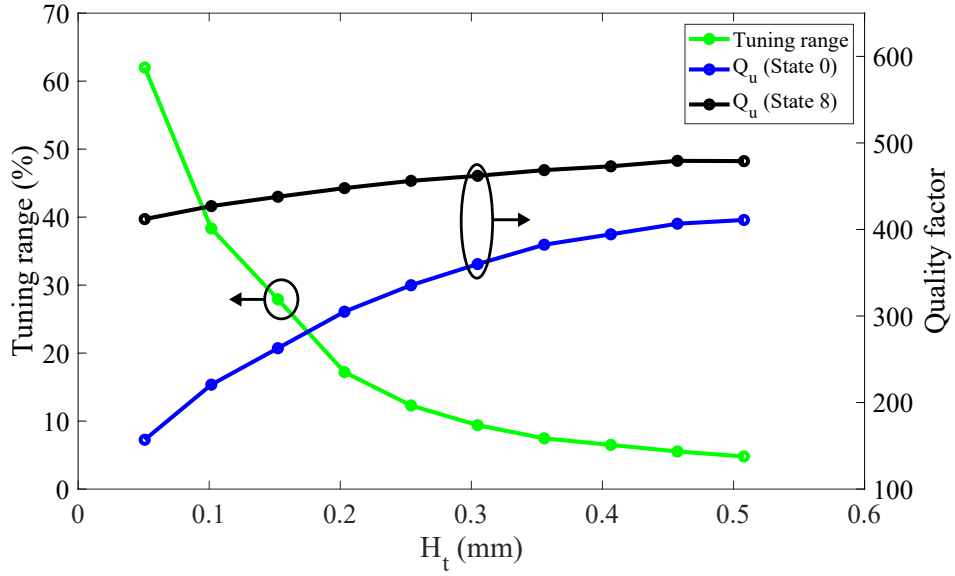


Figure 3.13: The maximum tuning range and quality factor of the sample tunable ELCSIW resonator as a function of the tuning substrate thickness with $\epsilon_t = 3.45$ mm, $\tan\delta_t = 0.002$, $L_t = 2.7$ mm, and $W_t = 1.2$ mm.

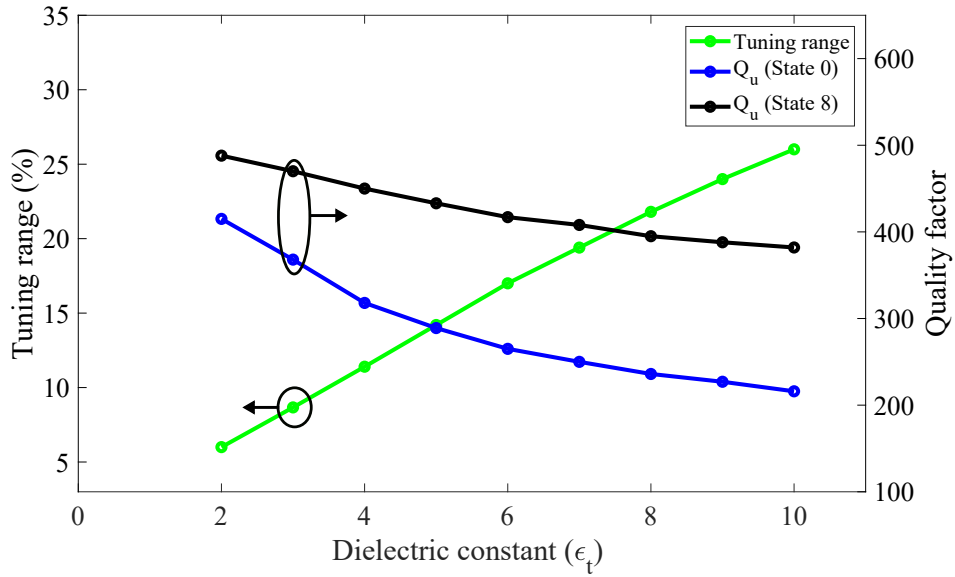


Figure 3.14: The maximum tuning range and quality factor of the sample tunable ELCSIW resonator as a function of the tuning substrate dielectric constant with $\tan\delta_t = 0.002$, $H_t = 0.2032$ $L_t = 2.7$ mm, and $W_t = 1.2$ mm.

The material's loss tangent primarily defines the dielectric loss caused by the

cavity substrates. The dielectric loss of the tuning substrate affects the overall unloaded quality factor of the tuned resonator. To determine the impact of the loss tangent on the unloaded quality factor, full-wave HFSS simulations are conducted for different loss tangent values of the tuning substrate at multiple substrate thicknesses. Figure 3.15 shows the relationship between the loss tangent and the unloaded quality factor, as the quality factor decreases when the substrate loss tangent increases. Also, the figure shows that the quality factor degrades at different tuning substrate thicknesses at the same rate when the loss tangent increases.

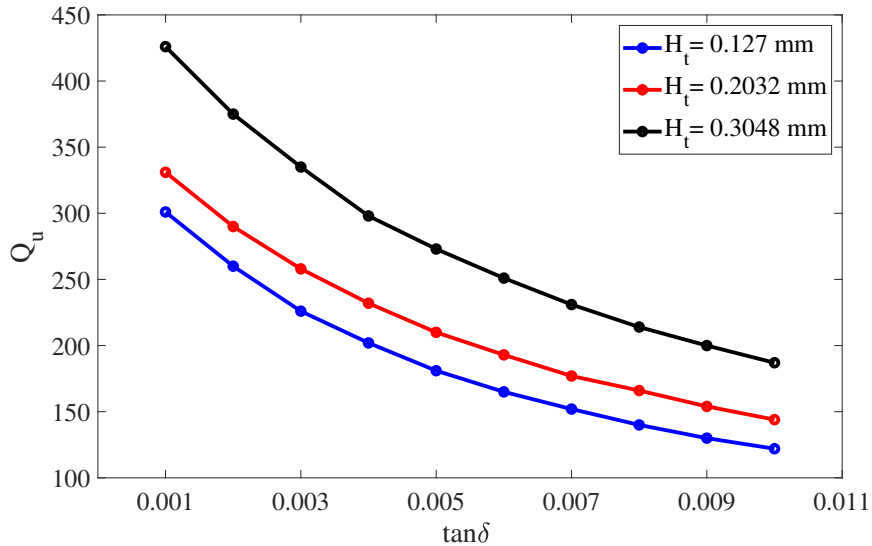


Figure 3.15: The unloaded quality factor of the sample tunable ELCSIW resonator as a function of the tuning substrate loss tangent at various tuning substrate thicknesses.

The quality factors shown in Figures 3.13 and 3.14 are determined at different frequencies due to the variation of the loading from the tuning circuit. The impact of the tuning circuit on the ELCSIW resonator quality factor is best demonstrated by comparing tunable and non-tunable versions of the resonator operating at the same resonant frequency. In section 2.2.3, an ELCSIW resonator operating at 1.05 GHz with 99 % miniaturization factor was simulated, and the

extracted unloaded quality factor is found to be 480. Similarly, the tunable ELCSIW resonator in Figure 2.3 is adjusted and simulated to operate at 1.05 GHz with $L_t = 2.7$ mm, $W_t = 1.2$ mm, $H_t = 0.2032$ mm, $\epsilon_t = 3.45$, and $\tan\delta_t = 0.002$. The simulated transmission coefficient of the tuned resonator is presented in Figure 3.16. The unloaded quality factor is extracted using (2.19) and found to be 315. For $\tan\delta_t=0.001$, the extracted unloaded quality factor of the tunable ELCSIW resonator is found to be 365. This comparison demonstrates that the tuning circuit can improve the ELCSIW technology's reliability at the expense of a decrease in the quality factor.

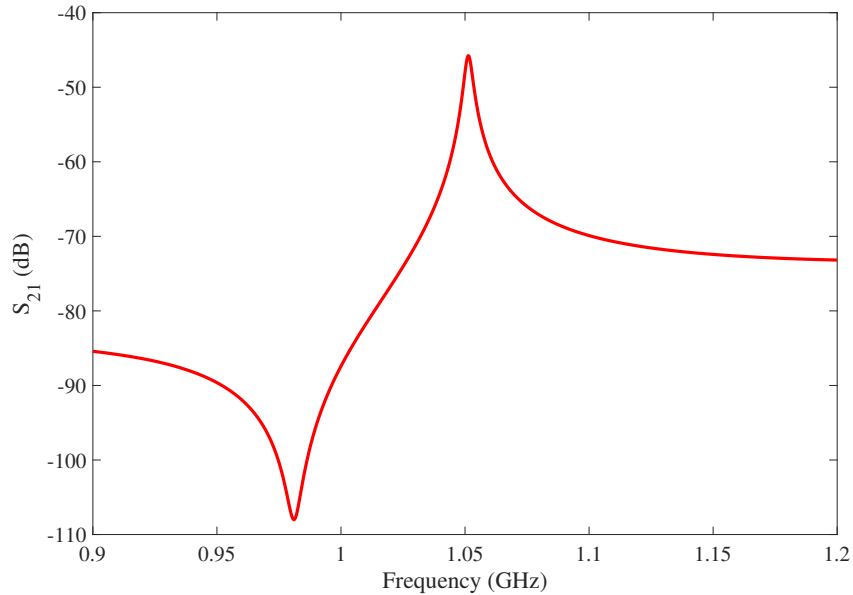


Figure 3.16: The transmission coefficient of a weakly coupled tunable ELCSIW cavity resonator.

From the above parametric investigation, it can be concluded that the tuning circuit needs to be carefully designed to account for the manufacturing tolerance while maintaining a high quality factor.

3.3 Post-Fabrication Frequency Tuning Filter

Two second-order tunable ELCSIW filters are designed and simulated to demonstrate the mechanism and the benefits of the tuning circuit in compensating for the fabrication tolerances. The filters are going to be named filter A and filter B throughout the section. The filters are designed to operate in the lower L-band frequency, arbitrarily at 1.04 GHz. The filters have 70 MHz bandwidth, which is equivalent to 6.3 % fractional bandwidth, and an equi-ripple of 20 dB. The input/output feed lines consist of 50 Ω coplanar waveguides connected to tap striplines through vertical transition vias. These tap striplines are short-circuited to the post of the resonators and allow for magnetic coupling to the cavity. The structure of the second-order tunable filter is shown in Figure 3.17.

The design procedure for ELCSIW filter with the post-fabrication tuning circuit is described as follows:

1. Determine experimentally the maximum and minimum thickness of Isola prepreg that can be obtained after a full cycle of lamination.
2. Determine the maximum frequency shift caused by the tolerance of Isola prepreg thickness obtained in step 1.
3. Design and obtain the initial dimensions of the ELCSIW filter following the procedure in section 2.3.
4. Select the tuning substrate thickness and dielectric constant that can compensate for the frequency shift obtained in step (2) using the parametric analysis presented in section 3.2.
5. Measure the fabricated filter S-parameters and determine the shift in the resonant frequency compared to the designed, if any.

6. Simulate the filter with different combination of switches states and identify the switches that need to be disconnected.
7. Disconnect the identified switches and measure the filter S-parameters.

The first tunable ELCSIW filter A is designed to have a tuning circuit that can compensate for up to 6 % shift in the resonant frequency. This possible frequency shift is a result of the Isola prepreg expected to have a thickness from 58 μm to 68 μm after the lamination process. For filter A, the material used to implement the design is Rogers TMM3, which has a dielectric constant of 3.45 and a loss tangent of 0.002. Following the procedure described in section 3.2, the physical dimensions of the tunable ELCSIW filter and its tuning circuit are obtained and presented in Table 3.3. The tuning circuit is designed to have eight tuning striplines with different lengths to allow fine-tuning of the filter response. The tuning strip lines are labeled alphabetically and arranged to be symmetrical around the filter center plane.

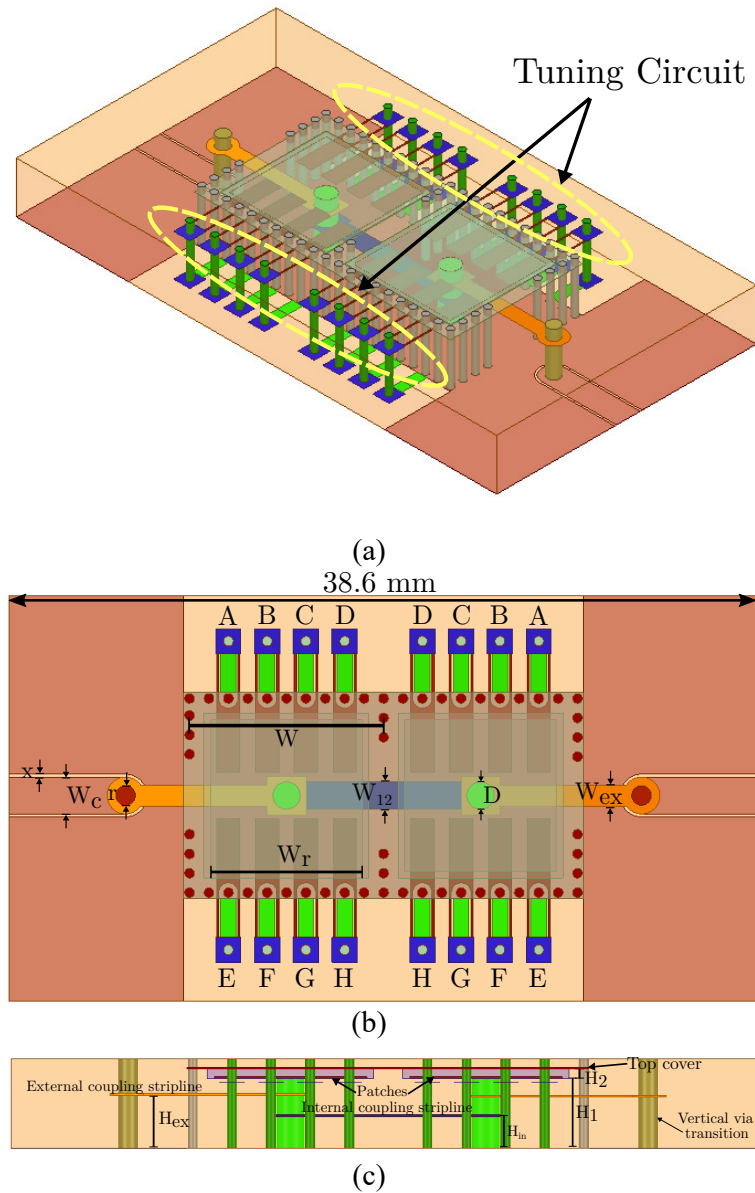


Figure 3.17: The structure of the proposed post-fabrication tunable ELCSIW filter, (a) a 3D view, (b) top view, (c) side view.

To demonstrate the impact of the tolerance of the Isola prepreg thickness (H_2), simulations of the filter A with a variation of H_2 are performed, and the results are shown in Figure 3.18. The filter is assumed to have H_2 of $58 \mu\text{m}$, instead of the nominal design thickness of $68.58 \mu\text{m}$, as a result of the lamination process and material tolerances. The filter performance with the nominal thickness and defected thickness of H_2 is depicted in Figure 3.19. It can be seen

Table 3.3: Second-order post-fabrication tunable ELCSIW filter design parameters (filter A). All dimensions are in mm.

Design Parameter	Value
Cavity length (W)	10
Patch width (W_r)	7.8
Post diameter (D)	1.6
Coplanar waveguide width (W_c)	1.9
Coplanar waveguide gap width (x)	0.15
Vertical via transition diameter (D_v)	1
Air cavity to via spacing (S_1)	0.9
Outer via diameter (d)	0.5
Outer via spacing (p)	1
Bottom substrate thickness (H_1)	3.5052 (138 mils)
Isola prepreg thickness (H_2)	0.0685 (2.7 mils)
Top substrate thickness (H_3)	0.635 (25 mils)
External tap height (H_{ex})	2.794 (110 mils)
Inter-resonator tap height (H_{in})	1.5748 (62 mils)
Copper clad thickness (t)	0.0175
Inter-resonator stripline width (W_{12})	1.6
External coupling stripline width (W_{ex})	1
Tuning substrate dielectric constant (ϵ_t)	3.55
Tuning via diameter (D_t)	0.5
Tuning strip width (W_t)	1.2
Tuning thin strip width (G_t)	0.1
Tuning substrate thickness (H_t)	0.127 (5 mils)
Switch A tuning strip length (L_t)	1.9
Switch B tuning strip length (L_t)	2.1
Switch C tuning strip length (L_t)	2.4
Switch D tuning strip length (L_t)	2.4
Switch E tuning strip length (L_t)	1.9
Switch F tuning strip length (L_t)	2.1
Switch G tuning strip length (L_t)	2.4
Switch H tuning strip length (L_t)	2.4

that the center frequency of the filter is shifted from 1.04 GHz to 0.970 GHz as H_2 is assumed to be 58 μm after the lamination process. Multiple tuning switches may be disconnected to compensate for this frequency shift. Since the tuning strip lines have different lengths, different combinations of switch states, listed in Table 3.4, are implemented in the simulation to show the compensation process to get to the nominal resonant frequency. The simulation results of the switch states in Table 3.4 are shown in Figure 3.20. It can be observed that the filter center frequency shifts upward when a tuning strip line is disconnected. The filter center frequency is re-tuned to the designed frequency at 1.040 GHz when switches A, B, C, F, and G are disconnected. The S-parameters of the

tunable ELCSIW initial designed filter and the post-tuned filter are plotted in Figure 3.21. Despite the material thickness tolerance, the performance of the post-tuned filter has good agreement with the designed filter performance.

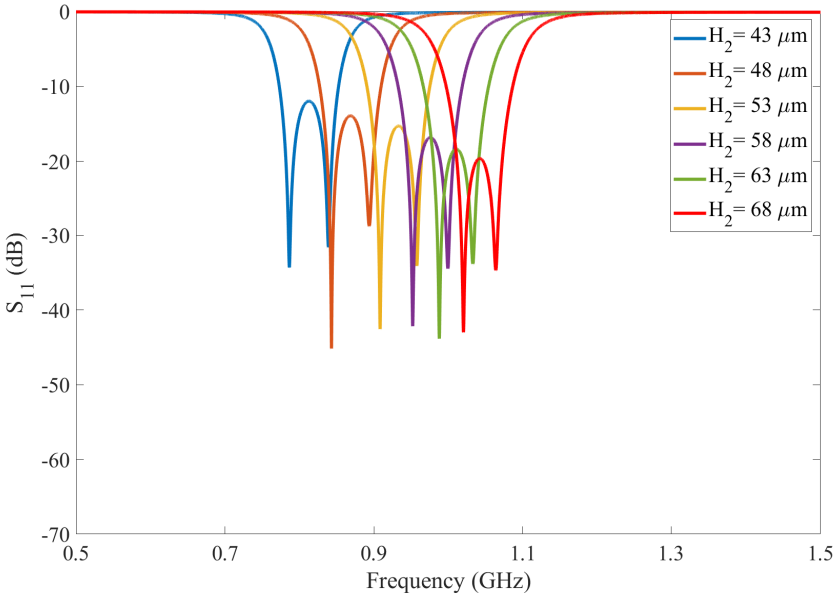


Figure 3.18: The impact of Isola prepreg thickness variations on the tunable ELCSIW filter center frequency. Showing only S_{11} for clarity.

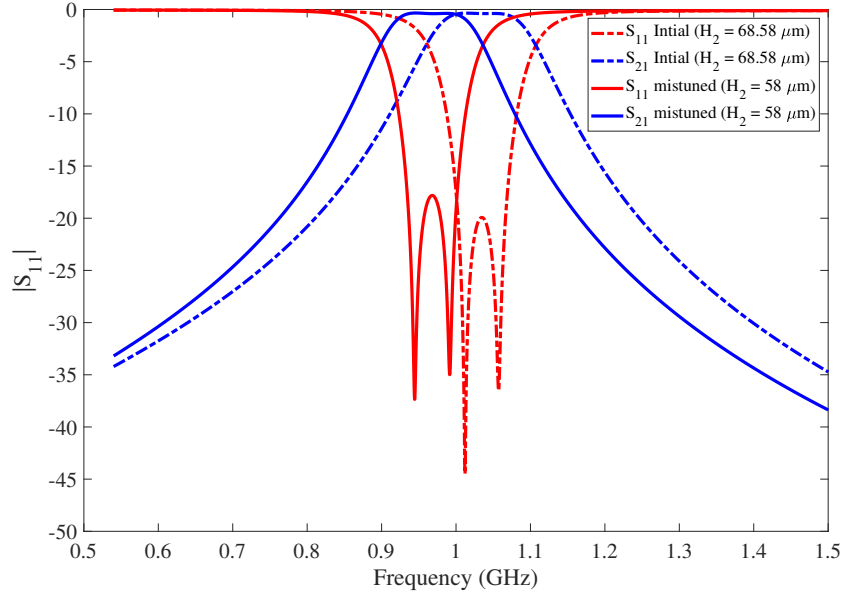


Figure 3.19: S-parameters of the tunable ELCSIW filter (filter A) at $H_2 = 68.58 \mu\text{m}$ and $H_2 = 58 \mu\text{m}$.

Table 3.4: Switch states of the tunable ELCSIW filter (filter A). ON: switch is connected, OFF: switch is disconnected.

State\Switch	A	B	C	D	E	F	G	H
0	ON	ON	ON	ON	ON	ON	ON	ON
1	OFF	ON	ON	ON	ON	ON	ON	ON
2	OFF	OFF	ON	ON	ON	ON	ON	ON
3	OFF	OFF	OFF	ON	ON	ON	ON	ON
4	OFF	OFF	OFF	ON	ON	OFF	ON	ON
5	OFF	OFF	OFF	ON	ON	OFF	OFF	ON

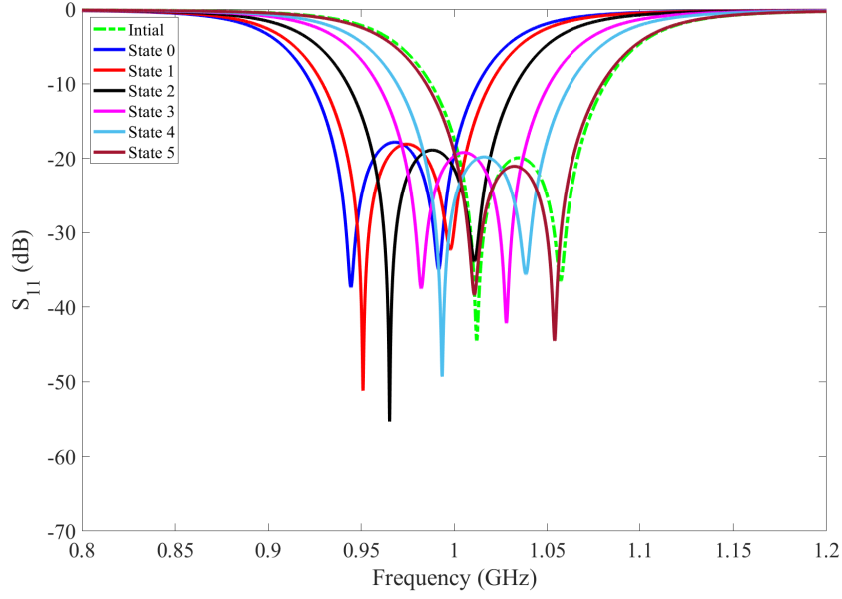


Figure 3.20: The impact of disconnecting tuning switches of the tunable ELCSIW filter (filter A) on the center frequency. Initial: initial design of the ELCSIW filter with $H_2 = 68.58 \mu\text{m}$. Showing only S_{11} for clarity.

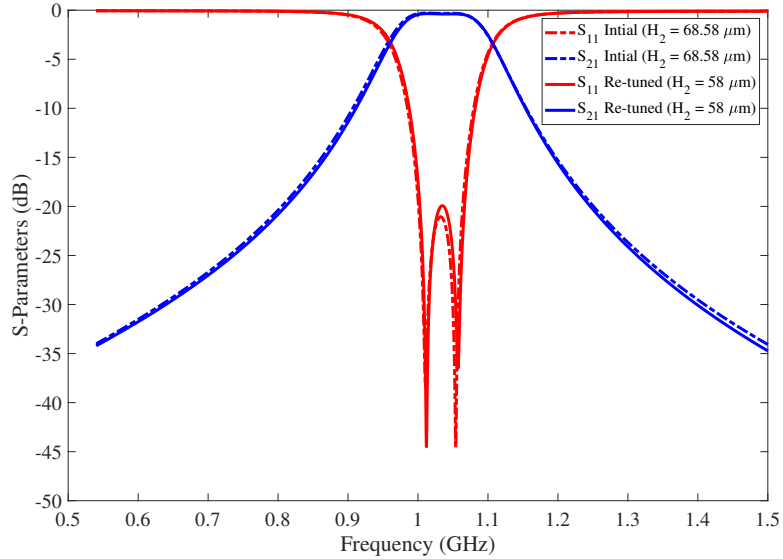


Figure 3.21: S-parameters of the designed tunable ELCSIW filter (filter A) with $H_2 = 68.58 \mu\text{m}$ and the re-tuned ELCSIW filter (filter A) with $H_2 = 58 \mu\text{m}$.

In filter B, the filter is assumed to have the Isola prepreg thickness H_2 to be

50 μm instead of the nominal design thickness of 68.58 μm as a result of the lamination process and material tolerances. The filter performance with the nominal thickness and defected thickness of H_2 are depicted in Figure 3.22. It can be seen that the center frequency of the filter is shifted from 1.04 GHz to 0.942 GHz as the H_2 is assumed to be 50 μm after the lamination process. Multiple tuning switches may be disconnected to compensate for this frequency shift. Different combinations of the switches state are implemented in the simulation and listed in Table 3.5. The simulation results of the states in Table 3.5 are shown in Figure 3.23. The filter center frequency is re-tuned to the designed frequency at 1.04 GHz when switches A, B, C, E, and G are disconnected. The S-parameters of the tunable ELCSIW initial design and the post-tuned filter are plotted in Figure 3.24. Despite the material thickness tolerances, the performance of the post-tuned filter has good agreement with the designed filter performance.

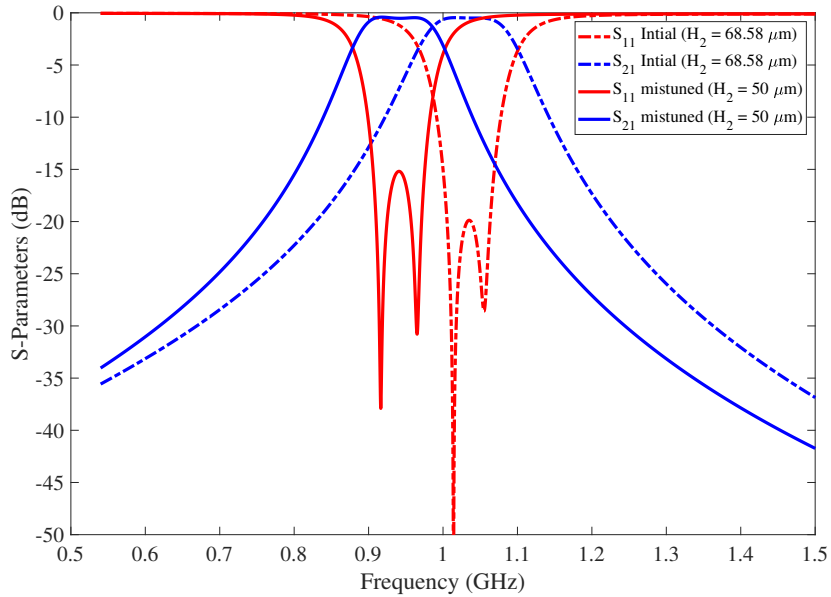


Figure 3.22: S-parameters of the tunable ELCSIW filter (filter B) at $H_2 = 68.58 \mu\text{m}$ and $H_2 = 50 \mu\text{m}$.

Table 3.5: Second-order post-fabrication tunable ELCSIW filter design parameters (filter B). All dimensions are in mm.

Design Parameter	Value
Cavity length (W)	10
Patch width (W_r)	7.8
Post diameter (D)	2.5
Coplanar waveguide width (W_c)	1.9
Coplanar waveguide gap width (x)	0.15
Vertical via transition diameter (D_v)	1
Air cavity to via spacing (S_1)	0.9
Outer via diameter (d)	0.5
Outer via spacing (p)	1
Bottom substrate thickness (H_1)	3.5052 (138 mils)
Isola prepreg thickness (H_2)	0.0685 (2.7 mils)
Top substrate thickness (H_3)	0.635 (25 mils)
External tap height (H_{ex})	3.0988 (122 mils)
Inter-resonator tap height (H_{in})	1.5748 (62 mils)
Copper clad thickness (t)	0.0175
Inter-resonator stripline width (W_{12})	1.6
External coupling stripline width (W_{ex})	1
Tuning substrate dielectric constant (ϵ_t)	6
Tuning via Diameter (D_t)	0.5
Tuning strip width (W_t)	1.2
Tuning thin strip width (G_t)	0.1
Tuning substrate thickness (H_t)	0.127 (5 mils)
Switch A tuning strip length (L_t)	2.4
Switch B tuning strip length (L_t)	2.3
Switch C tuning strip length (L_t)	2.2
Switch D tuning strip length (L_t)	1.9
Switch E tuning strip length (L_t)	2.4
Switch F tuning strip length (L_t)	2.3
Switch G tuning strip length (L_t)	2.2
Switch H tuning strip length (L_t)	1.9

Table 3.6: Switch states of the tunable ELCSIW filter (filter B). ON: switch is connected, OFF: switch is disconnected.

State\Switch	A	B	C	D	E	F	G	H
0	ON	ON	ON	ON	ON	ON	ON	ON
1	OFF	ON	ON	ON	ON	ON	ON	ON
2	OFF	OFF	ON	ON	ON	ON	ON	ON
3	OFF	OFF	OFF	ON	ON	ON	ON	ON
4	OFF	OFF	OFF	ON	OFF	ON	ON	ON
5	OFF	OFF	OFF	ON	OFF	ON	OFF	ON

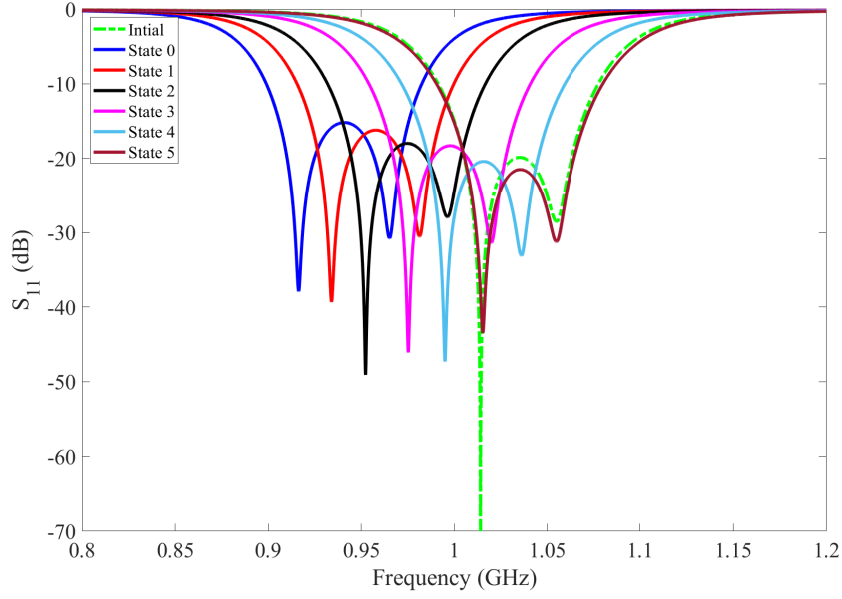


Figure 3.23: The impact of disconnecting tuning switches of the tunable ELCSIW filter (filter B) on the return loss. Initial: initial design of the ELCSIW filter with $H_2 = 68.58 \mu\text{m}$.

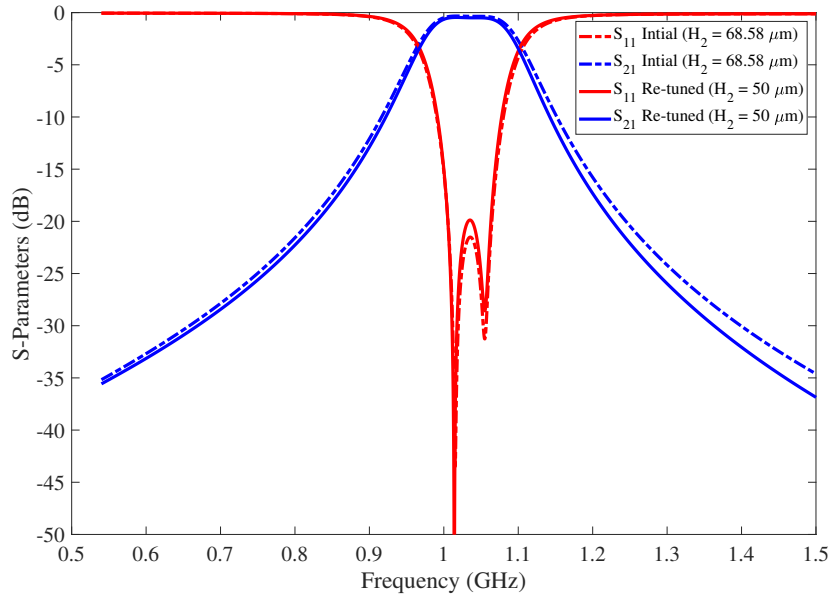


Figure 3.24: S-parameters of the designed tunable ELCSIW filter (filter B) with $H_2 = 68.58 \mu\text{m}$ and the re-tuned ELCSIW filter (filter B) with $H_2 = 50 \mu\text{m}$.

The novel post-fabrication frequency tuning technique for ELCSIW filters

has demonstrated significant benefits in obtaining the nominal response of a microwave filter. Unlike traditional tuning methods, the proposed technique does not involve mechanical tuning screws or require any active circuit components, making it feasible to implement using standard PCB fabrication processes. This technique takes into account the tolerances and variations in the materials properties that can cause differences between the simulated and measured responses of an ELCSIW filter. The ELCSIW tuning technique involves embedding electrical loading elements to the cavity resonators in the filter, which allows for the adjustment of the resonant frequency of the filter after the fabrication. The adjustment is made by connecting or disconnecting the loading elements. The simplicity and flexibility of the proposed tuning technique make it an attractive option for manufacturers of ELCSIW filters, as it can be easily incorporated into the existing fabrication process with minimal additional costs.

In conclusion, the ELCSIW post-fabrication tuning technique provides a simple and effective solution for achieving the desired response of an ELCSIW filter, regardless of the tolerances and variations in the materials properties. The technique is easy to implement and does not require any active circuit components, making it a cost-effective solution for manufacturers. This innovative tuning method expands the possibilities for implementing ELCSIW technology in various applications.

Chapter 4

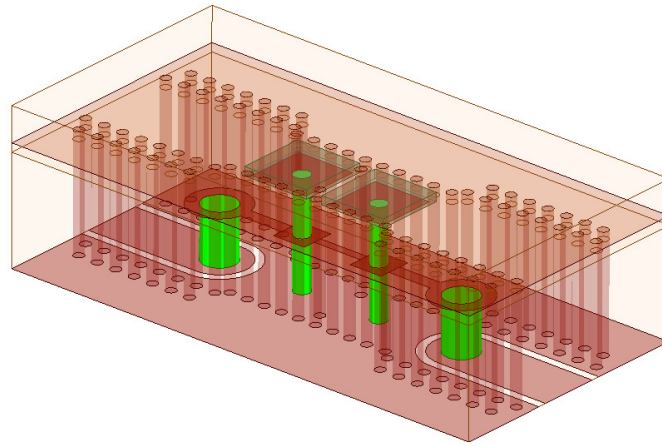
Ka-band Ultra-Miniaturized Substrate Integrated Waveguide Filters

This chapter presents the design and implementation of Ka-band embedded loaded coaxial substrate integrated waveguide filters to demonstrate the scalability of the ELCSIW technology to higher frequencies. An ELCSIW filter in Ka-band is first developed with the goal of achieving a miniaturization factor of 98.3 %, demonstrating the cutting edge of this miniaturization technology. Two second-order filters are designed to show the technology's potential to create transmission zeros and enhance the stopband rejection by using a mixed inter-resonator coupling.

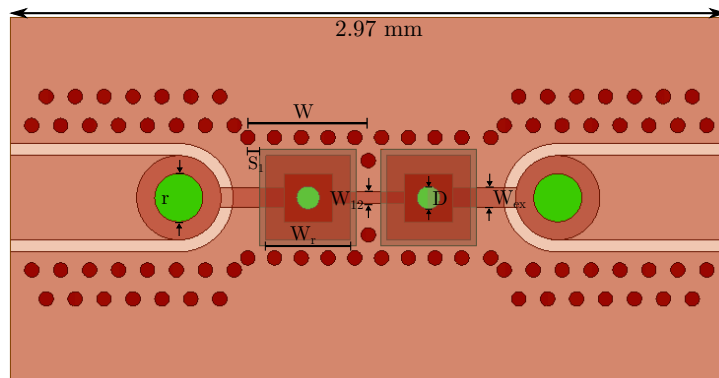
4.1 Ka-band ELCSIW Bandpass Filter Design

A Second-order Chebyshev ELCSIW bandpass filter is designed to demonstrate the technology's scalability to Ka-band frequencies. Figure 4.1 shows the overview of the Ka-band ELCSIW filter. The filter has 2 GHz of absolute bandwidth, which is equivalent to 6.6 % of fractional bandwidth, and an equi-ripple of 20 dB. The input/output feed lines consist of 50Ω grounded coplanar waveguide (GCPW) lines connected to tap strip lines through vertical transition vias. These tap strip lines are short-circuited to the resonator posts and allow for magnetic coupling to the cavity. The design procedure for a second-order ELCSIW filter

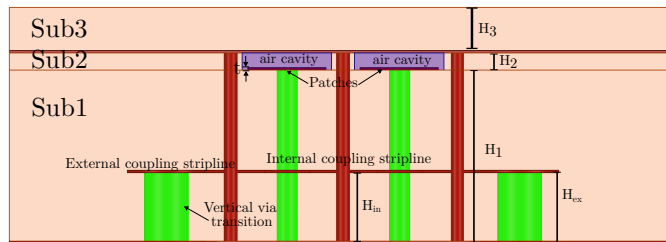
is demonstrated in section 2.3.



(a)



(b)



(c)

Figure 4.1: The structure of the Ka-band second-order ELCSIW bandpass filter, (a) 3D view, (b) top view, and (c) side view.

In Ka-band, the thickness of Sub1 (H_1) is reduced to mitigate the effect of the vertical via transition and increase its cut-off frequency to allow the filter to operate up to 30 GHz. Also, the Sub1 thickness has a significant impact on

the miniaturization factor. Figure 2.8 demonstrates the relationship between the Sub1 thickness and the miniaturization factor. Therefore, the total thickness of Sub1 is chosen to be 0.9652 mm (38 mils) to have a high miniaturization factor while mitigating the effect of the vertical via transition. To meet the required thickness, a Rogers 4003 dielectric material is chosen for Sub1 instead of Rogers TMM3 used for the L-band filter in Chapter 2, as it has a wide range of small standard thickness substrates. Rogers 4003 has a dielectric constant of 3.55 and a loss tangent of 0.0021. Sub1 is created by stacking three Rogers 4003 substrates (B1, B2, B3) and two SpeedWave prepreg layers for bonding, as shown in Figure 4.2. The thicknesses of substrates B1, B2, and B3 are 0.254 mm, 0.508 mm, and 0.1016 mm, respectively. The SpeedWave prepreg has a thickness of 0.0508 mm (2 mils) and a dielectric constant of 3.16. The external and internal coupling strip lines are etched on the bottom of substrate B2 at the height of 0.3048 mm. The air cavity is constructed in the Isola prepreg (Sub2) of thickness 0.06858 mm (2.7 mils). Rogers TMM3, with a thickness of 0.381 mm (15 mils), is then used to cover the air cavity. Because of its superior structural properties, TMM3 was used as a cover to minimize any bending into the air cavity during the lamination process.

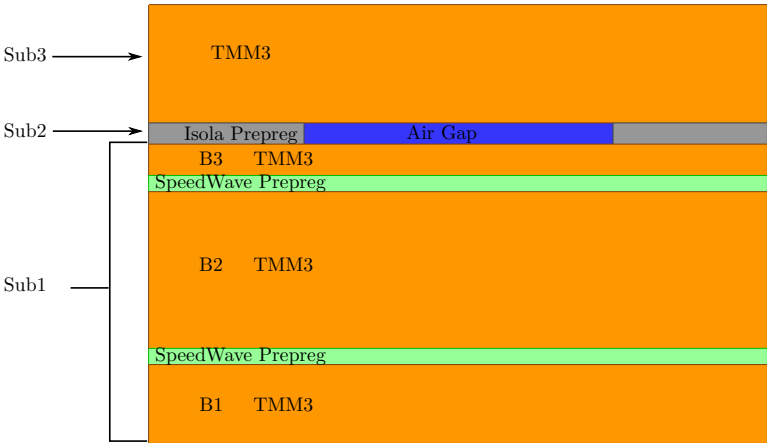


Figure 4.2: The substrate material stack-up for the Ka-band ELCSIW BPF.

4.1.1 Input/Output Feed Lines Design

50 Ω grounded coplanar waveguides are designed on the bottom of Sub1 as the input/output feeding lines and presented in Figure 4.3. The characteristic impedance of the transmission line is determined by the ratio of the width of the trace (W_c) to the gap (g) on a given substrate height and dielectric constant [4]. Two rows of fence shorted vias surround the coplanar waveguide to suppress any parasitic parallel plate modes. The distance of the fence vias from the copper trace (X_1) should be minimized to push the higher order modes to higher frequencies. Also, the spacing between the vias (p_1) should not exceed $\lambda/4$ at the highest frequency of operation to prevent any energy leaking into the side ground region structure beyond the fence vias. This energy leaking will generate higher order modes in the GCPW structure degrading the performance of the interconnect [84]. The design parameters of the coplanar waveguide are presented in Table 4.1. In Figure 4.4, the simulated S-parameters of the designed grounded coplanar waveguide are presented, showing low dispersions in the Ka-band frequency range.

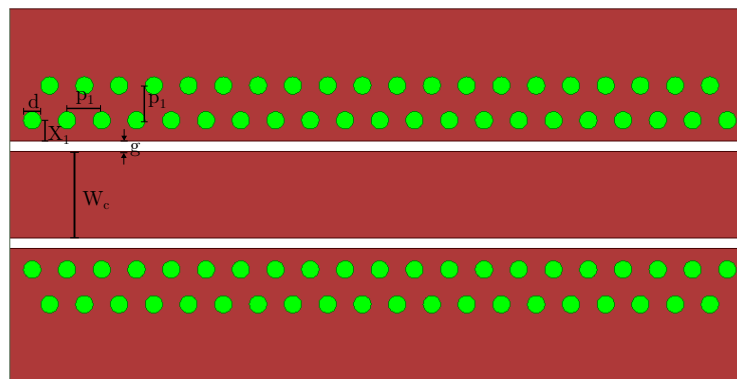


Figure 4.3: Top-view of the grounded coplanar waveguide trace with design parameters illustrations.

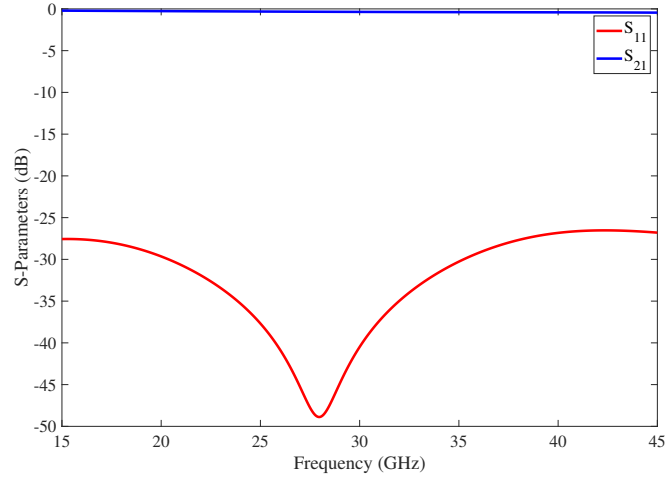


Figure 4.4: The simulated S-parameters of the designed grounded coplanar waveguide.

Next, the vertical via transition is appropriately designed to reduce its impact on the filter’s insertion loss at the Ka-band frequency range, and it’s presented in Figure 4.5. The signal propagates in the GCPW on the bottom substrate and then travels through a blind vertical via. A capture pad, with a diameter of 0.35 mm, is formed on the bottom of substrate B2 to connect the via to the external strip lines that are shorted to the cavity posts. A small capacitance is formed between the coplanar waveguide and the surrounding ground plane (C_1). The via length between the coplanar waveguide and the capture pad can be modeled as an inductance (L_1). There is also a small capacitance formed between the capture pad and the top copper layer (C_2). As discussed in detail

Table 4.1: Grounded coplanar waveguide design parameters. All dimensions are in mm.

Parameter	Value
GCPW substrate thickness	1.03378 (40.7 mils)
GCPW trace width (W_c)	0.35
GCPW gap (g)	0.05
Fence via diameter (d)	0.06
Fence via to trace spacing (X_1)	0.085
Fence via to via spacing (p_1)	0.12

in section 2.3.1, the vertical via transition, which is represented by two shunt capacitances (C_1 , C_2) and one inductance (L_1), behaves as a low pass filter. C_1 and L_1 can be determined using (2.24) and (2.25), respectively. The small capacitance that is formed between the capture pads and the top copper layer can be determined by

$$C_2 = \frac{\epsilon_0 \epsilon_r A}{d}, \quad (4.1)$$

where ϵ_0 is the permittivity of free space, ϵ_r is the dielectric constant of Sub1, A is the area of the capture pad, and d is the distance between the capture pads and the top copper layer. The equivalent lumped element circuit model of the vertical via transition is presented in Figure 4.6.

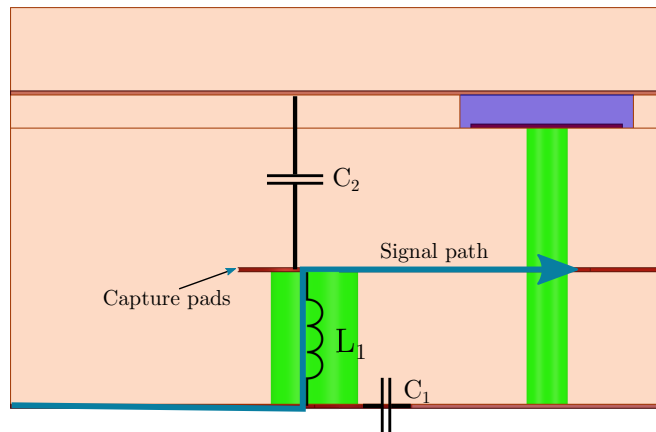


Figure 4.5: Overview of the Ka-band vertical via transition to illustrate the lumped elements affecting the signal path.

The impact of the vertical transition on the filter performance can be mitigated by appropriately tuning the dimensions of the capture pad diameter, the vertical via length, and the via diameter. The placement of the GCPW on the bottom side of the structure allows for a shorter via transition, creating a smaller inductance. This impact increases the cut-off frequency of the via transition. Also, the increase of vertical via diameter reduces the via inductance and increases the cut-off frequency. Moreover, the impact of the vertical via on the

filter can be minimized by reducing C_2 [51]. This can be obtained by receding the area of the capture pad.

The circuit model is simulated in AWR circuit solver, and vertical via dimensions are tuned. After tuning, the vertical via diameter is chosen to be 0.2 mm. The desired external coupling determines the length of the via, where the capture pad of the external strip line is placed and is initially set to 0.3048 mm. The capture pad diameter is chosen to be 0.35 mm. The calculated capacitance and inductance based on the design parameters are presented in Table 4.2. The simulated S-parameters of the vertical via circuit model using the calculated capacitance and inductance are shown in Figure 4.7. It can be seen that low loss is obtained across the frequency range of interest.

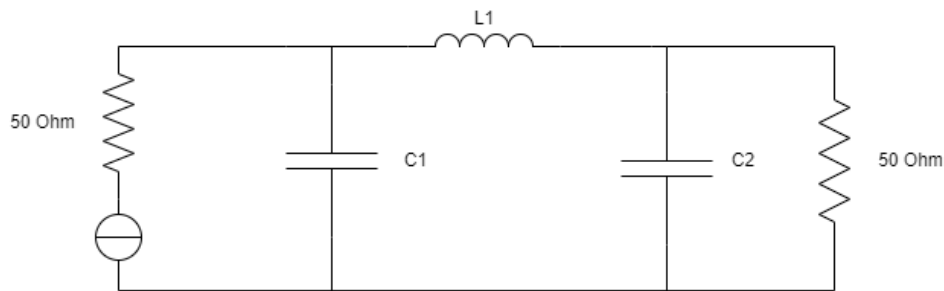


Figure 4.6: Ka-band vertical via transition equivalent lumped element circuit model.

Table 4.2: Calculated capacitance and inductance of the Ka-band vertical via transition lumped circuit model elements.

Lumped Element	Value
C_1	0.01207 pF
C_2	0.004082 pF
L_1	0.1712 nH

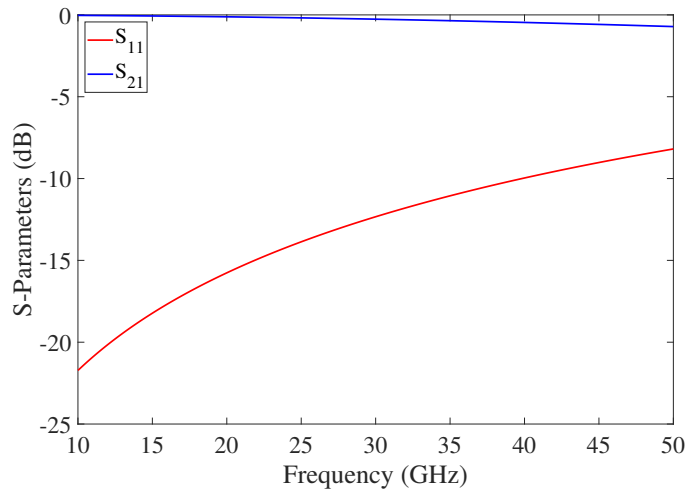


Figure 4.7: The simulated S-parameters of the Ka-band vertical transition via lumped element circuit model.

4.1.2 Simulation Results

The Ka-band Chebyshev ELCSIW second-order bandpass filter in Figure 4.1 is simulated using the full-wave HFSS solver. The filter is excited using two wave ports normalized to 50Ω placed at the edge of the coplanar waveguide substrate. The filter parameters' dimensions and thicknesses are listed in Table 4.3. To demonstrate the frequency scaling of the technology, the filter is designed at an arbitrary center frequency of 30 GHz with a bandwidth of 2 GHz. This Ka-band filter achieves 98.3 % miniaturization as compared to its substrate-integrated waveguide counterpart filters. The second-order filter's S-parameters are shown in Figure 4.8. The simulated insertion loss is 0.9 dB, and the return loss is greater than 20 dB. Moreover, the filter displays a wide spurious-free band greater than 30 GHz.

Table 4.3: Ka-band second-order Chebyshev ELCSIW bandpass filter design parameters. All dimensions are in mm.

Design Parameter	Value
Cavity length (W)	0.5
Patch width (W_r)	0.35
Post diameter (D)	0.095
Coplanar waveguide width (W_c)	0.35
Coplanar waveguide gap (g)	0.05
Vertical via transition diameter (D_v)	0.2
Air cavity to via spacing (S_1)	0.9
Outer via diameter (d)	0.06
Outer via spacing (p)	0.12
Bottom substrate thickness (H_1)	0.9652 (38 mils)
Isola prepreg thickness (H_2)	0.0685 (2.7 mils)
Top substrate thickness (H_3)	0.381 (15 mils)
External tap height (H_{ex})	0.3048 (12 mils)
Inter-resonator tap height (H_{in})	0.3048 (12 mils)
SpeedWave prepreg thickness	0.0508 (2 mil)
Copper clad thickness (t)	0.0175
Inter-resonator stripline width (W_{12})	0.05
External coupling stripline width (W_{ex})	0.08

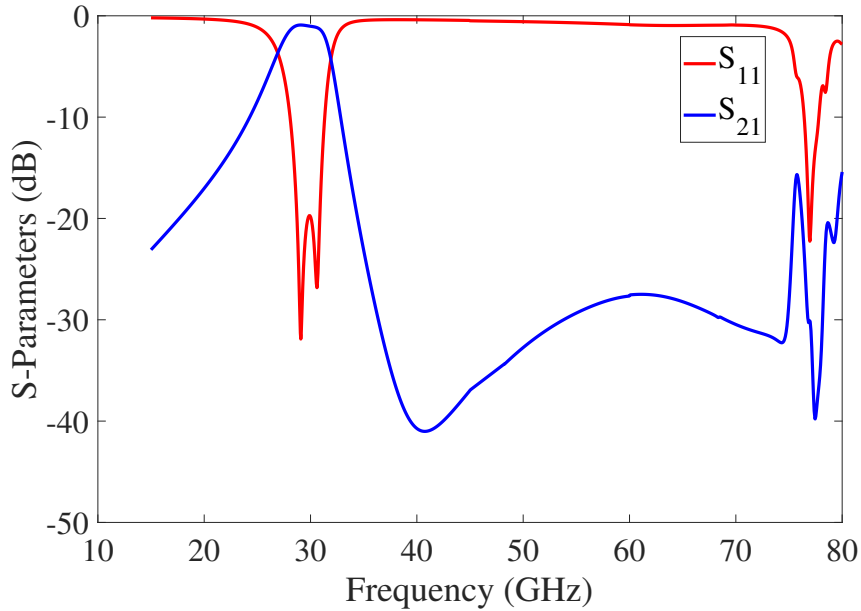


Figure 4.8: The simulated S-parameters of the Ka-band second-order ELCSIW bandpass filter.

4.2 Ka-band Mixed-Coupling ELCSIW Bandpass Filter Design

Second-order filters typically have a less sharp roll-off compared to higher-order filters, as observed in the performance of the Ka-band filter in Figure 4.8. This can result in unwanted signals leaking into the passband. Thus, two second-order ELCSIW bandpass filters in Ka-band with improved stopband rejection are developed. The stopband improvement is obtained by generating a transmission zero (TZ) in the stopband using a mixed-coupling mechanism as discussed in section 2.4. The ELCSIW unique structure allows two adjacent resonators to electrically couple by extending strip lines from the resonator patches and forming interdigital capacitor. The length and width of the strip lines and the spacing between them adjust the intensity of electric coupling. This extra coupling mechanism, in conjunction with direct tap magnetic coupling, provides a mixed coupling that can produce a transmission zero on either side of the passband based on which coupling is dominant. The first filter (case A) is designed to have a TZ in the upper stopband, whereas the second filter (case B) is designed to implement a TZ in the lower stopband. Both cases demonstrate the reconfigurability of the ELCSIW filter to have a TZ in an arbitrary location around the passband.

In Figure 4.9, the first mixed coupling second-order ELCSISW filter (case A) is presented with two extended strip lines from the resonator patches. The filter is designed based on the specifications and guidelines in section 4.1. The initial dimensions of the filter are listed in Table 4.3. The extended strip lines from the patches add extra capacitance and electrical coupling to the filter, and therefore, some of the designed parameters in Table 4.3 need slight modifications to achieve the desired specifications. These modifications to the design parameters are updated in the figure caption. The design procedure of the mixed coupling mechanism and the location of the TZ are discussed in section 2.4. Following

the abovementioned guidelines, the filter is implemented and simulated in the full-wave HFSS solver, and the S-parameters are shown in Figure 4.10. The simulated insertion loss is 0.9 dB, and the return loss is greater than 20 dB. The figure shows a TZ realized at 37 GHz to improve the stopband rejection.

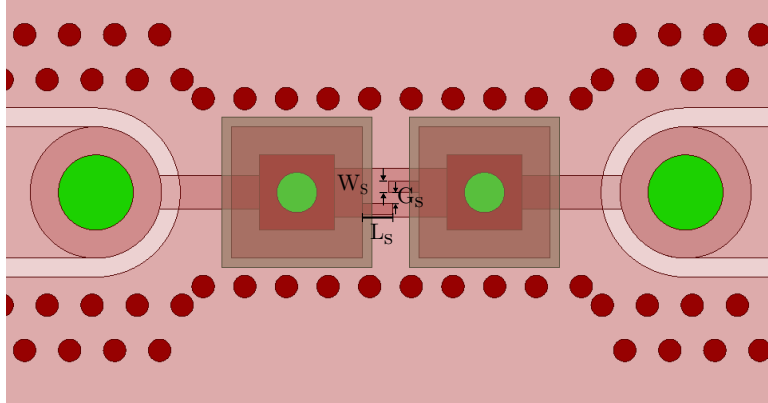


Figure 4.9: Design illustration of the second-order ELCSIW filter (case A) with mixed magnetic and electric coupling mechanisms. ($L_s = 0.08$ mm, $W_s = 0.03$ mm, $G_s = 0.03$ mm, $D = 0.107$ mm, $W_{12} = 0.13$ mm, $W_{ex} = 0.09$ mm).

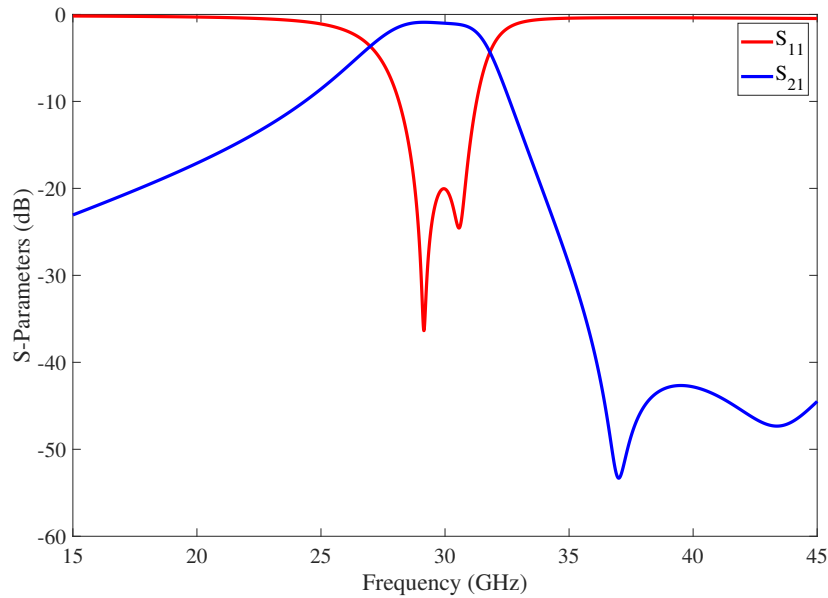


Figure 4.10: The simulated S-parameters of the Ka-band second-order ELCSIW filter (case A).

The mixed coupling second-order ELCSISW filter (case B) is presented in Figure 4.11 with three extended strip lines from each resonator patch. Similarly, the filter is designed based on the specifications and guidelines in section 4.1. The initial dimensions of the filter are listed in Table 4.3, and slight modifications on these design parameters are provided in the figure caption. The filter is implemented and simulated in the full-wave HFSS solver, and the S-parameters are shown in Figure 4.12. The simulated insertion loss is 1.1 dB, and the return loss is greater than 20 dB. Additional loss is noticeably degrading the passband performance. The additional loss is caused by the strong electric field coupling between the extended strip lines. Figure 4.12 shows a TZ realized at 23 GHz, which significantly improves the lower stopband rejection as compared to the filter performance in Figure 4.8.

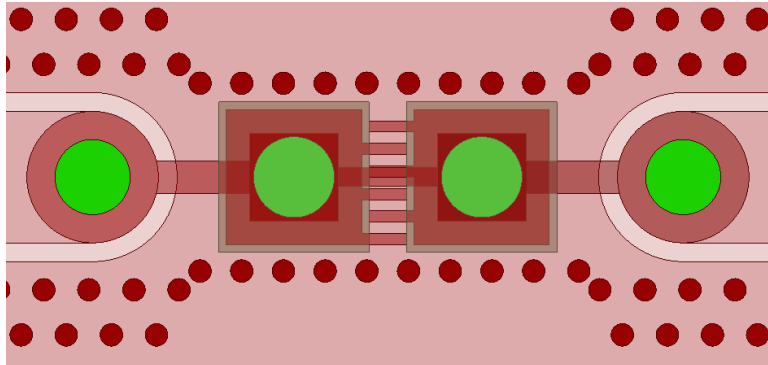


Figure 4.11: Design illustration of the Ka-band second-order ELCSISW filter (case B) with mixed magnetic and electric coupling mechanisms. ($L_s = 0.12$ mm, $W_s = 0.03$ mm, $G_s = 0.03$ mm, $D = 0.215$ mm, $W_{12} = 0.05$ mm, $W_{ex} = 0.087$ mm, $H_{in} = 0.1016$ mm).

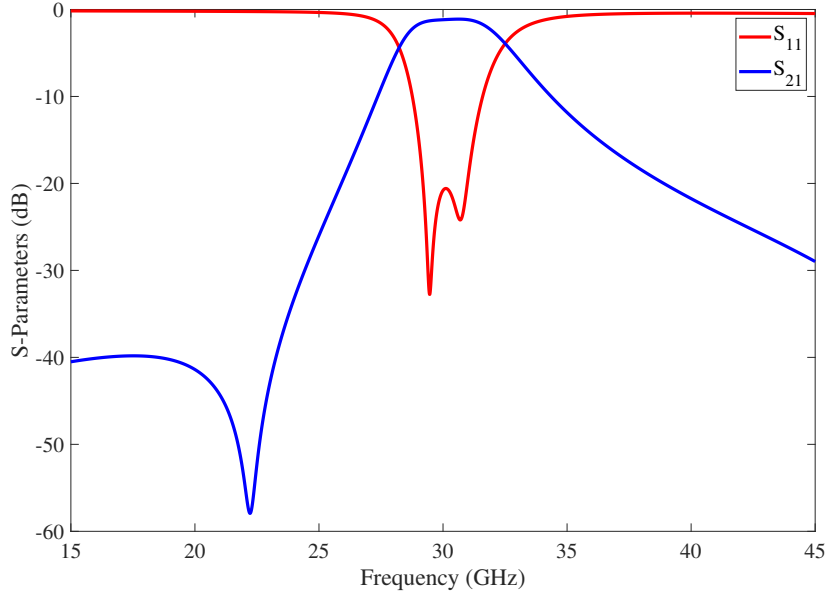


Figure 4.12: The simulated S-parameters of the Ka-band second-order ELCSIW filter (case B).

The ELCSIW technology is a cutting-edge development in the field of substrate integrated waveguide compact filter technology. This technology is a promising new technology for ultra-miniaturized SIW filters. The ELCSIW technology has been demonstrated in Ka-band frequencies showing 98 % miniaturization factor, excellent insertion loss of less than 1.1 dB, and improved stopband rejection using full-wave simulations. This shows the capability of ELCSIW technology to scale to higher frequencies at a compact size and low loss. This technology has the potential to advance future communication and radar systems; however, several challenges need to be overcome in order to implement it in a standard PCB process.

One of the challenges is the size of the smallest feature in the design, which must be chosen according to the fabrication capability. For instance, the Protolaser U4 has the ability to fabricate strip lines of width $30 \mu\text{m}$ using $20 \mu\text{m}$ focused laser beam diameter with a $1.2 \mu\text{m}$ resolution. This can limit ELCSIW implementation in PCB technology in frequencies higher than Ka-band. However,

this technology can be explored for applicability to other fabrication processes, such as semiconductor technologies, to create even smaller features. Another challenge is the vertical transition low pass filter effect. This effect limits the substrate thickness selection as a thicker substrate lowers the low pass filter cutoff frequency. Other external coupling mechanisms, such as CPW to SIW transition coupling and slots coupling, can be investigated as alternatives to the vertical via transition.

In summary, the ELCSIW technology offers a compact and low-loss solution for filters in wireless communications and radar systems. Although some challenges need to be overcome, further research and development in this field will help fully realize this technology's potential and provide better solutions for future communication and radar systems.

Chapter 5

Summary and Future Work

5.1 Summary of Work

This research is focused on advancing the field of ultra-miniaturized filters for use in the next generation of wireless communications and radar systems. These systems have strict RF front-ends requirements, including compactness, lightweight design, high power capability, and low loss. In order to meet these demands, ultra-miniaturized embedded loaded coaxial substrate integrated waveguide filters are developed and implemented.

First, a comprehensive modeling and analysis of the proposed ELCSIW structure are presented. Integrating a highly loaded air-filled parallel plate capacitor into an ELCSIW resonator is key to achieve a high miniaturization factor with a high-quality factor. Detailed step-by-step materials selection and fabrication guidelines in standard PCB technology are provided. An ELCSIW resonator is simulated at 1.1 GHz, obtaining a 99 % miniaturization factor and an unload quality factor of 480. Utilizing the ELCSIW resonator, a second-order ELCSIW bandpass filter is designed and implemented at 1.1 GHz. The simulated filter exhibit a low insertion loss of 0.26 dB at 6.3 % of fractional bandwidth. Moreover, the proposed filter demonstrates a spurious free stopband more than $7 \times f_r$, highlighting another technology advantage. The power handling capability of the ELCSIW filter is investigated in this work. A power handling capability

prediction method is shown, and it predicted that an ELCSIW filter is capable of handling up to 113 Watts of power. A comparison between the ELCSIW filter and the current state of miniaturized substrate-integrated filters is presented. The ELCSIW filter demonstrates superiority in compactness, quality factor, and stopband rejection compared to the state-of-the-art filter technologies in the literature.

Another emphasis of this dissertation is enhancing the stopband rejection of a second-order ELCSIW filter. Implementing two controlled electric and magnetic mixed inter-resonator coupling mechanisms enabled the realization of a transmission zero on either side of the passband of the second-order ELCSIW filter. The transmission zero will occur at the lower side of the passband when the electric cross-coupling dominates and vice versa at the upper side when the magnetic cross-coupling dominates. The arbitrary location of the transmission zero is determined by the intensity of each coupling mechanism. The unique structure of the proposed ELCSIW allows two coupling mechanisms to be implemented with minimal additional fabrication cost. The configuration and the design guidelines of the mixed-coupled ELCSIW filters are presented. Two second-order mixed-coupled ELCSIW filters with two different transmission zero locations are developed and simulated, showing improvements in the stopband rejection.

Next, a novel post-fabrication frequency tuning mechanism for the ELCSIW filter is developed. The tolerances and variations in thicknesses and material properties of prepreg and dielectric substrates can affect the resonant frequency of the fabricated ELCSIW filters. Thus, additional capacitive loading strip lines are integrated into the cavity in the design to compensate for the frequency variation. By connecting or disconnecting the loading striplines, the cavity's total inductance, and capacitance can be adjusted, allowing to tune the resonant frequency. The circuit model and the working mechanism of the tuning circuit are

explained. Two scenarios of mistuned ELCSIW filters are presented to demonstrate the proposed method's effectiveness. Using the proposed frequency tuning method, the resonant frequencies of the mistuned filters are accurately tuned to their originally designed frequency.

Finally, the scaling capabilities of the ELCSIW technology to high frequency are investigated. Material selections and design guidelines are provided and applied to design a second-order ELCSIW filter at 30 GHz. The simulated filter showed an insertion loss of less than 0.91 dB and a return loss greater than 20 dB. The filter area is 0.56 mm \times 1.12 mm with more than 98.3 % miniaturization factor. In addition, two second-order mixed-coupled ELCSIW filters are designed and simulated at 30 GHz to illustrate the advantage of applying mixed-coupling to increase stopband rejection by adding a transmission zero. Despite the challenges, such as fabrication limitation and external coupling degradation effect, further research and development in this technology will help fully realize its potential and provide better solutions beyond Ka-band frequencies.

Overall, the work presented in this dissertation provides state-of-the-art ultra-miniaturized high quality factor substrate integrated waveguide filters that have the potential to be integrated into the next generation of wireless communications and radar systems.

5.2 Contributions

This dissertation has provided contributions to the field of SIW miniaturization techniques and post-fabrication tuning. The work contributions are summarized as follows

- Accurate modeling and characterization of ELCSIW cavity resonators.
- Development and implementation of ELCSIW cavity resonator achieving

miniaturization factor of 99 % and quality factor of 480.

- Provide design guidelines to fabricate multi-layer ELCSIW cavity with micrometer scale air cavity.
- Design and fabrication of ultra-miniaturized bandpass filter with an insertion loss of less than 0.54 dB.
- Development of an ultra-miniaturized bandpass filter with a theoretical power handling capability prediction of more than 113 W.
- Design and development of an ultra-miniaturized inline mixed-coupled bandpass filter with dynamic transmission zeros relocation.
- Design and development of a novel post-fabrication frequency tuning for ELCSIW filters.
- Design and demonstration of ELCSIW filter at Ka-band frequency.
- Design and development of an ultra-miniaturized inline mixed-coupled bandpass filter with dynamic transmission zeros relocation at Ka-band.

5.3 Future Work

In this dissertation, ultra-miniaturized embedded loaded coaxial substrate integrated waveguide filters and resonators are presented. As shown in Chapter 3, the resonant frequency of the ELCSIW resonator is sensitive to the capacitive air gap constructed by the Isola prepreg. The Isola prepreg has its manufacturing tolerance, and in addition, its thickness may get reduced under the high pressure applied during the lamination process. Three micrometers tolerance in the thickness of the Isola prepreg can lead to a 5 % shift in the resonant frequency. Also, the lamination pressure can cause thickness reduction in the Isola

prepreg. Typically, the lamination process requires an experimental characterization of bonding multiple layers to find the recipe that ensures excellent adhesion while obtaining the required air gap thickness. Despite the characterizing of the lamination process, there will be variations in the Isola prepreg thickness. The typical setup for bonding two dielectric substrates and a prepreg is demonstrated in Figure 5.1. An accurate Isola prepreg thickness can be obtained by inserting a copper sheet with known thickness into the stack of the bonding layers. The metal sheet acts as a stopper when the prepreg thickness is reduced under the high-pressing lamination process, as shown in Figure 5.2. In other words, the metal sheet stopper thickness is chosen to be smaller than the prepreg. Then, when the pressing is applied, the metal stopper will prevent the prepreg from shrinking beyond the thickness determined by the stopper.

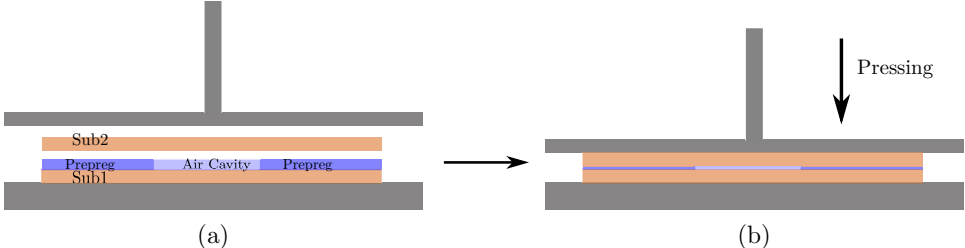


Figure 5.1: The typical lamination setup for two substrates and a prepreg illustrating the prepreg thickness reduction after pressing.

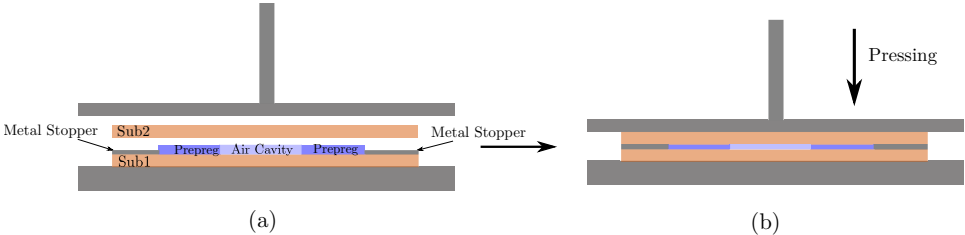


Figure 5.2: The proposed lamination setup for two substrates and a prepreg showing the benefit of the metal stopper in controlling the prepreg final thickness.

In Chapter 3, a post-fabrication frequency tuning method for ELCSIW filters is presented for the first time. This method allows a wide tuning range for the

resonant frequency of the ELCSIW resonator by disconnecting capacitive tuning strip lines embedded into the cavity. The capacitance of the tuning strip line varies based on its length, width, and distance from the patch. This work can be extended to a tunable ELCSIW filter. Using switch technologies such as pin diodes or MEMS, an ELCSIW resonator can be developed to have a range of tunable frequencies controlled by DC bias switches. The proposed overview of the tunable filter is presented in Figure 5.3. Each switch can have a separate DC bias. The number of tuning strip lines can be increased to more than eight to increase the tuning range and flexibility of the tuning step size of the resonant frequency.

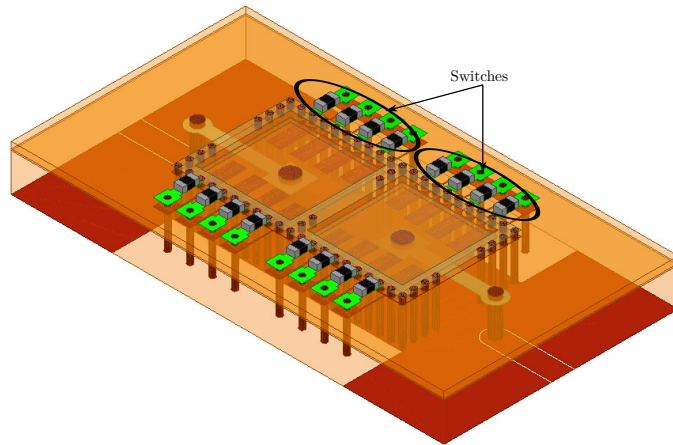


Figure 5.3: The proposed overview of the tunable ELCSIW filter using switch technology.

In Chapter 2, a mixed-coupling mechanism is implemented in the ELCSIW filter to realize a transmission zero in the stopband to improve its rejection characteristics. This method can be utilized in developing a new configuration of quad-mode ELCSIW cavity resonators. The ELCSIW quad-mode has four conductive posts and four patches within a single cavity, as shown in Figure 5.4. Four different modes are generated in the cavity and coupled with each other. Figure 5.5 shows the simulated vector plot of the electric-field distribution of the

resonant modes. The magnetic coupling is determined by the spacing between the posts and the size of the posts, whereas the electric coupling is determined by the inter-digital strip line length. This quad-mode configuration allows for four different cross-coupling paths, which can generate four transmission zeros [85]. A transmission zero will occur at the lower side of the passband when electric cross-coupling dominates and vice versa at the upper side when magnetic cross-coupling dominates, as demonstrated in section 2.4. This new configuration of quad-mode in ELCSIW technology enables to have an ultra-miniaturized filter with multiple transmission zeros to suppress interference and higher-order modes and improve the overall stopband rejection.

Further research and development in the higher-order, multi-modes, and tunable ELCSIW filters can expand the feasibility of integrating this technology in different applications and systems, unlocking the full potential of the technology.

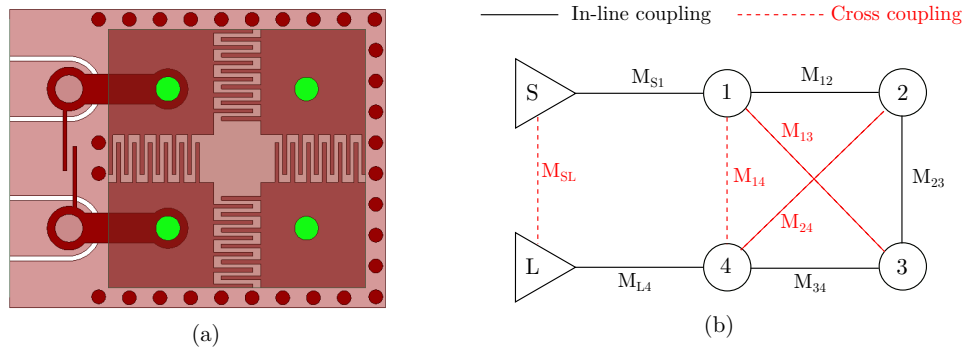


Figure 5.4: (a) Design layout of the proposed quad-mode ELCSIW cavity resonator, and (b) coupling scheme of the proposed quad-mode ELCSIW filter.

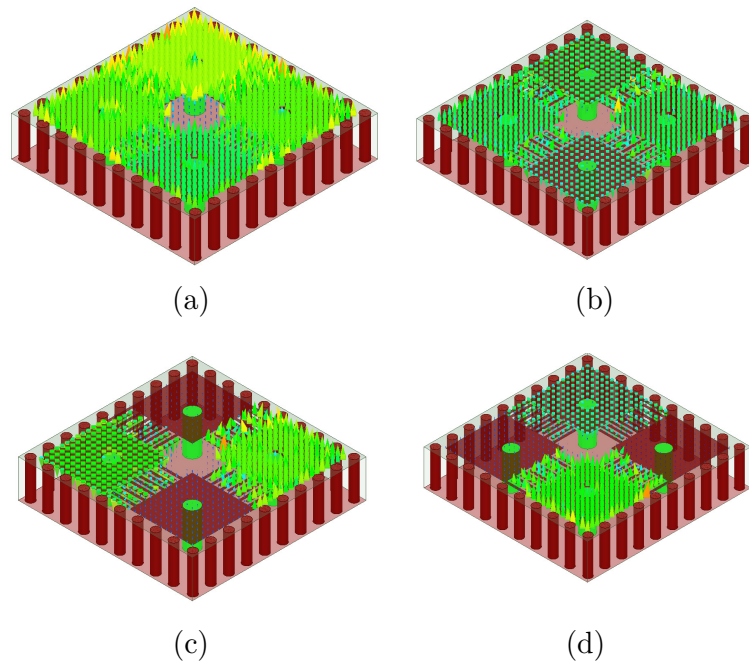


Figure 5.5: Vector plot of the simulated electric field distribution of the proposed quad-mode ELCSIW cavity resonator, (a) fundamental mode, (b) differential mode, (c) and (d) pair of orthogonal degenerate modes.

Bibliography

- [1] Mohammad Mozaffari, Walid Saad, Mehdi Bennis, Young-Han Nam, and Mérouane Debbah. A tutorial on uavs for wireless networks: Applications, challenges, and open problems. *IEEE Communications Surveys Tutorials*, 21(3):2334–2360, 2019.
- [2] Wahab Ali Gulzar Khawaja, Martins Ezuma, Vasili Semkin, Fatih Erden, Ozgur Ozdemir, and Ismail Guvenc. A survey on detection, tracking, and classification of aerial threats using radars and communications systems, 11 2022.
- [3] C. Sempere Chaves, R. H. Geschke, M. Shargorodskyy, R. Brauns, R. Herschel, and C. Krebs. Polarimetric uav-deployed fmcw radar for buried people detection in rescue scenarios. In *2021 18th European Radar Conference (EuRAD)*, pages 5–8, 2022.
- [4] D.M. Pozar. *Microwave Engineering*. Wiley, 2012.
- [5] Swamy M. N. S. Du, Ke-Lin. *Wireless Communication Systems From RF Subsystems to 4G Enabling Technologies*. Cambridge University Press, 2010.
- [6] Inder Bahl, Maurizio Bozzi, and Ramesh Garg. *Microstrip Lines and Slotlines, Third Edition*. Artech, 2013.
- [7] Chi Wang and Krawthar A. Zaki. Dielectric resonators and filters. *IEEE Microwave Magazine*, 8(5):115–127, 2007.

- [8] M. Bozzi, A. Georgiadis, and K. Wu. Review of substrate-integrated waveguide circuits and antennas. *IEE proceedings. Microwaves, antennas and propagation.*, 5(8):909–920, 06 2011.
- [9] Xiao-Ping Chen and Ke Wu. Substrate integrated waveguide filter: Basic design rules and fundamental structure features. *IEEE Microwave Magazine*, 15(5):108–116, 2014.
- [10] K. Wu. Integration and interconnect techniques of planar and non-planar structures for microwave and millimeter-wave circuits - current status and future trend. *APMC 2001. 2001 Asia-Pacific Microwave Conference*, 2:411–416 vol.2, 2001.
- [11] R. Garg, P. Bhartia, I. Bahl, and A. Ittipiboon. *Microstrip Antenna Design Handbook*. Artech House, 2001.
- [12] H. Uchimura, T. Takenoshita, and M. Fujii. Development of a "laminated waveguide". *IEEE Transactions on Microwave Theory and Techniques*, 46(12):2438–2443, 1998.
- [13] D. Deslandes and K. Wu. Integrated microstrip and rectangular waveguide in planar form. *IEEE Microwave and Wireless Components Letters*, 11(2):68–70, 2001.
- [14] Ke Wu, Maurizio Bozzi, and Nelson J. G. Fonseca. Substrate integrated transmission lines: Review and applications. *IEEE Journal of Microwaves*, 1(1):345–363, 2021.
- [15] Dominic Deslandes and Ke Wu. Single-substrate integration technique of planar circuits and waveguide filters. *IEEE Transactions on Microwave Theory and Techniques*, 51(2 I):593–596, 2003.

- [16] Mostafa Abdolhamidi and Mahmoud Shahabadi. X-band substrate integrated waveguide amplifier. *IEEE Microwave and Wireless Components Letters*, 18(12):815–817, 2008.
- [17] Zhebin Wang and Chan-Wang Park. Novel substrate integrated waveguide (siw)-based power amplifier using siw-based filter to suppress up to the fourth harmonic. In *2012 Asia Pacific Microwave Conference Proceedings*, pages 830–832, 2012.
- [18] Rui Sen Chen, Sai-Wai Wong, Lei Zhu, and Qing-Xin Chu. Wideband bandpass filter using u-slotted substrate integrated waveguide (siw) cavities. *IEEE Microwave and Wireless Components Letters*, 25(1):1–3, 2015.
- [19] Min-Hua Ho and Kun-Hua Tang. Miniaturized siw cavity tri-band filter design. *IEEE Microwave and Wireless Components Letters*, 30(6):589–592, 2020.
- [20] Y. Cassivi and K. Wu. Low cost microwave oscillator using substrate integrated waveguide cavity. *IEEE Microwave and Wireless Components Letters*, 13(2):48–50, 2003.
- [21] Weichen Huang, Jianyi Zhou, and Peng Chen. An x-band low phase noise free-running oscillator using substrate integrated waveguide dual-mode bandpass filter with circular cavity. *IEEE Microwave and Wireless Components Letters*, 25(1):40–42, 2015.
- [22] Maurizio Bozzi, Feng Xu, Dominic Deslandes, and Ke Wu. Modeling and design considerations for substrate integrated waveguide circuits and components. *8th International Conference on Telecommunications in Modern Satellite, Cable and Broadcasting Services, TELSIKS 2007, Proceedings of Papers*, 2007.

- [23] A U Bhohe and T P Cencich. Investigations on the propagation characteristics of the substrate integrated waveguide based on the method of lines. pages 527–533, 2005.
- [24] D. Deslandes and Ke Wu. Accurate modeling, wave mechanisms, and design considerations of a substrate integrated waveguide. *IEEE Transactions on Microwave Theory and Techniques*, 54(6):2516–2526, 2006.
- [25] Maurizio Bozzi, Marco Pasian, and Luca Perregrini. Advanced modeling and design of substrate integrated waveguide components. In *2014 IEEE International Wireless Symposium (IWS 2014)*, pages 1–4, 2014.
- [26] Robert E. Collin. *Waveguides and Cavities*, pages 329–410. 1991.
- [27] N. Grigoropoulos and P.R. Young. Compact folded waveguides. In *34th European Microwave Conference, 2004.*, volume 2, pages 973–976, 2004.
- [28] Wenquan Che, Liang Geng, Kuan Deng, and Y. Leonard Chow. Analysis and experiments of compact folded substrate-integrated waveguide. *IEEE Transactions on Microwave Theory and Techniques*, 56(1):88–93, 2008.
- [29] Hung-Yi Chien, Tze-Min Shen, Ting-Yi Huang, Wei-Hsin Wang, and Ruey-Beei Wu. Miniaturized bandpass filters with double-folded substrate integrated waveguide resonators in ltcc. *IEEE Transactions on Microwave Theory and Techniques*, 57(7):1774–1782, 2009.
- [30] C. A. Zhang, Y. J. Cheng* and Y. Fan. Quadri-folded substrate integrated waveguide cavity and its miniaturized bandpass filter applications. . *Progress In Electromagnetics Research*, 23(May):1–14, 2011.

- [31] Alejandro Niembro-Martín, Victoria Nasserddine, Emmanuel Pistono, Hamza Issa, Anne-Laure Franc, Tan-Phu Vuong, and Philippe Ferrari. Slow-wave substrate integrated waveguide. *IEEE Transactions on Microwave Theory and Techniques*, 62(8):1625–1633, 2014.
- [32] Matthieu Bertrand, Zhanhao Liu, Emmanuel Pistono, Darine Kaddour, and Philippe Ferrari. A compact slow-wave substrate integrated waveguide cavity filter. In *2015 IEEE MTT-S International Microwave Symposium*, pages 1–3, 2015.
- [33] Matthieu Bertrand, Emmanuel Pistono, Darine Kaddour, Vincent Puyal, and Philippe Ferrari. A filter synthesis procedure for slow wave substrate-integrated waveguide based on a distribution of blind via holes. *IEEE Transactions on Microwave Theory and Techniques*, 66(6):3019–3027, 2018.
- [34] Yuanqing Wang, Wei Hong, Yuandan Dong, Bing Liu, Hong Jun Tang, Jixin Chen, Xiaoxin Yin, and Ke Wu. Half mode substrate integrated waveguide (hmsiw) bandpass filter. *IEEE Microwave and Wireless Components Letters*, 17(4):265–267, 2007.
- [35] Stefano Moscato, Cristiano Tomassoni, Maurizio Bozzi, and Luca Perregrini. Quarter-mode cavity filters in substrate integrated waveguide technology. *IEEE Transactions on Microwave Theory and Techniques*, 64(8):2538–2547, 2016.
- [36] Peng Li, Hui Chu, and Ru-Shan Chen. Design of compact bandpass filters using quarter-mode and eighth-mode siw cavities. *IEEE Transactions on Components, Packaging and Manufacturing Technology*, 7(6):956–963, 2017.
- [37] Ya Na Yang, Guo Hui Li, Li Sun, Wei Yang, and Xue Xia Yang. Design of compact Bandpass filters using sixteenth mode and thirty-second mode

- SIW cavities. *Progress in Electromagnetics Research Letters*, 75(April):61–66, 2018.
- [38] Thomas R. Jones and Mojgan Daneshmand. Miniaturized Folded Ridged Half-Mode and Quarter-Mode Substrate Integrated Waveguides for Filter Design. *IEEE Transactions on Microwave Theory and Techniques*, 67(8):3414–3426, 2019.
- [39] T. Itoh Y. Dong. Substrate integrated waveguide negative-order resonances and their applications. *IET Microwaves, Antennas and Propagation*, 4(6):1081–1091(10), 2010.
- [40] Tao Yang, Pei-Ling Chi, Ruimin Xu, and Weigan Lin. Folded substrate integrated waveguide based composite right/left-handed transmission line and its application to partial h -plane filters. *IEEE Transactions on Microwave Theory and Techniques*, 61(2):789–799, 2013.
- [41] Xinlei Zhang Bo Zhou Shanwen Hu, Yiting Gao. Design of a compact 5.7-5.9 ghz filter based on crlh resonator units. *Progress In Electromagnetics Research Letters*, 89(4):141–149, 2020.
- [42] Jorge D. Martínez, Máriam Taroncher, and Vicente E. Boria. Capacitively loaded resonator for compact substrate integrated waveguide filters. *The 40th European Microwave Conference*, pages 192–195, 2010.
- [43] Stefano Sirci, Jorge D. Martínez, and Vicente E. Boria. A novel magnetic coupling for miniaturized bandpass filters in embedded coaxial SIW. *Applied Sciences*, 9(3), 2019.
- [44] Min Hua Ho, Jen Chih Li, and Yi Cheng Chen. Miniaturized SIW Cavity Resonator and Its Application in Filter Design. *IEEE Microwave and Wireless Components Letters*, 28(8):651–653, 2018.

- [45] Jorge D. Martinez, Stefano Sirci, Mriam Taroncher, and Vicente E. Boria. Compact CPW-fed combline filter in substrate integrated waveguide technology. *IEEE Microwave and Wireless Components Letters*, 22(1):7–9, 2012.
- [46] Harlan B. Palmer. The Capacitance of a Parallel-Plate Capacitor by the Schwartz-Christoffel Transformation. *Transactions of the American Institute of Electrical Engineers*, 56(3):363–366, 2009.
- [47] H.J. Riblet. An accurate approximation of the impedance of a circular cylinder concentric with an external square tube. *IEEE Transactions on Microwave Theory and Techniques*, 31(10):841–844, 1983.
- [48] Qinghua Lai, Christophe Fumeaux, Wei Hong, and Rüdiger Vahldieck. Characterization of the propagation properties of the half-mode substrate integrated waveguide. *IEEE Transactions on Microwave Theory and Techniques*, 57(8):1996–2004, 2009.
- [49] Saminda Dharmarathna, Sean Fleuriel, Eric Kil, Charles Bae, Leslie Kim, and Derek Hwang. Acid Copper Electroplating Processes With Excellent V-Pit Resistance for Flash Etching.
- [50] JIA-SHENG HONG. *Microstrip Filters for RF/Microwave Applications*. John Wiley Sons, Ltd, 2001.
- [51] Altera Corporation. Via Optimization Techniques for High-Speed Channel Designs - N529. (May):1–19, 2008. Available at <https://www.intel.com/content/dam/www/programmable/us/en/pdfs/literature/an/an529>. Online; accessed 01-Jan-2023.

- [52] L. Young G. Mattaei and E. M. T. Jones. *Microwave Filters, Impedance-Matching Networks, and Coupling Structures*. Artech House,, Norwood, MA, 1980.
- [53] Rogers Corporation. Speedwave™ 300p prepreg fabrication guidelines. 2023. Available at <https://www.rogerscorp.com/advanced-electronics-solutions/prepregs-and-bondplys/speedwave-300p-prepreg>. Online; accessed 01-Jan-2023.
- [54] C. A. Zhang, Y. J. Cheng and Y. Fan. Quadri-folded Substrate Integrated Waveguide Cavity and its Miniaturized Bandpass Filter Applications. *Progress In Electromagnetics Research*, 23(May):1–14, 2011.
- [55] Seymour B. Cohn. Dissipation loss in multiple-coupled-resonator filters. *Proceedings of the IRE*, 47(8):1342–1348, 1959.
- [56] Fang Zhu, Wei Hong, Ji-Xin Chen, and Ke Wu. Cross-coupled substrate integrated waveguide filters with improved stopband performance. *IEEE Microwave and Wireless Components Letters*, 22(12):633–635, 2012.
- [57] Xiao-Ping Chen and Ke Wu. Substrate Integrated Waveguide Cross-Coupled Filter With Negative Coupling Structure. *IEEE Transactions on Microwave Theory and Techniques*, (1):142–149, jan.
- [58] Ching-Ku Liao and Chi-Yang Chang. Design of microstrip quadruplet filters with source-load coupling. *IEEE Transactions on Microwave Theory and Techniques*, 53(7):2302–2308, 2005.
- [59] Kaixue Ma, Jian-Guo Ma, Kiat Seng Yeo, and Manh Anh Do. A compact size coupling controllable filter with separate electric and magnetic coupling paths. *IEEE Transactions on Microwave Theory and Techniques*, 54(3):1113–1119, 2006.

- [60] Huan Wang and Qing Xin Chu. An inline coaxial quasi-elliptic filter with controllable mixed electric and magnetic coupling. *IEEE Transactions on Microwave Theory and Techniques*, 57(1):667–673, 2009.
- [61] Ming Yu. Power-handling capability for RF filters. *IEEE Microwave Magazine*, 8(5):88–97, 2007.
- [62] S. Saeedi, J. Lee, and H. Sigmarsson. Prediction of power handling in tunable, high-q, substrate-integrated, evanescent-mode cavity bandpass filters. *Electronics Letters*, 52(10):846–848, 2016.
- [63] Kenle Chen, Abbas Semnani, and Dimitrios Peroulis. High-power microwave gas discharge in high-q evanescent-mode cavity resonators and its instantaneous/long-term effects. In *2013 IEEE MTT-S International Microwave Symposium Digest (MTT)*, pages 1–4, 2013.
- [64] T. Olsson, U. Jordan, D. S. Dorozhkina, V. Semenov, D. Anderson, M. Lisak, J. Puech, I. Nefedov, and I. Shereshevskii. Microwave breakdown in rf devices containing sharp corners. *2006 IEEE MTT-S International Microwave Symposium Digest*, pages 1233–1236, 2006.
- [65] Rogers Corporation. Tmm thermoset microwave materials datasheet. 2023. Available at <https://www.rogerscorp.com/advanced-electronics-solutions/tmm-laminates/tmm-3-laminates>. Online; accessed 01-Jan-2023.
- [66] Rogers Corporation. Speedwave™ 300p prepreg datasheet. 2023. Available at <https://www.rogerscorp.com/advanced-electronics-solutions/prepregs-and-bondplys/speedwave-300p-prepreg>. Online; accessed 01-Jan-2023.

- [67] Vahid Miraftab and Raafat R. Mansour. Fully automated rf/microwave filter tuning by extracting human experience using fuzzy controllers. *IEEE Transactions on Circuits and Systems I: Regular Papers*, 55(5):1357–1367, 2008.
- [68] Raafat R. Mansour, Fengxi Huang, Siamak Fouladi, Winter Dong Yan, and Mitra Nasr. High- q tunable filters: Challenges and potential. *IEEE Microwave Magazine*, 15(5):70–82, 2014.
- [69] Gowrish Basavarajappa and Raafat R. Mansour. Design methodology of a high- q tunable coaxial filter and diplexer. *IEEE Transactions on Microwave Theory and Techniques*, 67(12):5005–5015, 2019.
- [70] Rui Zhang and Raafat R. Mansour. Low-cost dielectric-resonator filters with improved spurious performance. *IEEE Transactions on Microwave Theory and Techniques*, 55(10):2168–2175, 2007.
- [71] I.C. Hunter and J.D. Rhodes. Electronically tunable microwave bandpass filters. *IEEE Transactions on Microwave Theory and Techniques*, 30(9):1354–1360, 1982.
- [72] Jia Ni and Jiasheng Hong. Compact varactor-tuned microstrip high-pass filter with a quasi-elliptic function response. *IEEE Transactions on Microwave Theory and Techniques*, 61(11):3853–3859, 2013.
- [73] Xiaoxiao Chen, Yongle Wu, Yuhao Yang, and Weimin Wang. Simple coupled-line tunable bandpass filter with wide tuning range. *IEEE Access*, 8:82286–82293, 2020.
- [74] Amjad Iqbal, Jun Jiat Tiang, Ching Kwang Lee, and Byung Moo Lee. Tunable substrate integrated waveguide diplexer with high isolation and wide

- stopband. *IEEE Microwave and Wireless Components Letters*, 29(7):456–458, 2019.
- [75] David E. Senior, Xiaoyu Cheng, and Yong-Kyu Yoon. Electrically tunable evanescent mode half-mode substrate-integrated-waveguide resonators. *IEEE Microwave and Wireless Components Letters*, 22(3):123–125, 2012.
- [76] James R. Chen, Marvin D. Bengel, Akash Anand, Hjalti H. Sigmarsson, and Xiaoguang Liu. An evanescent-mode tunable dual-band filter with independently-controlled center frequencies. *2016 IEEE MTT-S International Microwave Symposium (IMS)*, pages 1–4, 2016.
- [77] Jorge Daniel Martinez, Stefano Sirci, Vicente Enrique Boria, and Miguel Angel Sanchez-Soriano. When compactness meets flexibility: Basic coaxial siw filter topology for device miniaturization, design flexibility, advanced filtering responses, and implementation of tunable filters. *IEEE Microwave Magazine*, 21(6):58–78, 2020.
- [78] Zhihua Wei, Tao Yang, Pei-Ling Chi, Xilin Zhang, and Ruimin Xu. A 10.23–15.7-ghz varactor-tuned microstrip bandpass filter with highly flexible reconfigurability. *IEEE Transactions on Microwave Theory and Techniques*, 69(10):4499–4509, 2021.
- [79] Sang-June Park, Isak Reines, Chirag Patel, and Gabriel M. Rebeiz. High- q rf-mems 4–6-ghz tunable evanescent-mode cavity filter. *IEEE Transactions on Microwave Theory and Techniques*, 58(2):381–389, 2010.
- [80] Fengxi Huang, Siamak Fouladi, and Raafat R. Mansour. High- q tunable dielectric resonator filters using mems technology. *IEEE Transactions on Microwave Theory and Techniques*, 59(12):3401–3409, 2011.

- [81] ZhengAn Yang, Runqi Zhang, and Dimitrios Peroulis. Design and optimization of bidirectional tunable mems all-silicon evanescent-mode cavity filter. *IEEE Transactions on Microwave Theory and Techniques*, 68(6):2398–2408, 2020.
- [82] Thomas R. Jones and Mojgan Daneshmand. Miniaturized folded ridged quarter-mode substrate integrated waveguide rf mems tunable bandpass filter. *IEEE Access*, 8:115837–115847, 2020.
- [83] Gabriel M. Rebeiz, Kamran Entesari, Isak C. Reines, Sang-june Park, Mohammed A. El-tanani, Alex Grichener, and Andrew R. Brown. Tuning in to rf mems. *IEEE Microwave Magazine*, 10(6):55–72, 2009.
- [84] Arghya Sain and Kathleen L. Melde. Impact of ground via placement in grounded coplanar waveguide interconnects. *IEEE Transactions on Components, Packaging and Manufacturing Technology*, 6(1):136–144, 2016.
- [85] *Microwave Filters for Communication Systems: Fundamentals, Design and Applications*. John Wiley Sons, Ltd, 2018.
- [86] Jing Wang, Miao Wu, and Chengqiang Cui. Factors governing filling of blind via and through hole in electroplating. *Circuit World*, 40(3):92–102, 2014.

Appendices

Appendix A

A.1 Fourth-order ELCSIW Filter

A fourth-order Chebyshev embedded loaded coaxial substrata-integrated waveguide filter is designed at 1.1 GHz to demonstrate the capability to scale ELCSIW filters to higher orders. Four ELCSIW resonators are placed in box shape topology, as shown in Figure A.1. The filter has 70 MHz of bandwidth, equivalent to 6.3 % of fractional bandwidth, and an equi-ripple of 20 dB. The input/output feed lines consist of 50 Ω microstrip lines connected to tap striplines through vertical transition vias. These tap striplines are short-circuited to the post of the resonator and allow for magnetic coupling to the cavity. The Chebyshev polynomial coefficients, the calculated inter-resonator coupling coefficient, and external coupling for the second-order ELCSIW filter are listed in Table A.1. Following the design steps in section 2.3, the filter dimensions are realized as shown in Figure A.1. The filter dimensions and the substrates' thicknesses are listed in Table A.2.

Table A.1: The Chebyshev polynomial coefficients, inter-resonator coupling coefficient, and external quality factor for the fourth-order Chebyshev ELCSIW filter.

g_0	g_1	g_2	g_3	g_4
1	0.9332	1.2923	1.5795	0.7636
g_5	k_{12}	k_{23}	k_{34}	Q_{ex}
1.2222	0.0574	0.0441	0.0574	14.8

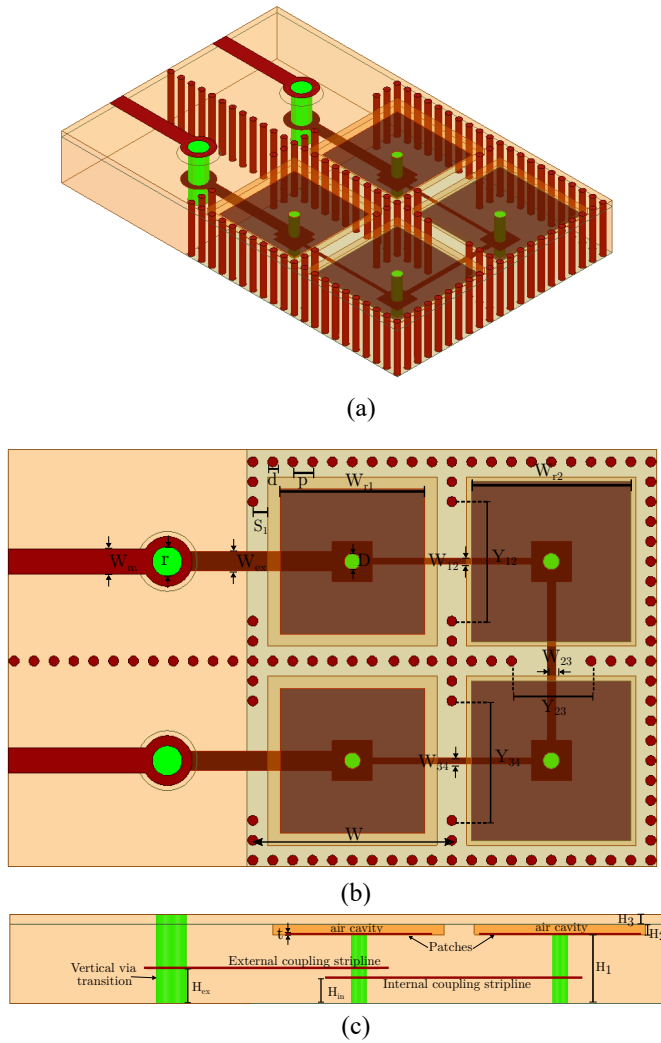


Figure A.1: Design illustration of the fourth-order ELCSIW filter. (a) A 3D structure view, (b) top view, and (c) side view.

Then, the fourth-order filter is simulated using ANSYS HFSS full-wave solver, and the simulated S-parameters are shown in Figure A.2. The insertion loss of the simulated filter is 0.81 dB, including the input/output feed line losses. The fourth-order filter features a sharp roll-off at the 3 dB cutoff frequency, hence enhancing the filter's selectivity.

In this section, The ELCSIW technology has demonstrated the ability to scale to higher orders. This help improves the filter selectivity and unwanted

signals leaking into the passband. Also, the exhibits a low loss and high miniaturization with a fourth-order filter. This demonstrates the advantages of the proposed technology in expanding its boundaries to higher order and different configurations.

Table A.2: Fourth-order ELCSIW filter design parameters. All dimensions are in mm.

Design Parameter	Value
Cavity length (W)	10
Patch width (W_{r1})	7.77
Patch width (W_{r2})	7.93
Post diameter (D)	0.8
Microstrip line width (W_m)	1.2
Microstrip pad (W_p)	2.6
Vertical via transition diameter (D_v)	1.5
Air cavity to via spacing (S_1)	0.9
Outer via diameter (d)	0.5
Outer via spacing (p)	1
Bottom substrate thickness (H_1)	3.378 (133 mils)
Isola prepreg thickness (H_2)	0.0685 (2.7 mils)
Top substrate thickness (H_3)	0.635 (25 mils)
External tap height (H_{ex})	1.6256 (64 mils)
Inter-resonator tap height (H_{in})	1.27 (50 mils)
Copper clad thickness (t)	0.0175
Inter-resonator stripline width (W_{12})	0.36
Inter-resonator stripline width (W_{23})	0.25
Inter-resonator stripline width (W_{34})	0.36
Coupling window (Y_{12})	6
Coupling window (Y_{23})	4
Coupling window (Y_{34})	6
External coupling stripline width (W_{ex})	1.7

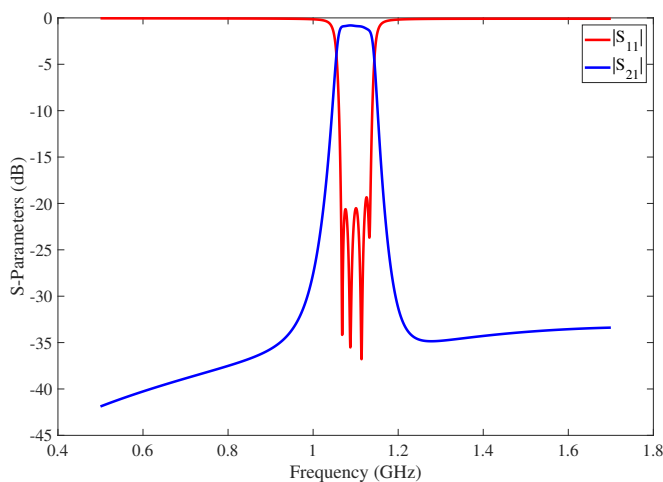


Figure A.2: Simulated S-parameters of the fourth-order ELCSIW filter.

A.2 ELCSIW Resonator and Filter Fabrication Process

The designed resonator and second-order ELCSIW filter shown in Figure 2.15 and 2.21, respectively, are fabricated using a standard PCB process. The dimensions and the substrate thickness of the stack-up layers for the designed resonator and filters are presented in Table. 2.3 and 2.6, respectively. The fabrication steps are designed to meet the capabilities of the ARRC fabrication lab. The summary of the step-by-step of the fabrication process is presented in section 2.3.5. Additional details on the copper plating are presented in this section.

Copper electroplating is a process of coating a copper layer on a surface of a substrate. During fabrication, the stack-up layers required copper electroplating for the posts and cavity vias of the filter and resonator. The stack-up layers are made of dielectric materials that can not be directly copper coated with an electroplating process. Therefore, the copper electroless coating process is required before copper electroplating to deposit a thin layer of copper using a chemical reaction. The electroless process starts with micro-etching the stack-up layers using an acidic bath formulated to activate and condition drilled vias.

Then, the stack-up is treated with a catalytic solution to provide a seed layer on non-metallic objects before depositing copper using an electroless solution bath. Then, the stack-up undergo the electroplating process to electrically deposit $17\ \mu\text{m}$ of copper. The conductivity and the roughness of the copper depend on the condition of the electrolyte bath, organic additives used during the process, and the electroplating method (forward or reverse pulse). The electrolyte bath used in this experiment is an acidic sulfate-based bath. A brightener is used as an additive solution to refine and orientate the grain structure of the copper deposition [86]. This experiment uses the periodic pulse reverse plating method to plate the via surface and uniformly achieve low surface roughness. The periodic pulse reverse plating waveform is shown in Figure A.3. In Figure A.4, cross-sectional photos of plated via using forward pulse and periodic pulse reverse methods are presented. The forward pulse plating shows non-uniform and pinholes in the via surface, whereas the periodic pulse reverse method shows uniform and free-pinhole plating. The parameters of the periodic pulse reverse waveform are listed in Table A.3 where T is the cycle time, t_{on} is the forward pulse on time, t_{off} is the forward pulse off time, $t_{rev.on}$ is the reverse pulse on time, $t_{rev.off}$ is the reverse pulse off time, i_f and i_{rev} are the current densities of the forward and reverse pulse in $\text{A}\cdot\text{ft}^{-2}$ (ASF), respectively.

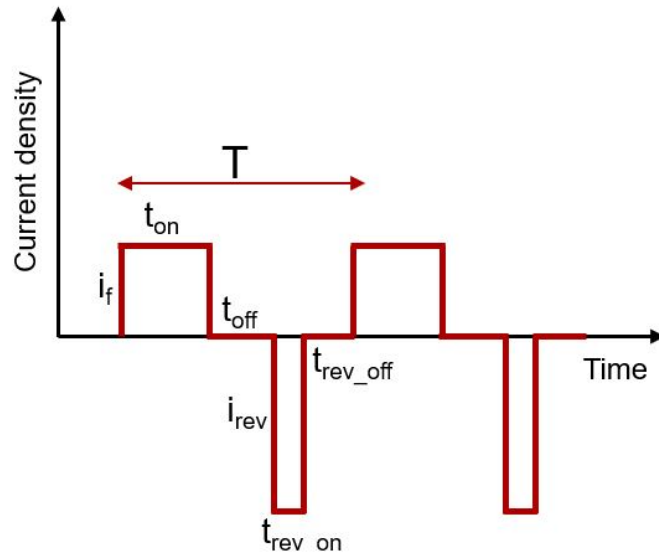


Figure A.3: Schematic diagram illustrating the parameters to describe the forward and reverse pulse plating waveform.

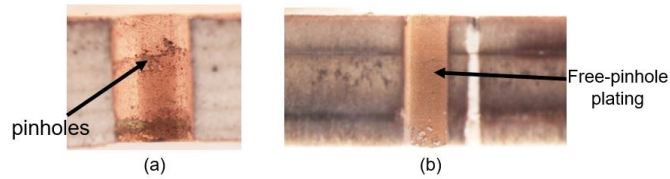


Figure A.4: Cross-section view of plated via using (a) forward pulse, and (b) periodic pulse reverse plating methods.

Table A.3: The periodic pulse reverse program and waveform parameters.

t_{on}	t_{off}	t_{rev_on}	t_{rev_off}	T	i_f	i_{rev}
4 ms	6 ms	1 ms	4 ms	15 ms	4 A.ft ⁻²	0.8 A.ft ⁻²